Global analysis of polarized DIS and SIDIS data with improved small-x helicity evolution

Daniel Adamiak,[1,2] Nicholas Baldonado,[3] Yuri V. Kovchegov,[1] W. Melnitchouk,[2] Daniel Pitonyak,[4] Nobuo Sato,[2] Matthew D. Sievert,[3] Andrey Tarasov,[5,6] and Yossathorn Tawabutr[7,8]

(Jefferson Lab Angular Momentum (JAM) Collaboration)

[1]*Department of Physics, The Ohio State University, Columbus, Ohio 43210, USA*
[2]*Jefferson Lab, Newport News, Virginia 23606, USA*
[3]*Department of Physics, New Mexico State University, Las Cruces, New Mexico 88003, USA*
[4]*Department of Physics, Lebanon Valley College, Annville, Pennsylvania 17003, USA*
[5]*Department of Physics, North Carolina State University, Raleigh, North Carolina 27695, USA*
[6]*Joint BNL-SBU Center for Frontiers in Nuclear Science (CFNS) at Stony Brook University, Stony Brook, New York 11794, USA*
[7]*Department of Physics, University of Jyväskylä, P.O. Box 35, 40014 University of Jyväskylä, Finland*
[8]*Helsinki Institute of Physics, P.O. Box 64, 00014 University of Helsinki, Finland*

(Received 24 August 2023; accepted 19 October 2023; published 11 December 2023)

We analyze the world polarized deep-inelastic scattering (DIS) and semi-inclusive DIS (SIDIS) data at low values of $x < 0.1$, using small-x evolution equations for the flavor singlet and nonsinglet helicity parton distribution functions (hPDFs), which resum all powers of both $\alpha_s \ln^2(1/x)$ and $\alpha_s \ln(1/x) \ln(Q^2/Q_0^2)$, with α_s being the strong coupling constant. The hPDFs for quarks, antiquarks, and gluons are extracted and evolved to lower values of x to make predictions for the future Electron-Ion Collider (EIC). We improve on our earlier work by employing the more realistic large-N_c & N_f limit of the revised small-x helicity evolution, and by incorporating running coupling corrections along with SIDIS data into the fit. We find an anticorrelation between the signs of the gluon and C-even quark hPDFs, as well as the g_1 structure function. While the existing low-x polarized DIS and SIDIS data are insufficient to constrain the initial conditions for the polarized dipole amplitudes in the helicity evolution equations, future EIC data will allow more precise predictions for hPDFs and the g_1 structure function for x values beyond those probed at the EIC. Using the obtained hPDFs, we discuss the contributions to the proton spin from quark and gluon spins at small x.

DOI: 10.1103/PhysRevD.108.114007

I. INTRODUCTION

A. General motivation

The proton spin puzzle has been one of the most intriguing and profound mysteries in our understanding of the proton structure for over three decades (for reviews, see Refs. [1–9]). The main challenge is to determine, both qualitatively and quantitatively, how the proton spin is distributed among the spins and orbital angular momenta (OAM) of its quark and gluon constituents. The question is usually formulated in terms of spin sum rules, such as the Jaffe-Manohar sum rule [10] (see also the Ji sum rule [11]), that decompose the proton spin of $1/2$ (in units of $\hbar$) into the sum of the quark (S_q) and gluon (S_G) spins and the OAM carried by the quarks (L_q) and gluons (L_G):

$$S_q + L_q + S_G + L_G = \frac{1}{2}. \tag{1}$$

Each of the contributions in Eq. (1) can, in turn, be written as the integral of a partonic function over the longitudinal momentum fraction x carried by the parton. For example,

$$S_q(Q^2) = \frac{1}{2}\int_0^1 \mathrm{d}x\, \Delta\Sigma(x, Q^2), \tag{2a}$$

$$S_G(Q^2) = \int_0^1 \mathrm{d}x\, \Delta G(x, Q^2), \tag{2b}$$

with similar expressions for the OAM contributions [12–16], where $\Delta\Sigma(x,Q^2)$ is the flavor singlet combination of the quark helicity parton distribution functions (hPDFs) $\Delta q(x,Q^2)$ (quark flavor q), and $\Delta G(x,Q^2)$ is the gluon hPDF [10]. The goal of current research in the field of proton spin physics is to determine $\Delta\Sigma(x,Q^2)$, $\Delta G(x,Q^2)$, $L_q(x,Q^2)$, and $L_G(x,Q^2)$ across a broad range of x and Q^2 in order to quantify how much of the proton spin is carried by the partons in different kinematic regions.

The standard way to address the proton spin puzzle is by extracting the hPDFs $\Delta q(x,Q^2)$ and $\Delta G(x,Q^2)$ from experimental data using collinear factorization along with the spin-dependent Dokshitzer-Gribov-Lipatov-Altarelli-Parisi (DGLAP) evolution equations [17–19] to relate observables at different Q^2 values. There have been a number of very successful extractions of hPDFs over the years within this approach [20–34]. Nevertheless, the DGLAP-based methodology has a drawback: since the DGLAP equations evolve PDFs in Q^2, they cannot truly predict the x dependence of PDFs. The x dependence is greatly affected by the functional form of the PDF parametrization at the initial momentum scale Q_0^2, which gives the initial conditions for the DGLAP evolution. The parameters are then determined by optimizing agreement between the theoretical calculations to the experimental measurements. In this way, the experimental data, in the x range where it is available, make up for the inability of DGLAP evolution to predict the x dependence of PDFs. Conversely, in the x region which has not yet been probed experimentally, DGLAP-based predictions typically acquire a broad uncertainty band due to extrapolation errors. This is particularly true in the small-x region. Since no experiment, present or future, can perform measurements down to $x=0$, further theoretical input is needed to constrain the hPDFs at low x. The benefit of small-x helicity evolution is that it makes a genuine prediction for the hPDFs at small x given some initial conditions at a higher x_0. Due to the integrals in Eq. (2), precise control over the behavior of hPDFs at small x is mandatory to resolving the proton spin puzzle.

B. Proton spin at small x

The first resummation of hPDFs at small x was performed in the pioneering work by Bartels, Ermolaev, and Ryskin (BER) [35,36], who employed the infrared evolution equations (IREE) formalism from Refs. [37–41]. The BER IREE resummed double logarithms of x—i.e., powers of the parameter $\alpha_s \ln^2(1/x)$ (with α_s being the strong coupling constant)—which is referred to as the double-logarithmic approximation (DLA). The leading small-x asymptotics for the flavor singlet combination of quark hPDFs and the gluon hPDF can be written as

$$\Delta\Sigma(x,Q^2)\sim\Delta G(x,Q^2)\sim\left(\frac{1}{x}\right)^{\alpha_h}, \tag{3}$$

with α_h being the helicity intercept. BER found $\alpha_h=3.66\sqrt{\frac{\alpha_s N_c}{2\pi}}$ in the pure gluon case and $\alpha_h=3.45\sqrt{\frac{\alpha_s N_c}{2\pi}}$ for $N_f=4$ (the numbers 3.66 and 3.45 were calculated numerically, the latter for $N_c=3$, with N_c/N_f being the number of quark colors/flavors). These intercepts are numerically large, with $\alpha_h>1$ for realistic coupling $\alpha_s=0.2$–0.3, making the integrals (2) divergent as $x\to 0$. One may hope that the higher-order corrections in α_s, when calculated, would lower the intercept α_h below 1, making the integrals (2) convergent. In addition, at very small x, parton saturation corrections (see Refs. [42–49] for reviews) are likely to significantly modify the asymptotics (3) by slowing down (or completely stopping) the growth of hPDFs with decreasing x (see, e.g., [50] for the impact of saturation effects on the unpolarized flavor nonsinglet evolution). Phenomenological applications of the BER IREE approach were developed in Refs. [51–56]. Recently, the BER approach has been applied to the OAM distributions as well [57].

Over the past decade, a new approach to helicity evolution at small x has been developed [58–71] employing the shock wave/s-channel evolution formalism originally constructed in Refs. [72–84] for unpolarized eikonal scattering. The main idea behind the works [58–71] is that the subeikonal, sub-subeikonal, etc., quantities obey small-x evolution equations similar to the eikonal ones [75–84], resulting from an s-channel gluon (or quark) cascade. (See Refs. [63,64,85–98] for the formalism of subeikonal and sub-subeikonal evolution in high-energy scattering.) The subeikonal quantities are suppressed by one power of x compared to the eikonal ones, while sub-subeikonal quantities are suppressed by two powers of x, etc.

The equations developed in Refs. [58,60,63,64,66,71] were also derived in the DLA. Similarly to the unpolarized evolution equations [75–84], the helicity evolution equations [58,60,63,64,71] only take on a closed form in the large-N_c [99] and large-N_c & N_f [100] limits. In that case, they become the evolution equations for the so-called "polarized dipole amplitudes," which are dipole scattering amplitudes with an insertion of one gluon or two quark operators at the subeikonal level into the light-cone Wilson lines [63,64,71,92]. The earlier version of this evolution, constructed in Refs. [58,60,63] (which we will refer to as KPS), led to an intercept of $\alpha_h=\frac{4}{\sqrt{3}}\sqrt{\frac{\alpha_s N_c}{2\pi}}\approx 2.31\sqrt{\frac{\alpha_s N_c}{2\pi}}$ in the large-N_c limit [61,62], significantly smaller than the intercept of $\alpha_h=3.66\sqrt{\frac{\alpha_s N_c}{2\pi}}$ found by BER in the same limit. The KPS evolution has recently been augmented [71] by inclusion of the operators which couple what can be interpreted as the OAM of the gluon probe (in the $A^-=0$ light-cone gauge of the projectile) to the spin of the proton.[1]

[1]We thank Florian Cougoulic, Alex Kovner, and Feng Yuan for suggesting this interpretation of those operators.

The revised evolution equations, which we will refer to as the KPS-CTT equations [58,64,71], have been solved at large N_c both numerically [71] and analytically [101]. While the former reference found the numerical value of the intercept to be $\alpha_h = 3.66\sqrt{\frac{\alpha_s N_c}{2\pi}}$, appearing to agree with BER, the analytic solution [101] found that the BER and KPS-CTT intercepts at large N_c disagree in the third decimal point. Very recently, a numerical solution of the large-N_c & N_f version of the KPS-CTT evolution [102] established a disagreement with BER (in the same limit) at the 2%–3% level, with the discrepancy increasing with N_f. While the observed differences between the two sets of results appear to demand further theoretical investigation, they are sufficiently small to allow one to proceed with rigorous phenomenological applications of the KPS-CTT evolution equations [58,60,63,64,71].

The first phenomenological application of the polarized dipole amplitude formalism—more precisely, its KPS version—was performed by a subset of the present authors in Ref. [103]. In that work, a successful "proof of principle" fit of the world polarized DIS data for $x < 0.1$ and $Q^2 > m_c^2$ (with m_c being the charm quark mass) based solely on small-x helicity evolution was performed. Since the analysis of Ref. [103] was limited to DIS data, only the g_1 structure functions of the proton and neutron were extracted instead of the individual flavor hPDFs. The impact of DIS data from the EIC on our ability to predict the g_1 structure function at small x was also estimated. In addition, in order to demonstrate that it is possible to extract the combinations $\Delta q^+(x,Q^2) \equiv \Delta q(x,Q^2) + \Delta\overline{q}(x,Q^2)$ for $q = u,\ d,\ s$ using small-x helicity evolution, parity-violating DIS EIC pseudodata were utilized. We refer to $\Delta q^+(x,Q^2)$ as the C-even hPDFs, whereas the flavor nonsinglet C-odd hPDFs are similarly defined as $\Delta q^-(x,Q^2) \equiv \Delta q(x,Q^2) - \Delta\overline{q}(x,Q^2)$.

C. Subject of this work

In the present paper, we perform, for the first time, a phenomenological analysis based on the KPS-CTT version of small-x helicity evolution with several other significant new features beyond the work of Ref. [103]. Instead of the large-N_c limit of evolution employed in Ref. [103], we base our analysis on the large-N_c & N_f limit. In addition to the polarized DIS data, we also include in our analysis polarized SIDIS data. Since the SIDIS data are sensitive to the individual quark and antiquark helicity PDFs, $\Delta q(x,Q^2)$ and $\Delta\overline{q}(x,Q^2)$, it is not sufficient to just use the flavor singlet helicity evolution from Ref. [71], which only yields the $\Delta q^+(x,Q^2)$ combination [in addition to the gluon hPDF $\Delta G(x,Q^2)$]. One also needs the flavor nonsinglet quark hPDFs $\Delta q^-(x,Q^2)$. Those are constructed using the large-N_c, small-x helicity evolution equation for the flavor nonsinglet case from Ref. [60]. Finally, to make the calculation more realistic and avoid the integrals (2) diverging at $x \to 0$, we include running coupling corrections into the kernel of the evolution equations (both flavor singlet and nonsinglet). We make the coupling run with the daughter dipole size, which ends up effectively reducing the intercept α_h for Δq^+ and ΔG below 1. (The intercept of the flavor nonsinglet hPDFs is smaller than 1 even at fixed coupling in the realistic $\alpha_s = 0.2$–0.3 range; still, for consistency, we apply running coupling corrections to the flavor nonsinglet helicity evolution as well.) The analysis of SIDIS data also requires input for fragmentation functions, which are not specific to the small-x evolution at hand; therefore, we employ the existing JAM fragmentation functions for pions, kaons, and unidentified hadrons from Ref. [34].

The paper is structured as follows: We begin in Sec. II by outlining the polarized dipole amplitude formalism developed in Refs. [58,60,63,64,71] and explicitly writing out the flavor-singlet KPS-CTT large-N_c & N_f, DLA small-x helicity evolution equations with running coupling corrections, along with the flavor nonsinglet helicity evolution equation derived in Ref. [60]. We also present the details of our numerical methodology in solving these evolution equations. We describe the calculation of observables (double-longitudinal spin asymmetries) in DIS and SIDIS, particularly detailing the calculation of the polarized SIDIS cross section at small x. We explain our analysis of the world polarized DIS and SIDIS low-x data and describe the implementation of the KPS-CTT evolution within the JAM Bayesian Monte Carlo framework. The results of our analysis are presented in Sec. III, which includes plots of data versus theory, the hPDFs, and the g_1 structure function, as well as an estimate of how much of the proton spin is carried by the net spin of partons at small x. We also conduct an EIC impact study on the aforementioned quantities. Conclusions and an outlook are given in Sec. IV.

II. METHODOLOGY

A. Flavor singlet evolution at small x

The small-x helicity formalism in the light-cone operator treatment (LCOT) framework along with the large-N_c & N_f, small-x evolution equations for helicity were revised in Ref. [71]. In the new formalism, the (DIS) g_1 structure function is given by

$$g_1(x,Q^2) = \frac{1}{2}\sum_q e_q^2 \Delta q^+(x,Q^2), \tag{4}$$

where e_q is the quark electric charge as a fraction of the magnitude of the electron's charge. The C-even quark hPDFs in the DLA take the form [64,71]

$$\begin{aligned}\Delta q^+(x,Q^2) &\equiv \Delta q(x,Q^2) + \Delta\overline{q}(x,Q^2)\\ &= -\frac{N_c}{2\pi^3}\int_{\Lambda^2/s}^1 \frac{dz}{z}\int_{1/zs}^{\min[1/z\mathcal{Q}^2,1/\Lambda^2]} \frac{dx_{10}^2}{x_{10}^2}\\ &\quad\times [Q_q(x_{10}^2,zs) + 2G_2(x_{10}^2,zs)].\end{aligned} \tag{5}$$

The gluon hPDF in the DLA is [63]

$$\Delta G(x,Q^2)=\frac{2N_c}{\alpha_s\pi^2}G_2\left(x_{10}^2=\frac{1}{Q^2},zs=\frac{Q^2}{x}\right). \quad (6)$$

Note that the quark and gluon hPDFs Δq^+ and ΔG are expressed in terms of the impact-parameter-integrated polarized dipole amplitudes Q_q and G_2, whose operator definitions can be found in Refs. [58,64,71] and Ref. [63], respectively. The dipole amplitudes depend on the transverse size of the dipole $x_{10}=|\mathbf{x}_1-\mathbf{x}_0|$, where the "polarized" (subeikonally interacting) line is located at $\mathbf{x}_1$, and the unpolarized (standard) Wilson line is at $\mathbf{x}_0$ in the transverse plane. The amplitudes also depend on the center-of-mass energy squared s of the projectile-proton scattering. The dimensionless longitudinal momentum fraction z can be thought of as the momentum fraction of the softest of the two lines in the dipole. (However, this definition is somewhat imprecise, and it is more accurate to think of zs as the effective energy of the dipole-proton scattering [58,60,70].) The momentum scale Λ denotes our infrared (IR) cutoff and is the scale characterizing the proton. No dipole can be larger than $1/\Lambda$—that is, the transverse size $x_{10}<1/\Lambda$.

At small x, Eq. (4) was derived in Refs. [58,60,61]. However, the contribution of G_2 to Δq^+ in Eq. (5) was recognized only recently [71]. Given that G_2 is closely related to the gluon hPDF ΔG, as follows from Eq. (6), Eqs. (4) and (5) show that in our LCOT approach, the contribution of ΔG to g_1 comes in through Δq^+ [71,102] (see more on this below). We have also expanded the definition of the amplitude Q_q to include dependence on the quark flavor $q=u,d,s$, such that we have three different amplitudes Q_u, Q_d, and Q_s for the light flavors, which is necessary, since the quark spinor field operators are flavor dependent. The operator definition for the three flavors is the same, but the flavor dependence can enter through the initial condition of the dipole amplitude evolution.

While Eq. (4) appears to correspond to the leading-order (LO) expression in the collinear factorization approach to polarized DIS [see, e.g., Eq. (4.5) in Ref. [104]], in the LCOT framework, it contains more information than that. In collinear factorization at the next-to-leading order (NLO) and beyond, the expression for the g_1 structure function also involves the contribution of ΔG. More precisely, one can write [18,19,105–114]

$$g_1(x,Q^2)=\frac{1}{2}\sum_q e_q^2\Bigg\{\Delta q^+(x,Q^2)+\int_x^1\frac{dz}{z}\left[\Delta c_q(z)\Delta q^+\left(\frac{x}{z},Q^2\right)+\Delta c_G(z)\Delta G\left(\frac{x}{z},Q^2\right)\right]\Bigg\}, \quad (7)$$

with the coefficient functions $\Delta c_q(z)$ and $\Delta c_G(z)$ calculated order by order in perturbation theory. In the $\overline{\text{MS}}$ scheme, the small-x, large-N_c & N_f coefficient functions are [105] (see also [114] for the three-loop contribution, which we do not show explicitly here)

$$\Delta c_q(z)=\frac{\alpha_s N_c}{4\pi}\ln\frac{1}{z}+\frac{5}{12}\left(\frac{\alpha_s N_c}{4\pi}\right)^2\left[1-4\frac{N_f}{N_c}\right]\ln^3\frac{1}{z}+\mathcal{O}(\alpha_s^3), \quad (8a)$$

$$\Delta c_G(z)=-\frac{\alpha_s}{2\pi}\ln\frac{1}{z}-\frac{11}{2}\left(\frac{\alpha_s}{4\pi}\right)^2 N_c\ln^3\frac{1}{z}+\mathcal{O}(\alpha_s^3). \quad (8b)$$

Note that after the z integration in Eq. (7), the contribution from the order-α_s terms in Eq. (8) becomes of the order $\alpha_s\ln^2(1/x)$, while the contribution from the order-α_s^2 terms in Eq. (8) becomes of the order $[\alpha_s\ln^2(1/x)]^2$, etc. Consequently, in the collinear factorization power counting, the contributions from $\Delta c_q(z)$ and $\Delta c_G(z)$ in Eq. (7) are NLO and beyond, allowing one to truncate the expansion at a given order in α_s determined by the accuracy of the calculation. In our DLA small-x power counting, the leading small-x parts of $\Delta c_q(z)$ and $\Delta c_G(z)$ are already included to all orders in the powers of $\alpha_s\ln^2(1/x)$. This is precisely what Eq. (4) accomplishes [102]. While it appears to be just the LO part of Eq. (7), the fact that Δq^+ in it is evolved with the DLA small-x helicity evolution [58,60,63,64,71], resumming powers of both $\alpha_s\ln^2(1/x)$ and $\alpha_s\ln(1/x)\ln(Q^2/Q_0^2)$, implies that Eq. (4) contains both the DLA DGLAP evolution of Δq^+, which mixes it with ΔG [by resumming the powers of $\alpha_s\ln(1/x)\ln(Q^2/Q_0^2)$], and the leading small-x parts of the coefficient functions $\Delta c_q(z)$ and $\Delta c_G(z)$, resummed to all orders in $\alpha_s\ln^2(1/x)$, bringing the ΔG and additional Δq^+ contributions into g_1, as expected from Eq. (7) (see [102] for a more detailed discussion). The fact that all these contributions are contained in Eq. (4), which looks much simpler than Eq. (7), appears to suggest that we are working in the "polarized DIS scheme" [102] for our hPDFs (cf. [115] for the standard DIS scheme), where ΔG does not contribute to g_1 directly, unlike the more widely used $\overline{\text{MS}}$ scheme from Eq. (7). Other small-x calculations, such as the NLO BFKL evolution [116,117] (in the small-x power counting), result in the spin-independent GG anomalous dimension in the DIS scheme [108]. This appears to be similar to our calculation giving a polarized DIS scheme result, with the difference between the anomalous dimensions in different schemes being proportional to N_f [102,108].

The polarized dipole amplitudes Q_q and G_2, which enter Eqs. (4)–(6), are found by solving the small-x evolution equations. The DLA large-N_c & N_f revised evolution equations at fixed coupling are given by Eq. (155) in Ref. [71] (see also Refs. [58,64]). Its existing numerical solution [102] (with fixed coupling) leads to a large

intercept α_h for the flavor singlet hPDFs and for Δq^+ [see Eq. (3) with the intercept values in the text following that equation], making the integrals in Eq. (2) divergent as $x \to 0$. As we discussed above, this divergence may be regulated by higher-order corrections and/or by the onset of saturation, which is likely to slow down the growth of hPDFs as $x \to 0$. As the unpolarized small-x evolution [72–84] is single-logarithmic, resumming powers of $\alpha_s \ln(1/x)$, a consistent inclusion of saturation effects is beyond the double-logarithmic approximation employed here. While, strictly speaking, phenomenology based on small-x evolution in the DLA should work with the high intercepts found in Ref. [102], it appears to be unphysical to perform an analysis of experimental data with a formalism that would yield an infinite amount of spin at small x. While we cannot include the single-logarithmic [resumming powers of $\alpha_s \ln(1/x)$] corrections to the revised DLA evolution equations (155) from Ref. [71], since they have not been fully calculated yet (see Ref. [70] for the single-logarithmic corrections to the earlier KPS evolution), we can include running-coupling corrections in the DLA evolution. A similar approximation was employed in the BER framework [53,55] and for the spin-independent eikonal small-x evolution [118,119], resulting in successful phenomenology.

In the DLA equations (155) from Ref. [71], the scale of the coupling could be given by either the "parent" (x_{10}) or the "daughter" (x_{21} or x_{32}) dipole. The running coupling corrections to the (unrevised) KPS evolution, calculated in Ref. [70] (along with other single-logarithmic corrections), indicate that at DLA the coupling runs with the daughter dipole size. For the neighbor dipole amplitudes $\overline{\Gamma}$, $\widetilde{\Gamma}$, and Γ_2, introduced in Refs. [58,60,63,64,66,71] and also entering helicity evolution equations, the coupling runs with the dipole size x_{32}, which determines the next emission's lifetime and is integrated over in the kernel [70]. Therefore, we proceed by running the coupling with the daughter dipole size (or, more precisely, with the dipole size that we integrate over in the kernel) in all the terms of the KPS-CTT evolution. (See Refs. [120–124] for calculations and analyses of the running coupling corrections in the unpolarized small-x evolution case.) The resulting running-coupling version of the large-N_c & N_f helicity evolution equations (155) from [71] reads

$$
\begin{aligned}
Q_q(x_{10}^2, zs) &= Q_q^{(0)}(x_{10}^2, zs) + \frac{N_c}{2\pi}\int_{1/x_{10}^2 s}^{z}\frac{dz'}{z'}\int_{1/z's}^{x_{10}^2}\frac{dx_{21}^2}{x_{21}^2}\alpha_s\left(\frac{1}{x_{21}^2}\right)\left[2\widetilde{G}(x_{21}^2, z's) + 2\widetilde{\Gamma}(x_{10}^2, x_{21}^2, z's)\right.\\
&\left. + Q_q(x_{21}^2, z's) - \overline{\Gamma}_q(x_{10}^2, x_{21}^2, z's) + 2\Gamma_2(x_{10}^2, x_{21}^2, z's) + 2G_2(x_{21}^2, z's)\right]\\
&+ \frac{N_c}{4\pi}\int_{\Lambda^2/s}^{z}\frac{dz'}{z'}\int_{1/z's}^{\min[x_{10}^2 z/z', 1/\Lambda^2]}\frac{dx_{21}^2}{x_{21}^2}\alpha_s\left(\frac{1}{x_{21}^2}\right)\left[Q_q(x_{21}^2, z's) + 2G_2(x_{21}^2, z's)\right], \qquad (9a)\\
\overline{\Gamma}_q(x_{10}^2, x_{21}^2, z's) &= Q_q^{(0)}(x_{10}^2, z's) + \frac{N_c}{2\pi}\int_{1/x_{10}^2 s}^{z'}\frac{dz''}{z''}\int_{1/z''s}^{\min[x_{10}^2, x_{21}^2 z'/z'']}\frac{dx_{32}^2}{x_{32}^2}\alpha_s\left(\frac{1}{x_{32}^2}\right)\left[2\widetilde{G}(x_{32}^2, z''s)\right.\\
&\left. + 2\widetilde{\Gamma}(x_{10}^2, x_{32}^2, z''s) + Q_q(x_{32}^2, z''s) - \overline{\Gamma}_q(x_{10}^2, x_{32}^2, z''s) + 2\Gamma_2(x_{10}^2, x_{32}^2, z''s) + 2G_2(x_{32}^2, z''s)\right]\\
&+ \frac{N_c}{4\pi}\int_{\Lambda^2/s}^{z'}\frac{dz''}{z''}\int_{1/z''s}^{\min[x_{21}^2 z'/z'', 1/\Lambda^2]}\frac{dx_{32}^2}{x_{32}^2}\alpha_s\left(\frac{1}{x_{32}^2}\right)\left[Q_q(x_{32}^2, z''s) + 2G_2(x_{32}^2, z''s)\right], \qquad (9b)\\
\widetilde{G}(x_{10}^2, zs) &= \widetilde{G}^{(0)}(x_{10}^2, zs) + \frac{N_c}{2\pi}\int_{1/x_{10}^2 s}^{z}\frac{dz'}{z'}\int_{1/z's}^{x_{10}^2}\frac{dx_{21}^2}{x_{21}^2}\alpha_s\left(\frac{1}{x_{21}^2}\right)\left[3\widetilde{G}(x_{21}^2, z's) + \widetilde{\Gamma}(x_{10}^2, x_{21}^2, z's)\right.\\
&\left. + 2G_2(x_{21}^2, z's) + \left(2 - \frac{N_f}{2N_c}\right)\Gamma_2(x_{10}^2, x_{21}^2, z's) - \frac{1}{4N_c}\sum_q \overline{\Gamma}_q(x_{10}^2, x_{21}^2, z's)\right]\\
&- \frac{1}{8\pi}\int_{\Lambda^2/s}^{z}\frac{dz'}{z'}\int_{\max[x_{10}^2, 1/z's]}^{\min[x_{10}^2 z/z', 1/\Lambda^2]}\frac{dx_{21}^2}{x_{21}^2}\alpha_s\left(\frac{1}{x_{21}^2}\right)\left[\sum_q Q_q(x_{21}^2, z's) + 2N_f G_2(x_{21}^2, z's)\right], \qquad (9c)\\
\widetilde{\Gamma}(x_{10}^2, x_{21}^2, z's) &= \widetilde{G}^{(0)}(x_{10}^2, z's) + \frac{N_c}{2\pi}\int_{1/x_{10}^2 s}^{z'}\frac{dz''}{z''}\int_{1/z''s}^{\min[x_{10}^2, x_{21}^2 z'/z'']}\frac{dx_{32}^2}{x_{32}^2}\alpha_s\left(\frac{1}{x_{32}^2}\right)\left[3\widetilde{G}(x_{32}^2, z''s)\right.\\
&\left. + \widetilde{\Gamma}(x_{10}^2, x_{32}^2, z''s) + 2G_2(x_{32}^2, z''s) + \left(2 - \frac{N_f}{2N_c}\right)\Gamma_2(x_{10}^2, x_{32}^2, z''s) - \frac{1}{4N_c}\sum_q \overline{\Gamma}_q(x_{10}^2, x_{32}^2, z''s)\right]\\
&- \frac{1}{8\pi}\int_{\Lambda^2/s}^{z'x_{21}^2/x_{10}^2}\frac{dz''}{z''}\int_{\max[x_{10}^2, 1/z''s]}^{\min[x_{21}^2 z'/z'', 1/\Lambda^2]}\frac{dx_{32}^2}{x_{32}^2}\alpha_s\left(\frac{1}{x_{32}^2}\right)\left[\sum_q Q_q(x_{32}^2, z''s) + 2N_f G_2(x_{32}^2, z''s)\right], \qquad (9d)
\end{aligned}
$$

$$G_2(x_{10}^2, zs) = G_2^{(0)}(x_{10}^2, zs) + \frac{N_c}{\pi}\int_{\Lambda^2/s}^{z}\frac{\mathrm{d}z'}{z'}\int_{\max\left[x_{10}^2,\frac{1}{z's}\right]}^{\min\left[\frac{z}{z'}x_{10}^2,\frac{1}{\Lambda^2}\right]}\frac{\mathrm{d}x_{21}^2}{x_{21}^2}\alpha_s\left(\frac{1}{x_{21}^2}\right)[\widetilde{G}(x_{21}^2, z's) + 2G_2(x_{21}^2, z's)], \tag{9e}$$

$$\Gamma_2(x_{10}^2, x_{21}^2, z's) = G_2^{(0)}(x_{10}^2, z's) + \frac{N_c}{\pi}\int_{\Lambda^2/s}^{z'\frac{x_{21}^2}{x_{10}^2}}\frac{\mathrm{d}z''}{z''}\int_{\max\left[x_{10}^2,\frac{1}{z''s}\right]}^{\min\left[\frac{z'}{z''}x_{21}^2,\frac{1}{\Lambda^2}\right]}\frac{\mathrm{d}x_{32}^2}{x_{32}^2}\alpha_s\left(\frac{1}{x_{32}^2}\right)[\widetilde{G}(x_{32}^2, z''s) + 2G_2(x_{32}^2, z''s)]. \tag{9f}$$

The running coupling in Eq. (9) is given by the standard one-loop expression,

$$\alpha_s(Q^2) = \frac{12\pi}{11N_c - 2N_f}\frac{1}{\ln(Q^2/\Lambda_{\mathrm{QCD}}^2)}, \tag{10}$$

with Λ_{QCD} being the QCD confinement scale. We have also modified Eq. (9) compared to Eq. (155) in Ref. [71] in two additional ways: first, we are now treating the momentum scale Λ as the infrared cutoff (assuming that $\Lambda > \Lambda_{\mathrm{QCD}}$); second, since the amplitude Q_q is now flavor dependent, we have replaced the N_f factors from Ref. [71] with flavor sums ($\sum_q$). Equation (9) also includes the dipole amplitude $\widetilde{G}$, which is defined in Ref. [71]: as one can see from Eqs. (4)–(6), the g_1 structure function and hPDFs do not depend on this dipole amplitude: this will affect our analysis below. Following Refs. [58,60,63,64,66,71], we have introduced the impact-parameter integrated "neighbor dipole amplitudes" $\overline{\Gamma}_q(x_{10}^2, x_{32}^2, zs)$, $\widetilde{\Gamma}(x_{10}^2, x_{32}^2, zs)$, and $\Gamma_2(x_{10}^2, x_{32}^2, zs)$ for the amplitudes Q_q, $\widetilde{G}$, and G_2, respectively, with physical dipole transverse size x_{10} and lifetime $\sim x_{32}^2 z$. This lifetime for the neighbor dipole amplitudes depends on the transverse size of another (adjacent) dipole, giving rise to the "neighbor" amplitude name.

The inhomogeneous terms (initial conditions) in Eq. (9) can be calculated at the Born level for a longitudinally polarized massless quark target instead of the proton. This gives [58,60,63,71]

$$\widetilde{G}^{(0)}(x_{10}^2, zs) = Q_q^{(0)}(x_{10}^2, zs) = \frac{\alpha_s^2 C_F}{2N_c}\pi\left[C_F \ln\frac{zs}{\Lambda^2} - 2\ln(zsx_{10}^2)\right], \tag{11a}$$

$$G_2^{(0)}(x_{10}^2, zs) = \frac{\alpha_s^2 C_F}{N_c}\pi\ln\frac{1}{x_{10}\Lambda}, \tag{11b}$$

where $C_F = (N_c^2 - 1)/(2N_c)$ is the Casimir operator in the fundamental representation of SU(N_c). These expressions will motivate our choice of the initial conditions for our phenomenological analysis. (While, strictly speaking, we should have included running coupling corrections in the expressions (11) as well, the fixed coupling form has a sufficient variety of dependence on the relevant variables zs and x_{10} to motivate a fairly broad class of initial conditions we will implement below).

B. Flavor nonsinglet evolution at small x

As one can see from Eq. (4) in the previous subsection, measurements of the g_1 structure function in DIS off a nucleon are only sensitive to a specific linear combination of $\Delta q^+(x, Q^2)$. Such DIS measurements were the topic of our previous study [103]. However, the polarized SIDIS process, as we will see below, provides information on the individual flavor hPDFs $\Delta q(x, Q^2)$—or, equivalently, on both $\Delta q^+(x, Q^2)$ and $\Delta q^-(x, Q^2) \equiv \Delta q(x, Q^2) - \Delta\overline{q}(x, Q^2)$. The above evolution equations (9) only allow us to calculate $\Delta q^+(x, Q^2)$. To perform the polarized SIDIS data analysis, we need to supplement them with the small-x helicity evolution in the flavor nonsinglet channel.

A closed evolution equation at small x yielding $\Delta q^-(x, Q^2)$ in the LCOT framework can be obtained in the large-N_c limit, which is equivalent to the large-N_c & N_f limit for the flavor nonsinglet helicity evolution in DLA. (In the DLA, the flavor nonsinglet evolution is N_f-independent, since virtual quark bubbles do not contribute. Thus, the large-N_c and large-N_c & N_f limits are identical for flavor nonsinglet evolution.) Employing Eq. (54b) of [60], we write in the DLA

$$\Delta q^-(x, Q^2) \equiv \Delta q(x, Q^2) - \Delta\overline{q}(x, Q^2) = \frac{N_c}{2\pi^3}\int_{\Lambda^2/s}^{1}\frac{\mathrm{d}z}{z}\int_{1/zs}^{\min[1/zQ^2, 1/\Lambda^2]}\frac{\mathrm{d}x_{10}^2}{x_{10}^2} \times G_q^{\mathrm{NS}}(x_{10}^2, zs). \tag{12}$$

We see that $\Delta q^-(x, Q^2)$ only depends on one (impact-parameter integrated) polarized dipole amplitude, $G_q^{\mathrm{NS}}(x_{10}^2, zs)$, for each flavor $q = u, d, s$. The definition of this dipole amplitude can be found in Eq. (55) of Ref. [60]. Just as in the flavor singlet case, the nonsinglet dipole amplitude can be determined by solving the small-x evolution equation, which reads [60]

$$G_q^{\mathrm{NS}}(x_{10}^2, z) = G_q^{\mathrm{NS}(0)}(x_{10}^2, z) + \frac{N_c}{4\pi}\int_{\Lambda^2/s}^{z}\frac{\mathrm{d}z'}{z'} \times \int_{1/z's}^{\min[x_{10}^2 z/z', 1/\Lambda^2]}\frac{\mathrm{d}x_{21}^2}{x_{21}^2}\alpha_s\left(\frac{1}{x_{21}^2}\right) \times G_q^{\mathrm{NS}}(x_{21}^2, z'). \tag{13}$$

To be consistent with the flavor-singlet evolution, we have also inserted a running coupling into Eq. (13), modifying it slightly compared to the fixed-coupling flavor nonsinglet evolution equation derived in Ref. [60]. The inhomogeneous term in Eq. (13) can also be calculated at Born level for a quark target [60]:

$$G_q^{\mathrm{NS}(0)}(x_{10}^2, zs) = \frac{\alpha_s^2 C_F^2}{N_c}\pi \ln\frac{zs}{\Lambda^2}. \tag{14}$$

This expression will again motivate our choice of the flavor nonsinglet initial conditions in phenomenology.

C. Numerical implementation of the flavor singlet and nonsinglet evolution

Similarly to our previous works [61,67,71,102], small-x helicity evolution equations simplify if one performs the following change of variables:

$$\eta^{(n)} = \sqrt{\frac{N_c}{2\pi}}\ln\frac{z^{(n)}s}{\Lambda^2}, \qquad s_{ij} = \sqrt{\frac{N_c}{2\pi}}\ln\frac{1}{x_{ij}^2\Lambda^2}. \tag{15}$$

Here, $z^{(n)} = z, z', z'', \ldots,$ while $\eta^{(n)} = \eta, \eta', \eta'', \ldots$. Note that this form, in contrast to the earlier works, removes the factor $\sqrt{\alpha_s}$ from the definition of the variables η and s_{ij}, so that the one-loop running of the coupling can be implemented via [cf. Eq. (10)]

$$\alpha_s(s_{21}) = \sqrt{\frac{N_c}{2\pi}}\frac{12\pi}{(11N_c - 2N_f)}\frac{1}{(s_{21}+s_0)}, \tag{16a}$$

$$s_0 = \sqrt{\frac{N_c}{2\pi}}\ln\frac{\Lambda^2}{\Lambda_{\mathrm{QCD}}^2}. \tag{16b}$$

Since we assume that $\Lambda > \Lambda_{\mathrm{QCD}}$, we have $s_0 > 0$. As all our dipole sizes are smaller than $1/\Lambda$, we see that $s_{21} > 0$, thus avoiding the Landau pole at $s_{21} = -s_0 < 0$ in the coupling. (In general, having an IR cutoff for the dipole sizes, $x_{ij} < 1/\Lambda$, implies that all $s_{ij} > 0$.)

Before discretizing our evolution equations, we need to impose the starting value of x for our evolution (cf. Ref. [103]). For $z = 1$ and $x_{10} = 1/Q$, we have the "rapidity" variable $y \equiv \eta - s_{10} = \sqrt{\frac{N_c}{2\pi}}\ln\frac{1}{x}$. Hence, if our evolution starts at some value of x labeled by x_0, then the $x < x_0$ condition implies that $\eta - s_{10} > \sqrt{\frac{N_c}{2\pi}}\ln\frac{1}{x_0} \equiv y_0$. Regarding the value of x_0, it was observed in Ref. [103], using the older (KPS) version of our helicity evolution, that good χ^2 fits of the polarized DIS data can be obtained with $x_0 = 0.1$ (and even for slightly higher values of x_0). This is in contrast to the $x_0 = 0.01$ starting point of the evolution [75–84] for phenomenological analyses of the unpolarized observables (see, e.g., Refs. [118,119]). As discussed in Sec. III A below, it was speculated in Ref. [103] that such a discrepancy could be attributed to the helicity evolution resumming the double-logarithmic parameter $\alpha_s \ln^2(1/x)$ while the unpolarized evolution [77–84,125,126] resums single logarithms $\alpha_s \ln(1/x)$. This way, the resummation parameter for helicity evolution is larger at small x, making the helicity evolution start at larger x values. We thus put $x_0 = 0.1$ in all our analyses below.[2]

The full process of discretizing our flavor singlet and nonsinglet evolution equations with running coupling is detailed in Appendix A. In the end, the discretized version of Eq. (9) written in terms of the variables in (15) reads

$$\begin{aligned} Q_q[i,j] &= Q_q[i,j-1] + Q_q^{(0)}[i,j] - Q_q^{(0)}[i,j-1] \\ &\quad + \Delta^2 \sum_{i'=i}^{j-2-y_0} \alpha_s[i']\left[\frac{3}{2}Q_q[i',j-1] + 2\widetilde{G}[i',j-1] + 2\widetilde{\Gamma}[i,i',j-1] - \overline{\Gamma}_q[i,i',j-1] + 3G_2[i',j-1] + 2\Gamma_2[i,i',j-1]\right] \\ &\quad + \frac{1}{2}\Delta^2 \sum_{j'=j-1-i}^{j-2} \alpha_s[i+j'-j+1]\left[Q_q[i+j'-j+1,j'] + 2G_2[i+j'-j+1,j']\right], \end{aligned} \tag{17a}$$

$$\begin{aligned} \overline{\Gamma}_q[i,k,j] &= \overline{\Gamma}_q[i,k-1,j-1] + Q_q^{(0)}[i,j] - Q_q^{(0)}[i,j-1] \\ &\quad + \Delta^2 \sum_{i'=k-1}^{j-2-y_0} \alpha_s[i']\left[\frac{3}{2}Q_q[i',j-1] + 2\widetilde{G}[i',j-1] + 2\widetilde{\Gamma}[i,i',j-1] - \overline{\Gamma}_q[i,i',j-1]\right. \\ &\quad \left. + 3G_2[i',j-1] + 2\Gamma_2[i,i',j-1]\right], \end{aligned} \tag{17b}$$

[2]Note that the $x < x_0$ condition is applied only to our small-x helicity evolution equations. The expressions for the g_1 structure function (4) and the quark (5) and gluon (6) hPDFs remain as shown above: for $x > x_0$ they are driven by the initial conditions/inhomogeneous terms for our evolution (cf. Ref. [103]). The coupling in Eq. (6) runs with Q^2.

$$\widetilde{G}[i,j] = \widetilde{G}[i,j-1] + \widetilde{G}^{(0)}[i,j] - \widetilde{G}^{(0)}[i,j-1] + \Delta^2 \sum_{i'=i}^{j-2-y_0} \alpha_s[i'] \left[3\widetilde{G}[i',j-1] + \widetilde{\Gamma}[i,i',j-1] + 2G_2[i',j-1] + \left(2 - \frac{N_f}{2N_c}\right)\Gamma_2[i,i',j-1] - \frac{1}{4N_c}\sum_q \overline{\Gamma}_q[i,i',j-1] \right] - \Delta^2 \frac{1}{4N_c} \sum_{j'=j-1-i}^{j-2} \alpha_s[i+j'-j+1] \left[\sum_q Q_q[i+j'-j+1,j'] + 2N_f G_2[i+j'-j+1,j'] \right], \tag{17c}$$

$$\widetilde{\Gamma}[i,k,j] = \widetilde{\Gamma}[i,k-1,j-1] + \widetilde{G}^{(0)}[i,j] - \widetilde{G}^{(0)}[i,j-1] + \Delta^2 \sum_{i'=k-1}^{j-2-y_0} \alpha_s[i'] \left[3\widetilde{G}[i',j-1] + \widetilde{\Gamma}[i,i',j-1] + 2G_2[i',j-1] + \left(2 - \frac{N_f}{2N_c}\right)\Gamma_2[i,i',j-1] - \frac{1}{4N_c}\sum_q \overline{\Gamma}_q[i,i',j-1] \right], \tag{17d}$$

$$G_2[i,j] = G_2[i,j-1] + G_2^{(0)}[i,j] - G_2^{(0)}[i,j-1] + 2\Delta^2 \sum_{j'=j-1-i}^{j-2} \alpha_s[i+j'-j+1][\widetilde{G}[i+j'-j+1,j'] + 2G_2[i+j'-j+1,j']], \tag{17e}$$

$$\Gamma_2[i,k,j] = \Gamma_2[i,k-1,j-1] + G_2^{(0)}[i,j] - G_2^{(0)}[i,j-1], \tag{17f}$$

where the numerical step sizes are chosen such that $\Delta\eta = \Delta s_{10} = \Delta s_{21} \equiv \Delta$, and the indices are defined by $\{\eta, s_{10}, s_{21}\} \to \{j,i,k\}\cdot\Delta$. Equation (17) allows us to compute the numerical solution for the flavor singlet evolution equations (9). Note that it is only necessary to loop over the ranges dictated by our physical assumptions, $0 \le i \le k \le j \le j_{\max}$ and $i < j$. Furthermore, it is useful to notice that the neighbor dipole amplitudes reduce to their dipole-amplitude counterparts when $k = i$—that is,

$$\overline{\Gamma}_q[i,k=i,j] = Q_q[i,j], \tag{18a}$$

$$\widetilde{\Gamma}[i,k=i,j] = \widetilde{G}[i,j], \tag{18b}$$

$$\Gamma_2[i,k=i,j] = G_2[i,j]. \tag{18c}$$

We can continue this convention and write the quark and gluon hPDFs from Eqs. (5) and (6) in the new variables,

$$\Delta q^+(x,Q^2) = -\frac{1}{\pi^2}\int_0^{\sqrt{\frac{N_c}{2\pi}}\ln\frac{Q^2}{x\Lambda^2}} \mathrm{d}\eta \int_{\max[0,\eta-\sqrt{\frac{N_c}{2\pi}}\ln\frac{1}{x}]}^{\eta} \mathrm{d}s_{10} \times [Q_q(s_{10},\eta) + 2G_2(s_{10},\eta)], \tag{19}$$

and

$$\Delta G(x,Q^2) = \frac{2N_c}{\alpha_s(Q^2)\pi^2} G_2\left(s_{10} = \sqrt{\frac{N_c}{2\pi}}\ln\frac{Q^2}{\Lambda^2}, \eta = \sqrt{\frac{N_c}{2\pi}}\ln\frac{Q^2}{x\Lambda^2}\right), \tag{20}$$

where the only difference compared to ΔG from Eq. (6) is the running coupling.

The last pieces to consider are the inhomogeneous terms. According to the Born-level initial conditions (11), they can be rewritten using our new logarithmic variables as

$$Q_q^{(0)}(s_{10},\eta) = \widetilde{G}^{(0)}(s_{10},\eta) = \frac{\alpha_s^2 C_F \pi}{2N_c}\sqrt{\frac{2\pi}{N_c}}[(C_F-2)\eta + 2s_{10}], \tag{21a}$$

$$G_2^{(0)}(s_{10},\eta) = \frac{\alpha_s^2 C_F \pi}{2N_c}\sqrt{\frac{2\pi}{N_c}} s_{10}. \tag{21b}$$

Since the equations (21) are linear in η and s_{10}, we follow Ref. [103] and employ the linear expansion ansatz—i.e.,

$$Q_q^{(0)}(s_{10},\eta) = a_q\eta + b_q s_{10} + c_q, \tag{22a}$$

$$\widetilde{G}^{(0)}(s_{10},\eta) = \widetilde{a}\eta + \widetilde{b}s_{10} + \widetilde{c}, \tag{22b}$$

$$G_2^{(0)}(s_{10},\eta) = a_2\eta + b_2 s_{10} + c_2. \tag{22c}$$

Thus, for the three light flavors we consider, $q = u, d, s$, the full set of initial conditions for the flavor singlet evolution depends on 15 parameters $a_u, b_u, c_u, a_d, \ldots, c_2$, which we will fit to the data. Moreover, because the evolution equations we are solving are linear, their solution can be written as a linear combination of 15 "basis" dipole

amplitudes, each of which is constructed by performing the iterative calculation outlined above while setting one parameter (from all the a's, b's, and c's) in Eq. (22) to be 1 and all the other parameters to 0. Furthermore, since all hPDFs and the g_1 structure function depend linearly on the polarized dipole amplitudes, they are linear combinations of their corresponding basis functions as well.

For example, $\Delta u^+(x)$ can be expressed as a linear combination of the 15 "basis hPDFs" shown in Fig. 1. Since $\Delta u^+(x)$ depends directly on the linear combination $Q_u + 2G_2$ [see Eq. (5)], one may expect that Q_u and G_2 have the largest contributions to $\Delta u^+(x)$ at moderate x. This is indeed the case, with the top and bottom panels in Fig. 1 having the largest-magnitude contributions to $\Delta u^+(x)$. Some of the other amplitudes contribute more significantly at lower x's, as their magnitudes begin to influence those of Q_u and/or G_2 through evolution. At the smallest values of x in Fig. 1, the largest contributor is G_2, followed by $\widetilde{G}$, while the contributions from Q_d and Q_s remain small for all values of x.

A consequence of this observation, which we will return to later, is that the sign of the g_1 structure function is influenced mainly by the sign of G_2 (or, equivalently, the

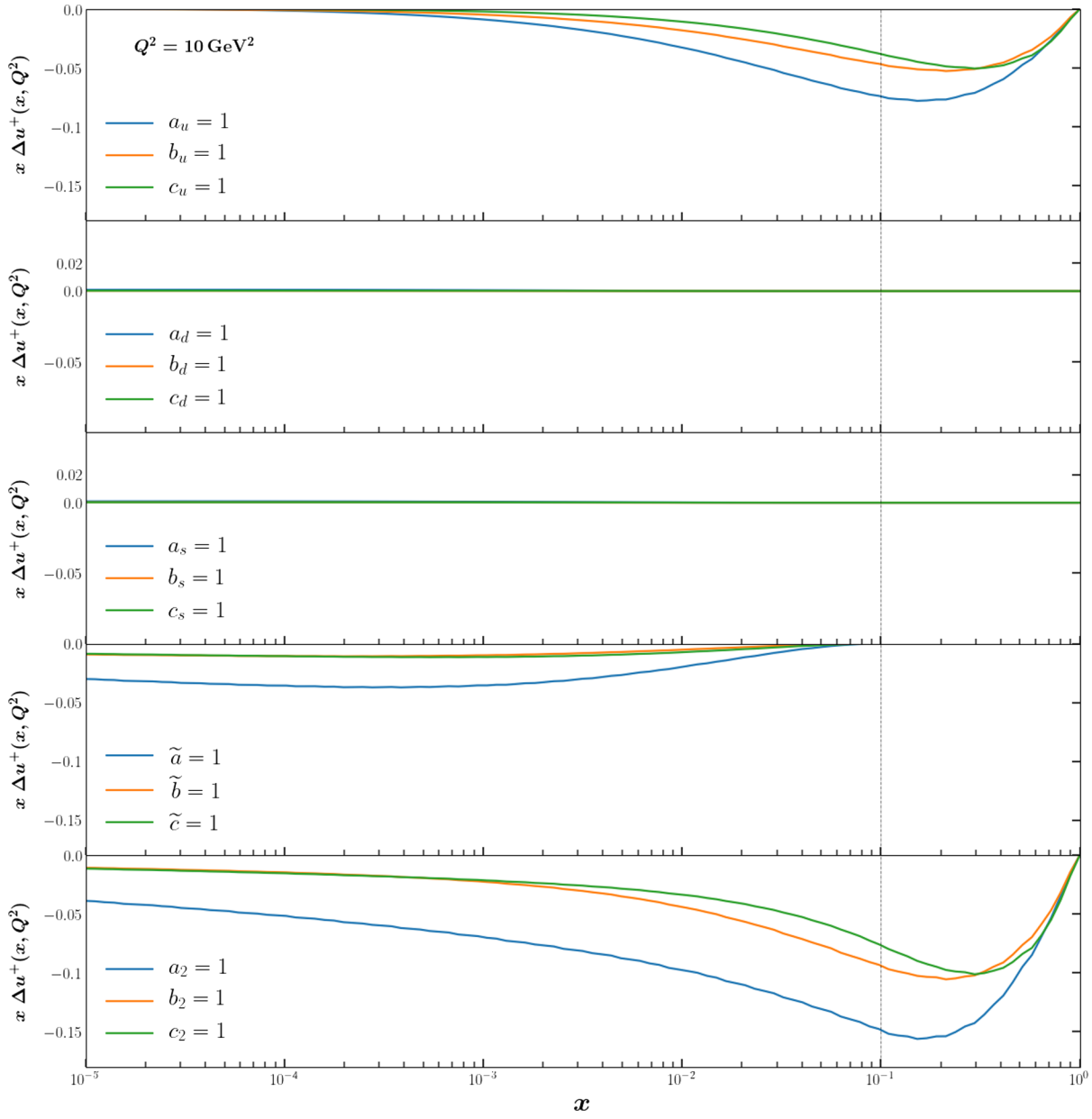

FIG. 1. The u-quark hPDF, $x\Delta u^+(x)$, constructed solely out of each basis function in the range $x \in [10^{-5}, 1]$. The legend in each panel shows which basis function was used for which curve. For example, the blue curve in the top panel corresponds to $x\Delta u^+(x)$ constructed from the initial conditions $Q_u^{(0)} = \eta$ and $Q_q^{(0)} = \widetilde{G}^{(0)} = G_2^{(0)} = 0$ for $q \in \{d, s\}$. The evolution begins at $x_0 = 0.1$, and the coupling constant runs with the daughter-dipole prescription specified in Eq. (A1).

sign of ΔG) and the sign of $\widetilde{G}$. A challenge for phenomenology presents itself: $\widetilde{G}$ is slow to grow and hence less sensitive to available data near $x = x_0$, but it has a potentially large effect on the small-x asymptotics. Unless we have sufficient data from an observable that is directly sensitive to $\widetilde{G}$, constraining that amplitude will be difficult.

Similarly to the singlet evolution, the discretization of the nonsinglet evolution equation (13) reads (again, see Appendix A for details)

$$\begin{aligned} G^{\mathrm{NS}}[i,j] = {} & G^{\mathrm{NS}}[i,j-1] + G^{\mathrm{NS}(0)}[i,j] - G^{\mathrm{NS}(0)}[i,j-1] \\ & + \frac{1}{2}\Delta^2 \Bigg[\sum_{i'=i}^{j-2-y_0} \alpha_s[i'] G^{\mathrm{NS}}[i',j-1] \\ & + \sum_{j'=j-1-i}^{j-2} \alpha_s[i-j+1+j'] \\ & \times G^{\mathrm{NS}}[i-j+1+j',j'] \Bigg]. \end{aligned} \tag{23}$$

The corresponding flavor nonsinglet quark hPDF is given by

$$\begin{aligned} \Delta q^-(x,Q^2) = {} & -\frac{1}{\pi^2} \int_0^{\sqrt{\frac{N_c}{2\pi}} \ln \frac{Q^2}{x\Lambda^2}} \mathrm{d}\eta \\ & \times \int_{\max\left[0, \eta - \sqrt{\frac{N_c}{2\pi}} \ln \frac{1}{x}\right]}^{\eta} \mathrm{d}s_{10} G^{\mathrm{NS}}(s_{10},\eta), \end{aligned} \tag{24}$$

with the integrals also discretized and evaluated numerically. Interested readers are directed to Appendix C for a discussion about convergence testing the numerical solutions of the flavor (non-)singlet evolution equations and the discretized versions of the hPDFs.

The Born-level approximation (14) is linear in the logarithmic variables (15), so we make a linear expansion ansatz for the inhomogeneous term in the flavor nonsinglet evolution,

$$G_q^{\mathrm{NS}(0)} = a_q^{\mathrm{NS}} \eta + b_q^{\mathrm{NS}} s_{10} + c_q^{\mathrm{NS}}, \tag{25}$$

for each of the three light flavors, $q = u, d, s$. This means that flavor nonsinglet hPDFs can be reconstructed as a linear combination of 9 flavor nonsinglet basis functions, generated by setting one of the 9 parameters ($a_u^{\mathrm{NS}}, b_u^{\mathrm{NS}}, \ldots, c_s^{\mathrm{NS}}$) to 1, while setting all others equal to 0. Combining this with the 15 parameters from Eq. (22) describing the inhomogeneous terms for the flavor singlet dipole amplitudes, we have 24 parameters (and associated basis functions) for the eight amplitudes (Q_u, Q_d, Q_s, $\widetilde{G}$, G_2, G_u^{NS}, G_d^{NS}, and G_s^{NS}), which we will fit to describe the world polarized DIS and SIDIS experimental data at low x.

D. SIDIS cross section at small x

We will now derive a formula for the SIDIS structure function $g_1^h(x,z)$ at small x. Using the notation of Ref. [71], we start with the DIS structure function $g_1(x)$ and write it as

$$g_1(x,Q^2) = -\frac{Q^2}{16\pi^2 \alpha_{\mathrm{em}} x} \sum_{\lambda=\pm} \lambda \sigma^{\vec{\gamma}^* + \vec{p} \to X}(\lambda, +), \tag{26}$$

where $\sigma^{\vec{\gamma}^* + \vec{p} \to X}(\lambda, \Sigma)$ is the total virtual-photon–proton cross section for the proton with helicity Σ and for the transversely polarized virtual photon with polarization λ, and α_{em} is the fine structure constant. The virtual-photon–proton cross section is always inelastic at this order in α_{em}, as the virtual photon has to decay into a quark-antiquark pair, with the quark and antiquark fragmenting into hadrons in the final state.

Consider producing a hadron with a fixed value of $z \equiv P \cdot P_h / P \cdot q$, where P and q are the four-momenta of the proton and virtual photon, respectively, while P_h is the momentum of the detected hadron, as shown in Fig. 2. At high energy/small x, we can work in the frame where the proton has a large P^+ momentum component, while the virtual photon has a large q^- momentum component. Then $z \approx P_h^- / q^-$ is the fraction of the virtual photon's minus momentum carried by the produced hadron. All other components of the hadron's momentum are integrated over.

We then write, by analogy to Eq. (26), in the collinear approximation [127–129]

$$\begin{aligned} g_1^h(x,z,Q^2) = {} & -\frac{Q^2}{16\pi^2 \alpha_{\mathrm{em}} x} \sum_{\lambda=\pm} \lambda \int \mathrm{d}^2 k_\perp \mathrm{d}^2 P_{h\perp} \delta^{(2)}(z\mathbf{k}_\perp - \mathbf{P}_{h\perp}) \\ & \times \sum_{q,\bar{q}} \frac{\mathrm{d}\sigma^{\vec{\gamma}^* + \vec{p} \to q + X}}{\mathrm{d}^2 k_\perp}(\lambda, +) D_1^{h/q}(z,Q^2), \end{aligned} \tag{27}$$

where $\mathbf{k}_\perp$ and $\mathbf{P}_{h\perp}$ are the transverse momentum vectors for the quark and produced hadron in Fig. 2, while $D_1^{h/q}(z,Q^2)$ is the collinear fragmentation function. The sum $\sum_{q,\bar{q}}$ goes over the produced quarks and antiquarks. While only quark fragmentation is depicted in Fig. 2, an

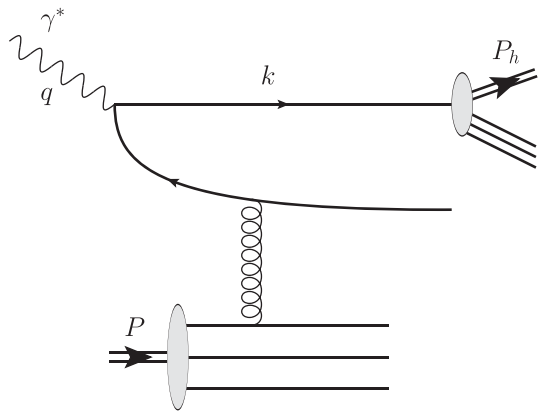

FIG. 2. The SIDIS process at small x. An incoming virtual photon with momentum q decays into a quark-antiquark pair, which interacts with the target proton carrying momentum P. The quark and antiquark then fragment into hadrons, and one of these hadrons is detected with momentum P_h.

antiquark could instead fragment there, by reverting the particle number flow direction on the quark line in the diagram.

In arriving at Eq. (27), we have employed the aligned jet configuration, dominant in DLA [58,71], in which $k^- \approx q^-$, such that the produced hadron carries the fraction $P_h^-/k^- \approx P_h^-/q^- = z$ of the quark's momentum. Consequently, we assume that z is not very small, such that the hadron is produced in the forward (virtual photon) direction/current fragmentation region and arises from the fragmentation of the forward-moving quark with four-momentum k in Fig. 2, and not from the fragmentation of the antiquark, which is separated from the quark by a large rapidity interval. This is similar to the hybrid factorization approach to particle production [130–132]. (The fragmentation of the antiquark in Fig. 2 would contribute to small-z hadron production and is neglected here, since we are interested in order-1 values of z.) In addition, the scale in the argument of the fragmentation function could be chosen to be $k_\perp^2$. However, in our small-x kinematics, the typical value of $k_\perp^2$ is not too far from Q^2, allowing us to use Q^2 in the argument of $D_1^{h/q}(z, Q^2)$.

Integrating Eq. (27) over $\mathbf{k}_\perp$ and $\mathbf{P}_{h\perp}$, we obtain

$$g_1^h(x,z,Q^2) = -\frac{Q^2}{16\pi^2\alpha_{\rm em}x}\sum_{\lambda=\pm}\lambda\sum_{q,\bar{q}}\sigma^{\vec{\gamma}^*+\vec{p}\to q+X}(\lambda,+) \times D_1^{h/q}(z,Q^2). \tag{28}$$

Comparing this to Eqs. (26) and (4), we arrive at

$$g_1^h(x,z,Q^2) = \frac{1}{2}\sum_{q,\bar{q}} e_q^2 \Delta q(x,Q^2) D_1^{h/q}(z,Q^2), \tag{29}$$

reproducing the result in Eq. (2) of Ref. [30] (see also Refs. [127,133,134]), derived in the collinear factorization framework. [As we mentioned above, since quarks and antiquarks have different fragmentation functions, the right-hand side of Eq. (29) cannot be expressed solely in terms of the Δq^+ linear combinations of hPDFs, and the Δq^- functions will enter as well.] We conclude that the expression (29) for the polarized SIDIS structure function is the same in the collinear and small-x formalisms for large z. However, we emphasize that a similar discussion to that surrounding Eqs. (4) and (7) applies to Eq. (29) regarding its interpretation in the LCOT framework as implicitly including higher-order α_s corrections.[3]

[3]Strictly speaking, for consistency, the fragmentation functions $D_1^{h/q}(z, Q^2)$ should also be taken in the polarized DIS scheme, but since the only presently available fragmentation functions are given in the $\overline{\rm MS}$ scheme, we make use of the existing extractions.

E. Global analysis

Our goal is to describe the world data on the longitudinal double-spin asymmetries in DIS and SIDIS at low x using small-x helicity evolution. We start with the longitudinal DIS asymmetry, $A_\parallel$ (see, e.g., Refs. [29,135]),

$$A_\parallel = \frac{\sigma^{\downarrow\Uparrow} - \sigma^{\uparrow\Uparrow}}{\sigma^{\downarrow\Uparrow} + \sigma^{\uparrow\Uparrow}} = D(A_1 + \eta A_2), \tag{30}$$

where the arrow $\uparrow(\downarrow)$ denotes the lepton spin along (opposite to) the beam direction, and the arrow $\Uparrow$ denotes the target polarization along the beam axis. The kinematic variables are given by

$$D = \frac{y(2-y)(2+\gamma^2 y)}{2(1+\gamma^2)y^2 + (4(1-y) - \gamma^2 y^2)(1+R)}, \tag{31a}$$

$$\eta = \gamma\frac{4(1-y) - \gamma^2 y^2}{(2-y)(2+\gamma^2 y)}, \tag{31b}$$

where $y = \nu/E$ is fractional energy transfer of the lepton in the target rest frame, $\gamma^2 = 4M^2x^2/Q^2$, and $R = \sigma_L/\sigma_T$ is the ratio of the longitudinal to transverse virtual photoproduction cross sections. When $4M^2x^2 \ll Q^2 (\gamma^2 \ll 1)$, we have $\eta \ll 1$, and the virtual-photon–target asymmetries are

$$A_1 = \frac{g_1 - \gamma^2 g_2}{F_1} \approx \frac{g_1}{F_1}, \qquad A_2 = \gamma\frac{g_1 + g_2}{F_1} \ll 1, \tag{32}$$

implying

$$A_\parallel \approx D A_1. \tag{33}$$

Similarly, in polarized SIDIS for the production of a hadron h, the asymmetry A_1^h can be expressed as (see, e.g., Refs. [23,30])

$$A_1^h = \frac{g_1^h - \gamma^2 g_2^h}{F_1^h} \approx \frac{g_1^h}{F_1^h}. \tag{34}$$

In principle, there is another observable in the DIS/SIDIS family that could help constrain hPDFs: parity-violating DIS. This process is sensitive to the $g_1^{\gamma Z}$ structure function, which is approximately proportional to $\Delta\Sigma$ [136,137]. Unfortunately, there is little to no data for $g_1^{\gamma Z}$ in the small-x ($x < 0.1$) region (see, e.g., Ref. [138]), not allowing us to employ this observable in our analysis.

Between the two scattering processes, we have ten unique observables: two in DIS (proton or deuteron/^{3}He target) and eight in SIDIS (proton or deuteron/^{3}He target with charged pion or kaon final states) from which in principle we can constrain the eight polarized dipole amplitudes [five associated with the C-even and flavor singlet hPDFs (Q_u, Q_d, Q_s, $\widetilde{G}$, G_2), and three associated with the flavor nonsinglet hPDFs ($G_u^{\rm NS}$, $G_d^{\rm NS}$, and $G_s^{\rm NS}$)].

In our formalism, the g_1 and g_1^h structure functions are calculated in terms of hPDFs using Eqs. (4) and (29), respectively. [Note that $\Delta q = (\Delta q^+ + \Delta q^-)/2$ and $\Delta \overline{q} = (\Delta q^+ - \Delta q^-)/2$.] This is the bridge connecting small-x helicity evolution to the experimental data. Fitting the hPDFs to $A_\parallel$, A_1, and A_1^h at moderate $x \lesssim 0.1$ allows us to determine the initial conditions of the polarized dipole amplitudes (22), (25). We then evolve the polarized dipole amplitudes toward lower values of x using Eqs. (9) and (13) to obtain hPDFs in that region, and compare with existing data, as well as make predictions at smaller x. We mention that the structure functions F_1 and F_1^h involve the unpolarized PDF $q(x, Q^2)$ and, for the latter, the unpolarized fragmentation function (FF) $D_1^{h/q}(z, Q^2)$. We compute F_1 and F_1^h up to next-to-leading order using collinear factorization and DGLAP evolution, based on the JAM analysis in Ref. [34]. (To be consistent, strictly speaking one should include small-x evolution also for F_1 and F_1^h. However, for us the results of Ref. [34] serve as a faithful proxy of the experimental data for these structure functions. A more comprehensive analysis that also utilizes small-x evolution for F_1 and F_1^h is left for future work.)

Let us present a short discussion about our ability to constrain G_2 and $\widetilde{G}$, which are two important polarized dipole amplitudes driving the small-x evolution of the hPDFs. The polarized dipole amplitude G_2 is directly related to the gluon hPDF, per Eq. (20). However, the observables we consider here do not directly couple to the gluon hPDF. Instead, as we saw above, they couple only to quark hPDFs. The dipole amplitude G_2 enters the quark hPDFs Δq^+ along with the dipole amplitude Q_q. Moreover, they always enter in the same linear combination, $Q_q + 2G_2$ for $q = u, d, s$ [see Eq. (19)]. We see that while G_2 and Q_q couple directly to the spin-dependent structure functions for DIS and SIDIS, we do not have an observable (or a linear combination of observables) in this analysis which separately couples only to G_2 or only to Q_q.

What may help us to separate G_2 and Q_q is the fact that these dipole amplitudes have a different preasymptotic form. While it is established numerically that at asymptotically small x, both polarized dipole amplitudes G_2 and Q_q are proportional to the same power of x with the same intercept [102] and are, therefore, probably hard to distinguish, in the preasymptotic region where the asymptotic form has not yet been reached, their contributions to the quark hPDFs may be quite different. This can be studied by comparing the Q_u and G_2 basis functions for Δu^+ in Fig. 1, shown in the top and bottom panels of that figure, respectively. If these functions were identical, they could be freely interchanged against each other while still producing the same structure functions: in such a case, it would be impossible to separate G_2 and Q_u from the data. Since the contributions of different amplitudes to quark hPDFs differ from each other, as follows from Fig. 1, these basis contributions cannot be adjusted at one value of x while maintaining the same value for the observables at all other x. Therefore, we may be able to separate G_2 and Q_u using the polarized DIS and SIDIS data. However, since the Q_u and G_2 basis functions have similar shapes, per Fig. 1, it might be the case that the uncertainties in the resulting extractions of Q_u and G_2 will be large.

The polarized dipole amplitude $\widetilde{G}$, on the other hand, does not couple to any of the polarized DIS or SIDIS observables we consider here. Rather, it mixes with other polarized dipole amplitudes only through evolution [see Eq. (9)]. This is why the $\widetilde{G}$ basis function of Δu^+ (second from the bottom panel in Fig. 1) appears to be vanishingly small above $x > x_0$. The consequence of this is that in the region of x where the polarized DIS and SIDIS data exist, $5 \times 10^{-3} < x < 0.1$, the $\widetilde{G}$ amplitude is very small, and is therefore much less constrained by the data than the Q_q and G_2 dipole amplitudes. At small x, however, the $\widetilde{G}$ amplitude is quite large, second only to G_2 (see Fig. 1). As we will see below, $\widetilde{G}$, unconstrained by the existing polarized DIS and SIDIS data, will dominate over the other polarized dipole amplitudes at small x, adversely affecting our ability to make precise predictions at even smaller x. Nevertheless, it is possible that $\widetilde{G}$ might be constrained with slightly more leverage in x. We will discuss this in Sec. III D when we explore the impact of the future EIC data on our uncertainties.

In our global analysis, we use the JAM Bayesian Monte Carlo framework (see, e.g., [29,139,140]) to randomly sample (roughly 500 times) the space of 24 parameters a, b, c from Eqs. (22) and (25)—namely, $a_u, b_u, c_u, a_d, \ldots, c_s^{\rm NS}$. For each combination of these parameters, we solve our evolution equations (9) and (13) to determine the polarized dipole amplitudes Q_u, Q_d, Q_s, $\widetilde{G}$, G_2, $G_u^{\rm NS}$, $G_d^{\rm NS}$, and $G_s^{\rm NS}$. (The actual numerical solution is facilitated by the basis functions introduced above.) Next, using Eqs. (19) and (24), we calculate the quark hPDFs at small x, which, via Eqs. (4) and (29), can be used to determine the structure functions g_1 and g_1^h that enter the numerator of the asymmetries $A_\parallel, A_1$ [Eqs. (32), (33)] and A_1^h [Eq. (34)], respectively. The χ^2 minimization procedure allows us to construct the posterior distributions of the parameters, and the corresponding solutions of our evolution equations then allow us to infer the quark and gluon hPDFs [the latter via Eq. (20)]. We confirm that the posterior distributions of the parameters are distributed more narrowly than the initial flat sampling and are approximately Gaussian, indicating a convergence in their values. These extracted quark and gluon hPDFs, and the quantities that can be computed from them, are the main results of our work, which we present below.

III. RESULTS

In this section, we present the results of our numerical analysis. We will concentrate on the proton g_1 structure

function, and the quark and gluon hPDFs (along with quantities, such as net spin, that can be computed from them).

A. Data versus theory

Our analysis (JAMsmallx) of the world polarized DIS and SIDIS data at low x utilizes measurements from SLAC [141–145], EMC [146], SMC [147–149], COMPASS [150–152], and HERMES [153,154] for DIS; and from SMC [155], COMPASS [156,157], and HERMES [158,159] for SIDIS. The data of interest fall in the Bjorken-x range of $5 \times 10^{-3} < x < 0.1 \equiv x_0$, and the Q^2 range is $1.69\ \text{GeV}^2 < Q^2 < 10.4\ \text{GeV}^2$. Since $x \approx Q^2/s$, the minimum cut on Q^2 determines the minimum accessible x in the dataset (for a given experimental center-of-mass energy), and conversely the maximum cut on x determines the maximum Q^2. The upper limit on x (denoted by x_0) was chosen based on our previous (DIS-only) work [103], as (almost) the highest value of x which gave a good χ^2 fit. This x_0 is the point where we start the small-x helicity evolution. The fact that our small-x approach was able to describe data up to such a high value of x could be due to the fact that, unlike the unpolarized Balitsky-Fadin-Kuraev-Lipatov (BFKL) [125,126], Balitsky-Kovchegov (BK) [75–78], and Jalilian-Marian–Iancu–McLerran–Weigert–Leonidov–Kovner (JIMWLK) [79–84] small-x evolutions, which resum powers of $\alpha_s \ln(1/x)$ at the leading order, our helicity evolution has a different (larger) resummation parameter, $\alpha_s \ln^2(1/x)$. For $\alpha_s \approx 0.25$, our resumation parameter becomes of order 1 for $x \approx 0.1$, potentially justifying our use of $x_0 = 0.1$ as the starting point for our evolution. Note that the value of our resummation parameter $\alpha_s \ln^2(1/x)$ at $x = x_0 = 0.1$ is comparable to (and even slightly larger than) the value of the resummation parameter $\alpha_s \ln(1/x)$ for the unpolarized small-x evolution at $x = 0.01$, which is where the latter evolution is usually initiated in phenomenological analyses [118,119]. The lower limit of Q^2 is set by the charm quark mass, $m_c^2 = 1.69\ \text{GeV}^2$. This is also the cut placed by the JAM FF set we use [34], which has independent functions for π^+, K^+, h^+ (π^-, K^-, h^- are found through charge conjugation) that we evolve through the DGLAP equations. By analogy to [103], we choose our IR cutoff to be $\Lambda = 1$ GeV. Also, in the Q^2 range specified above, the strong coupling in Eq. (16) is taken with $N_f = 3$ (and $N_c = 3$).

The range of the outgoing hadron momentum fraction z in polarized SIDIS is $0.2 < z < 1.0$, and we do not place any explicit cut on this variable. In practice, the data (after all the appropriate cuts) generally have values of $0.4 < z < 0.6$; some datasets integrate $z \in [0.2, 1]$, while others cover $z \in [0.2, 0.85]$. After all the cuts, we are left with 122 polarized DIS data points and 104 polarized SIDIS data points, for a total $N_{\text{pts}} = 226$. The overall χ^2/N_{pts} of our fit, based on the central theory curves, is 1.03. (We have also performed fits with cutoffs of $x_0 = 0.08$ and $x_0 = 0.05$, which produced no significant change in χ^2/N_{pts}.) The breakdown of the data by experiment, along with our χ^2/N_{pts} for those individual datasets, is shown in Table I for DIS and in Table II for SIDIS. The plots of the experimental data versus our JAMsmallx theory are shown in Fig. 3 for polarized DIS and in Fig. 4 for polarized SIDIS. Overall, our results demonstrate very good agreement with the existing world data.

B. Proton g_1 structure function

We now examine our result for the g_1 structure function of the proton to analyze the predictive capability of our formalism. Our calculation of g_1^p for all replicas is given in Fig. 5. This is the result of 500 individual fits of the experimental data where the (quark and gluon) hPDFs were extracted and then (the quark ones) were used to compute g_1^p. We color code each replica by its asymptotic sign at small x in order to clarify the structure of the plot, as well as to help establish correlations with the hPDFs below. While g_1^p is well constrained in the region where there are experimental data ($5 \times 10^{-3} < x < 10^{-1}$), it is largely unconstrained at smaller x. The major difficulty in

TABLE I. Summary of polarized DIS data included in the fit, separated into A_1 (left) and $A_\parallel$ (right), along with the χ^2/N_{pts} for each dataset.

Dataset (A_1)	Target	N_{pts}	χ^2/N_{pts}
SLAC (E142) [141]	^{3}He	1	0.60
EMC [146]	p	5	0.20
SMC [147,149]	p	6	1.29
	p	6	0.53
	d	6	0.67
	d	6	2.26
COMPASS [150]	p	5	1.02
COMPASS [151]	p	17	0.74
COMPASS [152]	d	5	0.88
HERMES [153]	n	2	0.73
Total		59	0.91

Dataset ($A_\parallel$)	Target	N_{pts}	χ^2/N_{pts}
SLAC (E155) [144]	p	16	1.28
	d	16	1.62
SLAC (E143) [143]	p	9	0.56
	d	9	0.92
SLAC (E154) [142]	^{3}He	5	1.09
HERMES [154]	p	4	1.54
	d	4	0.98
Total		63	1.19

TABLE II. Summary of the polarized SIDIS data on A_1^h included in the fit, along with the $\chi^2/N_{\rm pts}$ for each dataset.

Dataset (A_1^h)	Target	Tagged hadron	$N_{\rm pts}$	$\chi^2/N_{\rm pts}$
SMC [148]	p	h^+	7	1.03
	p	h^-	7	1.45
	d	h^+	7	0.82
	d	h^-	7	1.49
HERMES [158]	p	π^+	2	2.39
	p	π^-	2	0.01
	p	h^+	2	0.79
	p	h^-	2	0.05
	d	π^+	2	0.47
	d	π^-	2	1.40
	d	h^+	2	2.84
	d	h^-	2	1.22
	d	K^+	2	1.81
	d	K^-	2	0.27
	d	$K^+ + K^-$	2	0.97
HERMES [159]	^{3}He	h^+	2	0.49
	^{3}He	h^-	2	0.29
COMPASS [156]	p	π^+	5	1.88
	p	π^-	5	1.10
	p	K^+	5	0.42
	p	K^-	5	0.31
COMPASS [157]	d	π^+	5	0.50
	d	π^-	5	0.78
	d	h^+	5	0.90
	d	h^-	5	0.86
	d	K^+	5	1.50
	d	K^-	5	0.78
Total			104	1.01

constraining g_1^p is caused by the insensitivity of the data to the G_2 and $\widetilde{G}$ amplitudes described above.

That being said, the asymptotic solution of the large-N_c & N_f evolution equations [102] guarantees that the small-x behavior of g_1^p must be exponential in $\ln(1/x)$. This implies that it has to pick a sign (positive or negative) when $x \to 0$. Our results indicate (see Fig. 7) that, given the existing experimental data constraining our formalism, the asymptotic sign is likely to be picked by $x = 3.5 \times 10^{-4}$ with 10% uncertainty, with the uncertainty decreasing to 5% at approximately $x = 2.5 \times 10^{-5}$. Currently, 70% of the replicas are asymptotically positive, and 30% are asymptotically negative. These percentages are stable as the number of replicas increases. The primary source of uncertainty is how low in x one must go to determine the sign, as some replicas that appear positive may undergo a sign change at smaller x. Interestingly, our observation of a preference for g_1^p to be positive at small x agrees with the recent papers analyzing (unpolarized and polarized) DIS structure functions using the anti–de Sitter space/conformal field theory (AdS/CFT) correspondence [160–162] that make an even stronger statement that g_1^p clearly grows positive at small x. This behavior also has implications for the net parton spin expected at small x, as we discuss in Sec. III C.

1. Sign of g_1^p and quantifying numerical ambiguity

From Fig. 5 alone, one can make the qualitative observation that indeed each replica of g_1^p grows exponentially with $\ln(1/x)$, as we suggested earlier, and the color indicates the asymptotic sign of g_1^p for that given replica. We mentioned in the previous section that the exponential behavior of helicity functions in our theory makes it difficult for a given replica to maintain a near-zero value, and thus it must eventually choose to (rapidly) increase in magnitude toward positive or negative values. Given the numerical nature of our global analysis, we cannot compute each fitted replica down to $x = 0$ (corresponding to $\ln x \to -\infty$), so the color-coding and sign assignment is determined by the slope of a replica at the lowest-computed value of x: if the slope increases (decreases) as x goes to zero, then it is considered "asymptotically" positive (negative). To balance our time and computational resources, the results discussed in this section use replica data computed down to $x_{\rm asymp} = 10^{-7.5}$. One may realize potential issues with this system: a given replica may have multiple different "asymptotic" signs depending on the lowest computed value of x.

Any given replica is defined by its specific combination of basis functions, and since our Bayesian analysis samples parameters [Eq. (21)] that may be either positive or negative, competition between basis functions can result in nodes. Replicas with two nodes in $g_1^p(x)$, such as the one illustrated in Fig. 6, can occur for linear combinations of similar basis functions with opposite signs, as in the top/bottom panels of Fig. 1. These changes in sign can occur at various values of x depending on the initial conditions, making the prediction of the asymptotic sign dependent on what x value is used to make the prediction.

Careful readers may have already noticed this from Fig. 5, where there are a few red-coded replicas that appear to be growing negative (and a blue-coded replica that appears to be growing positive) at $x = 10^{-5}$. This is due to each of these replicas having a delayed critical point ($\frac{{\rm d}g_1^p(x)}{{\rm d}x} = 0$) that occurs at $x < 10^{-5}$, where a different basis function takes over the growth and the replica changes the sign of its slope. These critical points also are connected to the issue of *ambiguity*, where at a specific value of x we may be able to measure that a replica is *growing* positive (or negative) but has a magnitude that is actively negative (or positive), leaving its asymptotic sign unconfirmed. Luckily, investigations of these incidents show that they occur in a statistically small portion of replicas from the perspective of our considerably small $x_{\rm asymp}$.

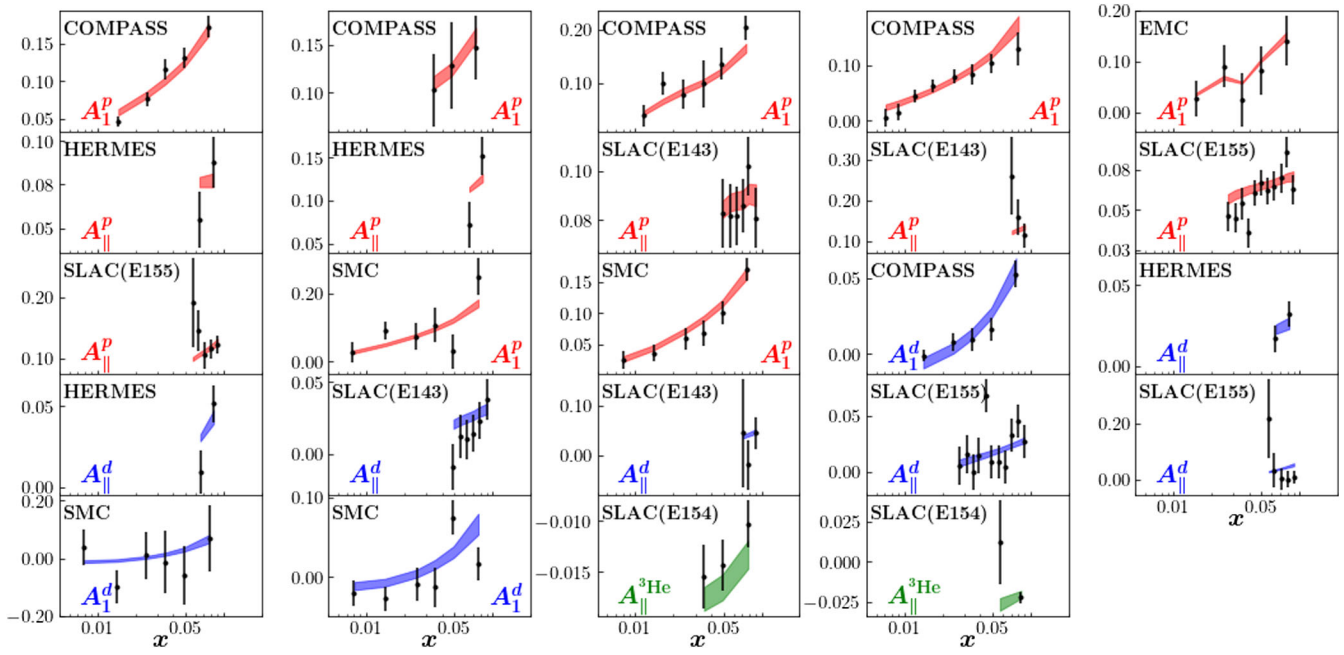

FIG. 3. Comparison of the experimental data and the fit based on our small-x theory for the double-spin asymmetries A_1 and $A_\parallel$ in polarized DIS on a proton (red), deuteron (blue), and ^{3}He (green) target.

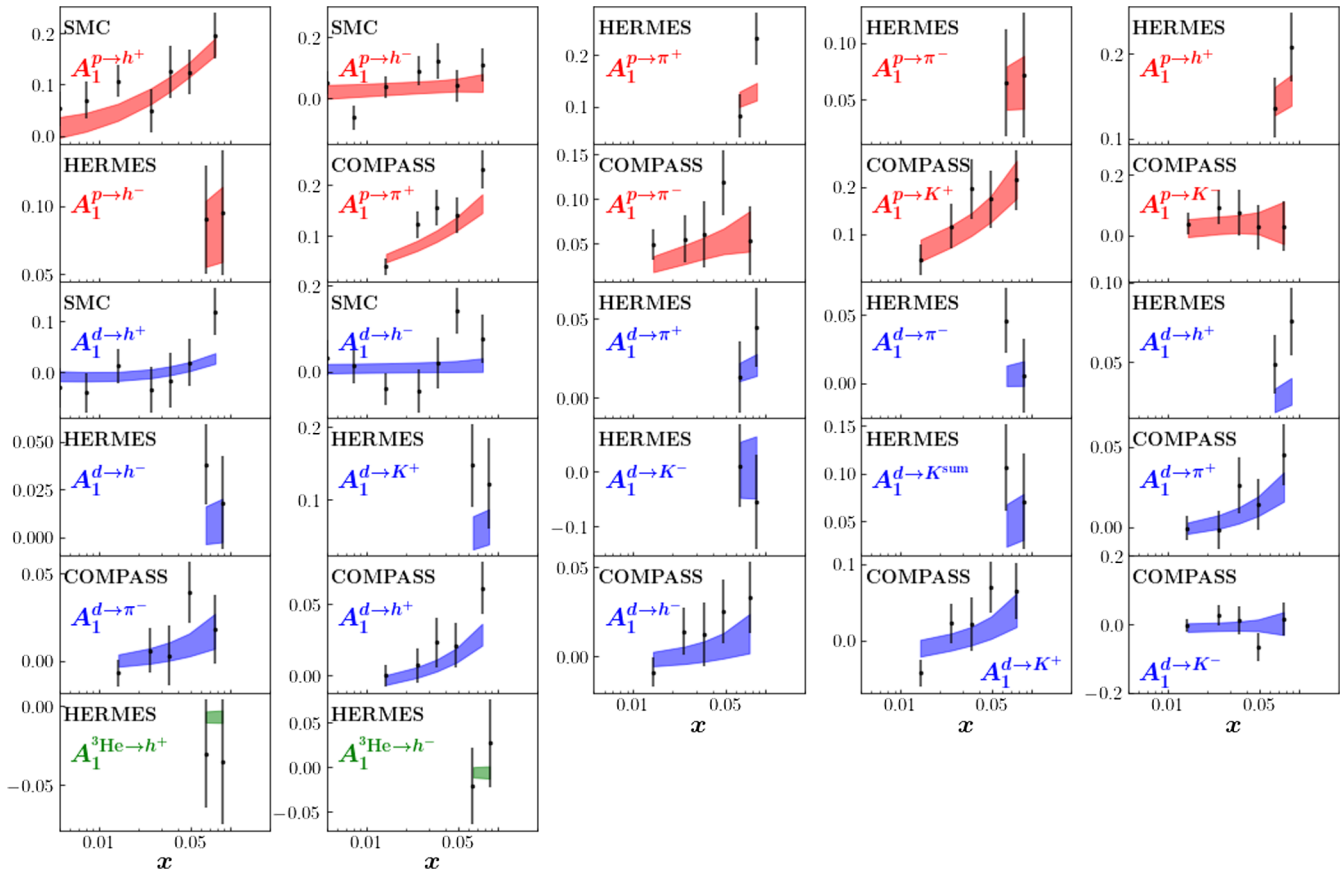

FIG. 4. Comparison of experimental data and fit based on our small-x theory for the double-spin asymmetry A_1^h in polarized SIDIS on a proton (red), deuteron (blue), and ^{3}He (green) target for charged pion, kaon, and unidentified hadron final states.

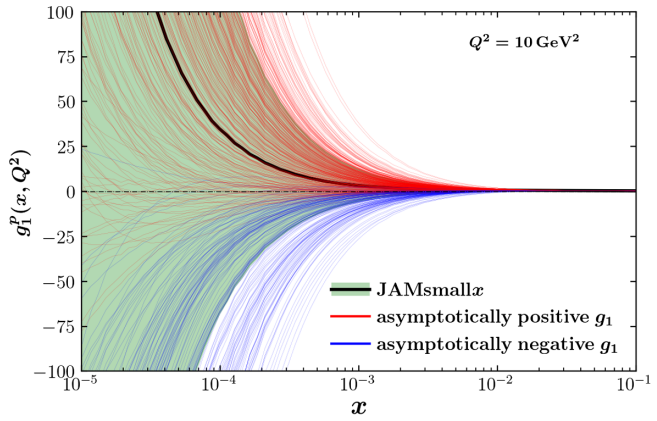

FIG. 5. The small-x calculation of the g_1 structure function of the proton. The black curve is the mean of all the replicas, with the green band giving the 1σ uncertainty. Red (blue) curves are solutions that are asymptotically positive (negative).

Since our goal is predictability at small x, we decided to quantify the amount of ambiguity by its probability density in x. That is, for each replica we count the smallest-x instance of ambiguity and take note of where in x it occurred. For example, Fig. 6 shows a replica that begins positive (true for all replicas), and evolution drives it more positive until it reaches a critical point, after which the replica then grows negative. After the critical point (in the gray region), the replica will be considered *ambiguous* until it crosses $g_1^p(x_1) = 0$, and then it is considered asymptotically negative (in the blue region). Only when the sign of g_1^p and the sign of its first derivative (as x decreases) agree can the replica be considered asymptotically positive or negative. If we wanted to predict the asymptotic sign of the

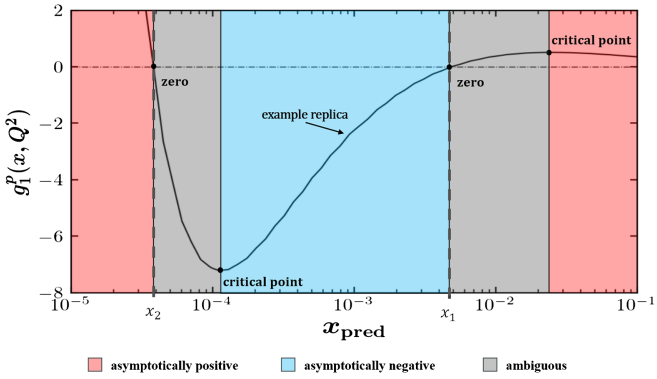

FIG. 6. An example replica of $g_1^p(x, Q^2 = 10\ \mathrm{GeV}^2)$ that demonstrates how the asymptotic sign is dependent on x_{pred}. If x_{pred} resides in the red (blue) region, then the replica will be considered asymptotically positive (negative) according to the sign of the first derivative (for decreasing x) and its agreement with the sign of the magnitude. If x_{pred} resides in either gray region, then the asymptotic sign is ambiguous due to a contradiction between the sign of the slope and the sign of the magnitude.

replica based on an observation at $x = x_{\mathrm{pred}}$ that resides in this (blue) region, then we would predict that this replica is "asymptotically negative" as $x \to 0$. However, this same replica has a small-x critical point (around $x = 10^{-4}$) that causes the sign of its slope to change; the replica observed in the (gray) region (on the left) between the critical point and $g_1^p(x_2) = 0$ would be considered ambiguous again. After crossing zero a second time, a prediction made at $x_{\mathrm{pred}} < x_2$ would therefore designate the replica to be "asymptotically positive." The smallest-x instance of ambiguity is thus counted in a bin at x_2. In this way, each replica is counted exactly once, and replicas that oscillate multiple times about the $g_1^p = 0$ axis only have their most delayed ambiguity counted. We can define the number of replicas that have their smallest-x instance of ambiguity in a particular bin of x as $C_A(x)$ (the counts of ambiguities) and make a histogram. The ambiguity count $C_A(x)$ is normalized such that it sums to the total number of replicas N_{ambig} containing at least one ambiguity:

$$\sum_{x=x_{\mathrm{asymp}}}^{x_0} C_A(x) = N_{\mathrm{ambig}} \leq N_{\mathrm{tot}}. \tag{35}$$

Because some replicas are always unambiguous across the entire range of x, the ambiguity count is less than the total number of replicas: $N_{\mathrm{ambig}} \leq N_{\mathrm{tot}}$.

Now, suppose we want to predict the asymptotic behavior of g_1^p at small x based on the behavior of the function at some value x_{pred}. Knowledge of the ambiguity count $C_A(x)$ allows us to estimate the accuracy of this prediction by estimating the probability that an unobserved ambiguity remains at $x_{\mathrm{asymp}} < x < x_{\mathrm{pred}}$. This probability is given by a summation as in Eq. (35), but over the truncated range in x:

$$\mathcal{A}(x_{\mathrm{pred}}) = \frac{1}{N_{\mathrm{rep}}} \sum_{x=x_{\mathrm{asymp}}}^{x_{\mathrm{pred}}} C_A(x). \tag{36}$$

From the normalization condition (35), we see that Eq. (36) implies that the truncated moment is normalized at $x_{\mathrm{pred}} = x_0$ to the total fraction of replicas containing at least one ambiguity:

$$\mathcal{A}(x_0) = \frac{N_{\mathrm{ambig}}}{N_{\mathrm{rep}}}. \tag{37}$$

From the left panel of Fig. 7, we see that the number of smallest-x ambiguities decreases greatly as x approaches zero. The right panel shows that we must go down to approximately $x = 3.5 \times 10^{-4}$, 2.5×10^{-5}, and 6×10^{-7} to capture the asymptotic sign with 10%, 5%, and 1% uncertainty, respectively. This is strong justification that $x_{\mathrm{asymp}} = 10^{-7.5}$ is reasonably low enough to capture the

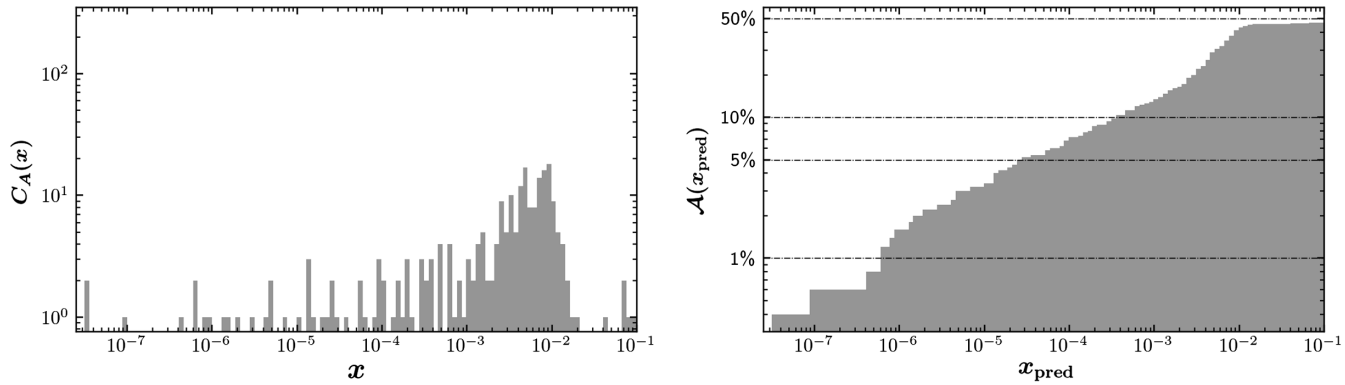

FIG. 7. Left: histogram that counts the number of replicas with a smallest-x ambiguity at a given value of x. Right: the running sum of the ambiguity histogram, telling us what percentage of replicas have an ambiguity below a given value of x.

asymptotic sign of our replicas with low uncertainty. Due to Eq. (37), we also know how many replicas are completely unambiguous; since we impose our evolution to begin at $x_0 = 0.1$, the running integral at that point quantifies the total ratio of replicas that have at least one ambiguity. According to the right panel of Fig. 7, approximately 50% of replicas choose their asymptotic sign immediately as evolution begins. Note that the data constrain the initial condition for g_1^p to be positive, so all completely unambiguous replicas are asymptotically positive.

Furthermore, splitting the replicas by their asymptotic sign (not shown in Fig. 7) allows us to also investigate how early (or late) the different solutions are chosen relative to each other. We gather that ambiguously negative replicas tend to choose their sign earlier than their positive counterparts, with the caveat that the majority of asymptotically positive replicas do not have any ambiguities at all. Approximately 75% of asymptotically positive replicas are completely unambiguous, and the remaining 25% are determined by $x \approx 2 \times 10^{-5}$ with 5% uncertainty. Though fewer in number, a still significant portion of replicas are asymptotically negative, 95% of which are confirmed by $x \approx 4.3 \times 10^{-4}$. This suggests that using a lower $x_{\rm pred}$ will affect the positive-identified and negative-identified solutions differently. In particular, a lower $x_{\rm pred}$ is likely to identify a greater number of asymptotically positive solutions by correcting replicas that would have been misidentified as asymptotically negative at a higher $x_{\rm pred}$. This asymmetric impact on positive-identified versus negative-identified solutions can be traced back to constraints from the data at large x, which strongly prefer $g_1^p > 0$. The fact that this positive preference persists down to small x suggests that the polarized dipole(s) which dominate the small-x asymptotics are partially (but not fully) constrained by the large-x data. This will be discussed in detail in Sec. III B 3.

We performed a similar analysis of the smallest-x critical points of each replica (rather than the ambiguities). On average, the smallest-x critical point occurs 4% earlier in $\ln(1/x)$ than its smallest-x zero. Since the ambiguous region of a replica is precisely the region in x between its critical point and zero, this small 4% difference indicates that any remaining ambiguities are quickly resolved at small x. Thus, we conclude that, from the perspective of Fig. 7, if we had data down to $x \approx 10^{-5}$, we could determine the asymptotic sign of g_1^p with high certainty (>95%).

2. Asymptotic behavior of g_1^p

Collectively utilizing the information in Figs. 5 and 7 paints a curious picture: there are many more g_1^p replicas that adopt their asymptotic forms early than there are replicas that change their signs at small x. This results in some clustering behavior—e.g., in the left panel of Fig. 7 there is a cluster of replicas around $x = 5 \times 10^{-3}$—implying that these replicas share similar critical points and rates of growth. As mentioned previously, the majority of replicas have no ambiguities and adopt their asymptotic growth rather quickly, effectively clustering their critical points at $x = x_0 \equiv 0.1$ (not explicitly shown). This behavior supports the idea that early adoption of asymptotic growth is preferred, whereas replicas with late critical points are fewer in nature. Consequently, we expect that there should be a form of bimodality in g_1^p between the rapidly growing *positive* solutions versus the rapidly growing *negative* solutions. This is a novel result, which we quantitatively analyze below.

While Fig. 5 may appear to show the anticipated bimodality (red versus blue curves), upon closer inspection the values of g_1^p are normally distributed, both at small x ($x = 10^{-3}$) and very small x ($x = 10^{-7.45}$), as depicted in Fig. 8. To uncover the bimodal behavior, it is necessary to construct a new observable related to the *curvature* of g_1^p which is sensitive to how quickly our evolution equations drive the g_1^p replicas toward the asymptotic limit. The emphasis, therefore, is not so much on g_1^p as on the exponent of its power-law behavior at small x—i.e., $g_1^p(x) \sim x^{-\alpha_h}$. The generalized x-dependent exponent

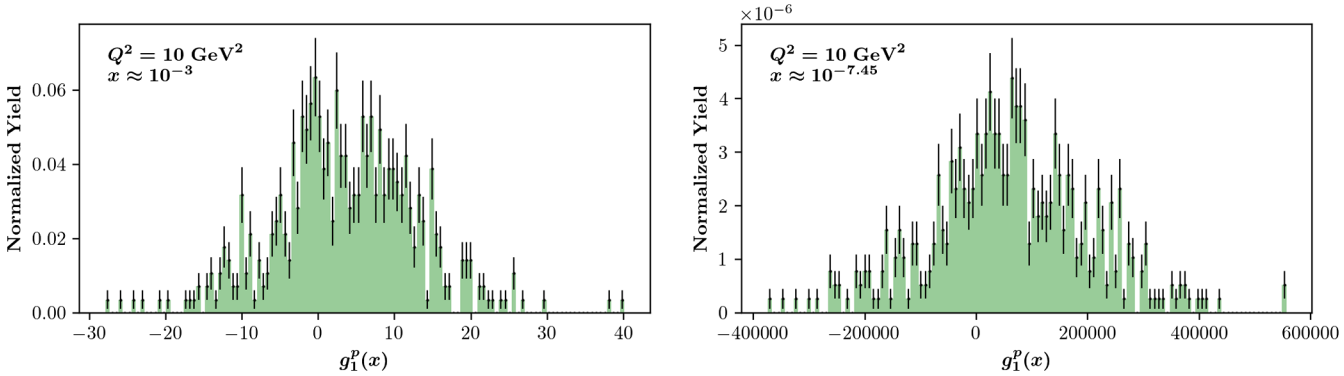

FIG. 8. Histograms counting all values of g_1^p at $x = 10^{-3}$ (left) and $10^{-7.45}$ (right), displaying normal distributions centered slightly above zero.

$\alpha_h(x)$ can be extracted through the logarithmic derivative of g_1^p:

$$\lim_{x\to 0} g_1^p(x) \equiv g_1^{p(0)} x^{-\alpha_h(x)} \;\; \therefore \;\; \alpha_h(x) \equiv \frac{1}{g_1^p(x)} \frac{\mathrm{d}g_1^p(x)}{\mathrm{d}\ln(1/x)}, \quad (38)$$

where $g_1^{p(0)} = \text{const}$. Examining the distribution of $\alpha_h(x)$ across replicas can provide complementary information to the distribution of $g_1^p(x)$ itself. Notably, the exponent provides a meaningful way to scale the solutions: if they have the same $\alpha_h(x)$, they have the same *curvature*, whether the magnitude of $g_1^p(x)$ is large or small. To further capture the *signed* behavior of $g_1^p(x)$ and distinguish between solutions trending positive or negative at small x, we can generalize the logarithmic derivative (38) to reflect the sign of g_1^p itself:

$$\alpha_h(x) = \frac{1}{g_1^p(x)} \frac{\mathrm{d}g_1^p(x)}{\mathrm{d}\ln(1/x)} \Rightarrow$$
$$\mathrm{Sign}[g_1^p(x)]\alpha_h(x) = \frac{1}{|g_1^p(x)|} \frac{\mathrm{d}g_1^p(x)}{\mathrm{d}\ln(1/x)}. \quad (39)$$

Both the effective exponent $\alpha_h(x)$ (38) and its signed generalization (39) are shown in Fig. 9 at varying values of x (from the same global fit that produced Fig. 5).

[We remark that if a g_1^p replica has a delayed critical point, it will result in a delayed zero that may cause an artificially large ratio if $g_1^{p\prime}(x) \gg g_1^p(x) \approx 0$. In order to avoid these statistical outliers, any replica with a ratio value outside of 5σ from the average are omitted from the results in Fig. 9.] The distribution in the right panel at $x = 10^{-2}$ (blue histogram) is skew-normal, which is expected since we are definitively outside of the asymptotic regime. However, at $x = 10^{-3}$ (yellow histogram), we already see the formation of two separated peaks, one positive and one negative. As x continues to decrease down to $x = 10^{-5}$ (green histogram), the two peaks become more refined as the evolution equations predict specific curvature related to the intercept α_h [see Eq. (39)]. Without the sign dependence, as displayed in the left panel of Fig. 9, as $x \to x_{\text{asymp}}$, a single peak emerges that approaches the expected asymptotic value for α_h. The decreasing uncertainties are a consequence of our small-x evolution, where the predictive power constrains the value of $\alpha_h(x)$.

From the perspective of the right panel of Fig. 9, it appears that data sensitive to this curvature at x as large as $x = 10^{-3}$ may be enough to identify which bimodal peak g_1^p belongs to. Unambiguously identifying this curvature will provide us the asymptotic sign of g_1^p as well as the

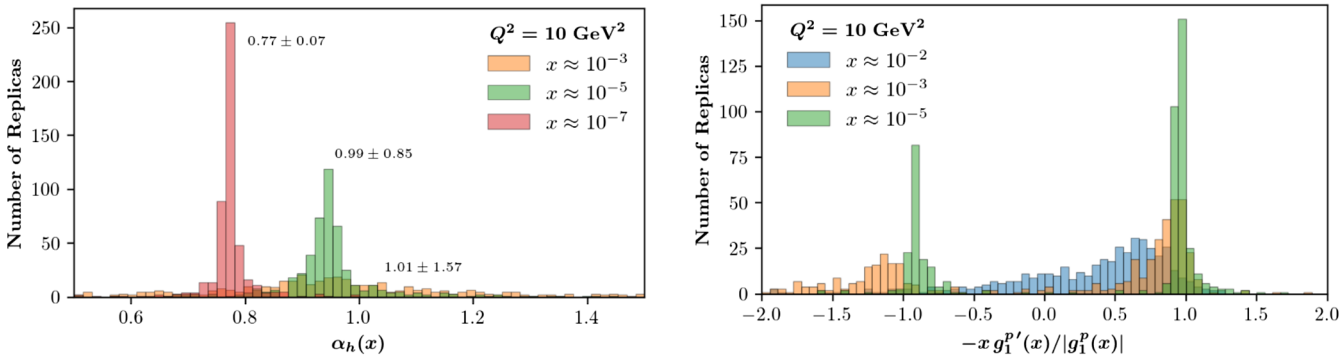

FIG. 9. Left: histograms utilizing Eq. (38) showing that as x decreases, the intercept $\alpha_h(x)$ becomes more constrained as a consequence of the small-x evolution equations. Right: keeping information on the sign dependence by using Eq. (39) produces bimodal peaks at $\pm\alpha_h(x)$. At large x, there is no asymptotic behavior, and for smaller values of x, two refined peaks emerge.

asymptotic sign of all the (flavor singlet and C-even) hPDFs, as will be discussed below. The fact that such a conclusion could be made at $x \approx 10^{-3}$ by analyzing the *curvature* of $g_1^p(x)$, compared to $x \approx 10^{-5}$ by studying $g_1^p(x)$ itself (see the discussion around Fig. 7), makes the idea of curvature a useful quantity to consider once future low-x data are available from the EIC.

3. Origins of asymptotic behavior

To understand what differentiates the positively and negatively growing solutions for g_1^p displayed in Fig. 5, we examine the polarized dipole amplitude parameters themselves, defined in Eq. (22). We note that the experimental data are only sensitive to the polarized dipole amplitudes as a whole, and not to any specific basis function. For example, combining Eqs. (4), (5), and (32) shows that A_1 is constructed from the dipole amplitudes Q_q and G_2, and any combination of parameters that reconstructs the experimental data with good χ^2 is equally valid. An appropriate change of variables can reorganize the basis hPDFs to increase the sensitivity to their overall sign. We can then classify which of these parameters are most correlated with the asymptotic sign of g_1^p. We find enhanced sensitivity to the asymptotic sign of g_1^p from the linear combinations $a' \equiv (a+b)/2$ and $b' \equiv (a-b)/2$. Then, the dipole initial condition $G^{(0)} = a\eta + bs_{10} + c$ can be written as

$$G^{(0)} = a'(\eta + s_{10}) + b'(\eta - s_{10}) + c. \tag{40}$$

These new basis functions are displayed in Fig. 10. Compared to Fig. 1, the alternative parameters a', b' change the shapes of the basis hPDFs. In particular, we note that this greatly increases the separation between the $a_2' = 1$ and $b_2' = 1$ basis functions at large x, where the data provide constraints. When we bin the replicas into asymptotically positive/negative g_1^p at small x, we find that the parameter with the largest difference between the solutions is $\widetilde{a}'$. The asymptotically positive solutions preferred a negative parameter $\widetilde{a}' = -1.56 \pm 2.32$, while the asymptotically negative solutions preferred the positive $\widetilde{a}' = 1.42 \pm 2.34$. No other systematic differences in parameters were observed.

We can understand from the basis hPDFs shown in Fig. 10 why asymptotically positive/negative g_1^p correlates, respectively, with negative/positive values of $\widetilde{a}'$, and why $\widetilde{a}'$ shows the greatest discrimination power. First, we note that the basis hPDFs themselves are negative-definite functions of x for positive values of the initial parameters a', b', c, which is simply a consequence of the explicit minus sign in Eq. (5). Second, we note that the hPDFs arising from both the $\widetilde{G}^{(0)}$ (with parameters $\widetilde{a}'$, $\widetilde{b}'$, $\widetilde{c}$) and $G_2^{(0)}$ (with parameters a_2', b_2', c_2) initial conditions are comparably large at small x; the $a_2' = 1$ basis function also being sizeable at large x, whereas the $\widetilde{a}'$ basis function only contributes meaningfully at small x. The large-x behavior means that the parameter a_2', while important for determining the small-x asymptotics, is constrained by higher-x experimental data, and it specifically prefers *negative* values: $a_2' = -0.98 \pm 1.00$. The origin of the different asymptotic behaviors seen in Fig. 5 therefore appears to be due to the dipole $\widetilde{G}$, which makes no contribution to the basis hPDFs at larger x, and thus, the sign of $\widetilde{a}'$ evades experimental constraints.

To test this hypothesis, we ran fits where all of the $\widetilde{G}$ initial condition parameters ($\widetilde{a}$, $\widetilde{b}$, $\widetilde{c}$) were restricted to be either negative-definite or positive-definite, with all other

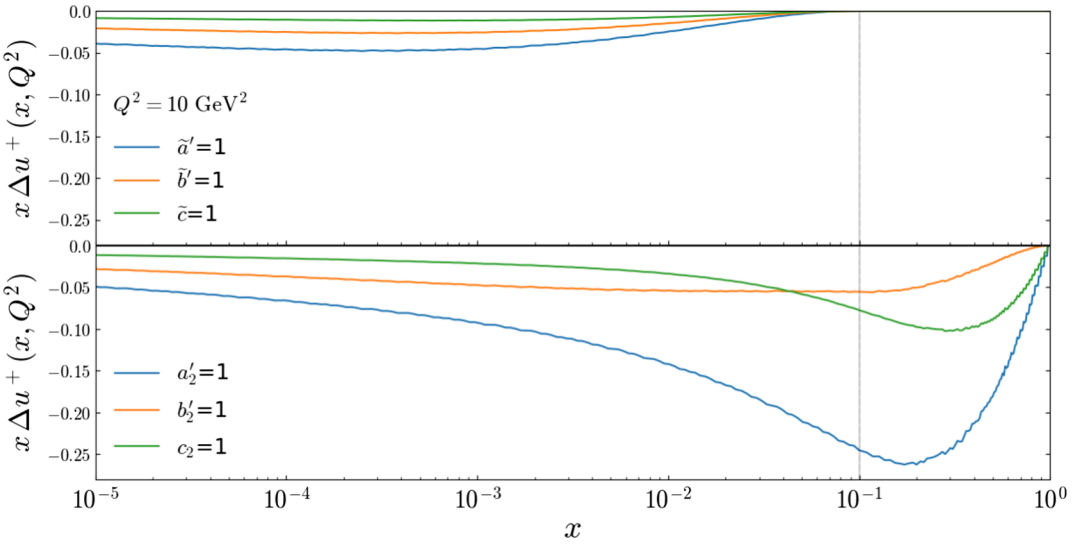

FIG. 10. Basis functions analagous to those in Fig. 1, where instead of plotting the η, s_{10}, and 1 contributions (displayed as the curves in Fig. 1 labeled $a = 1$, $b = 1$, $c = 1$, respectively), we instead show the contributions of $\eta + s_{10}$, $\eta - s_{10}$, and 1 displayed as the curves labeled $a' = 1$, $b' = 1$, and $c' = c = 1$. Here, only the $\widetilde{G}$ and G_2 dipole amplitudes are shown.

parameters unchanged. All g_1^p replicas in the negative-definite $\widetilde{G}$ fit were asymptotically positive. The positive-definite $\widetilde{G}$ fit was slightly less selective but still generated a 73% majority preferring asymptotically negative g_1^p replicas (recall that the original fit in Fig. 5 had a 70% *positive* preference). The results, shown in the top row of Fig. 11, clearly demonstrate that the sign of the $\widetilde{G}$ dipole amplitude determines the small-x asymptotics of g_1^p, as anticipated by the basis functions in Figs. 1 and 10.

The reason $\widetilde{G}$ leads to a g_1^p that is poorly constrained at small x can be seen directly from Eqs. (4)–(6), (9) and Eqs. (12), (13), (29): $\widetilde{G}$ does not contribute directly to any hPDF. Whereas all the other (non-neighbor) polarized dipole amplitudes directly enter a DIS/SIDIS observable, the effects of $\widetilde{G}$ are only felt indirectly through its impact on the evolution of the other amplitudes. As a result, hPDFs mediated by $\widetilde{G}$ only become large at very small x (see the top panel of Fig. 10), where there are no constraints from data.

While $\widetilde{G}$ is the driving factor in determining the small-x asymptotics of g_1^p, G_2 also plays a role. In fact, if $\widetilde{G}$ were removed, G_2 would be the most important amplitude in controlling the small-x asymptotics of g_1^p. We see this explicitly when setting the initial conditions for $\widetilde{G}$ all to zero ($\widetilde{a} = \widetilde{b} = \widetilde{c} = 0$) and repeating the previous analysis of now restricting the G_2 initial condition parameters to be always positive or always negative. The result, shown in the bottom panel of Fig. 11, confirms that, although constrained by large-x data, G_2 plays the second most important role after $\widetilde{G}$ in determining the small-x asymptotics of g_1^p. The negative-definite G_2 fit was 100% selective of asymptotically positive g_1^p replicas, while the positive-definite G_2 fit was 96% selective of asymptotically negative g_1^p replicas.

Figure 11 then compactly summarizes the origin of the asymptotic behavior seen in Fig. 5. The origin of the huge uncertainty band at small x is due to the inability to constrain the sign of $\widetilde{G}$ from large-x data, and the overall preference of the central curve in Fig. 5 favoring positive solutions is due to the fact that there *is* an experimental constraint which prefers $G_2 < 0$, leading to $g_1^p > 0$.

Knowing now that the dipole amplitude $\widetilde{G}$ controls the small-x asymptotics of g_1^p gives us powerful insight into the

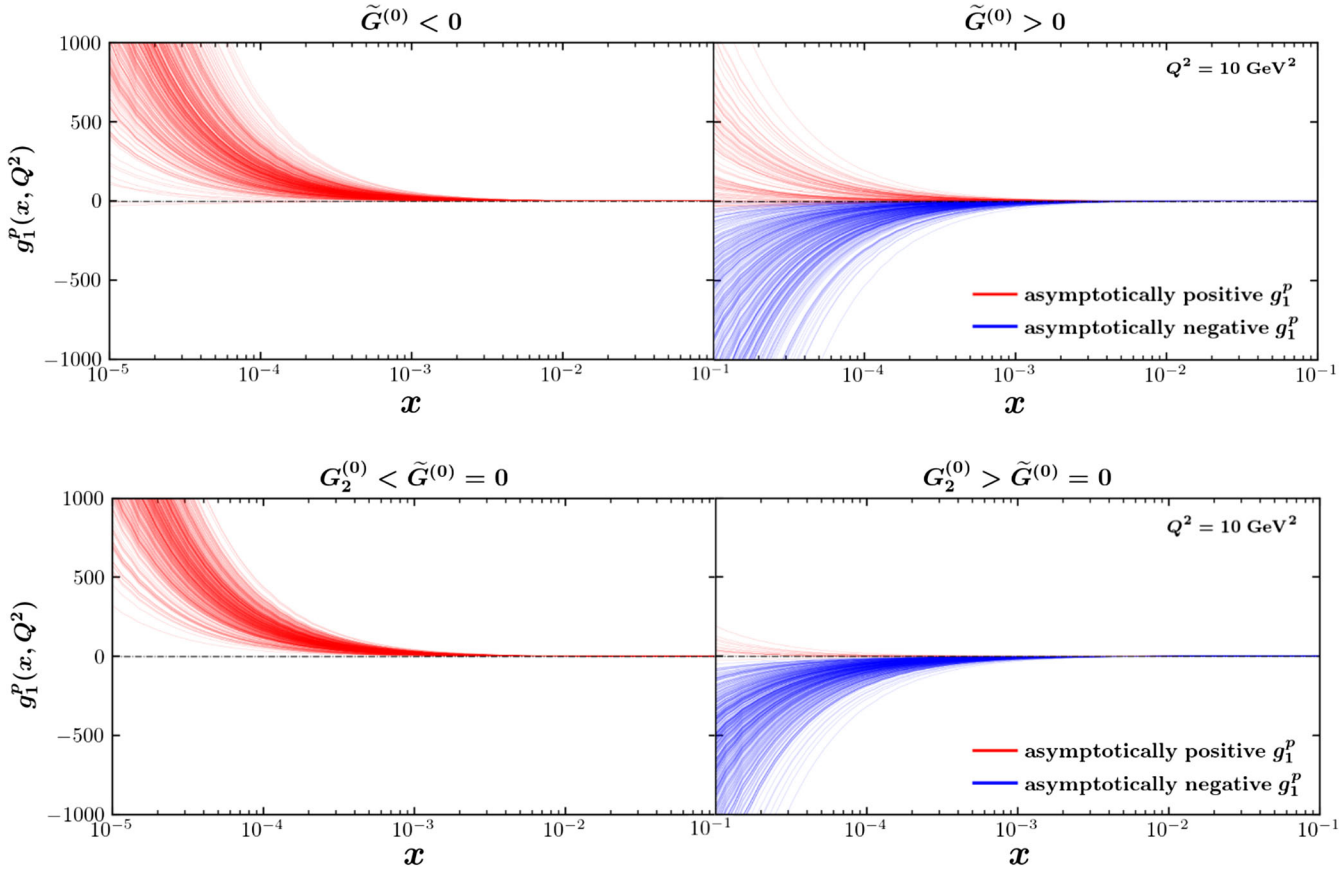

FIG. 11. Comparing the effects $\widetilde{G}$ and G_2 have on the overall sign of $g_1^p(x)$ at small x. Top row: the priors are restricted so that (left) $\widetilde{G} \leq 0$ and (right) $\widetilde{G} \geq 0$. Bottom row: the priors are restricted so that (left) $G_2 < \widetilde{G} = 0$ and (right) $G_2 > \widetilde{G} = 0$. All other parameters initially are randomly sampled just as they were in the fit shown in Fig. 5. We see that controlling the sign of $\widetilde{G}$ strongly influences the sign of g_1^p, and that the sign of G_2 will also influence the sign of g_1^p.

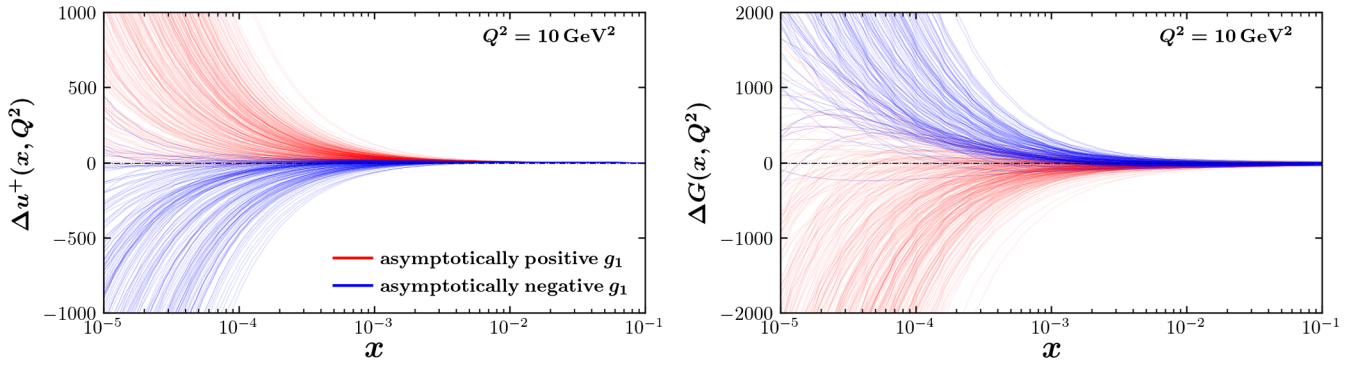

FIG. 12. Color-coding the hPDF replicas according to the asympotic sign of g_1^p shows that there is a novel correlation: at small x, quark hPDFs (left) have the same sign as g_1^p (only Δu^+ is shown), while the gluon hPDF (right) has the opposite sign to g_1^p.

hPDF correlations which characterize the fits. Comparing Eqs. (4), (5), and (6), we can draw the conclusion that at asymptotically small x, these quantities are simply related by

$$g_1^p(x) \propto \Delta q^+(x) \sim -(Q_q + 2G_2) \to -\widetilde{G}, \tag{41a}$$

$$\Delta G(x) \sim G_2 \to \widetilde{G}, \tag{41b}$$

where the last step in each line represents the fact that the evolution of Q_q and G_2 is driven by $\widetilde{G}$ [see Eq. (9)]. At small x, the two hPDFs Δq^+ and ΔG are both driven by the same polarized dipole amplitude $\widetilde{G}$, but they have opposite signs. Since g_1^p is proportional to Δq^+ (weighted by quark electric charge squared and summed over flavors), it follows that if the quark hPDFs for all flavors have the same sign, then at small x, g_1^p will have the same sign as the quark hPDFs and the opposite sign to the gluon hPDF. These anticipated (anti) correlations among the hPDFs are shown in Fig. 12, where we plot only Δu^+ and ΔG for brevity. Note that the color coding used for the replicas in Fig. 12 indicates the ultimate asymptotic sign of g_1^p, not the hPDF itself. That is, an hPDF replica is colored red (blue) if the corresponding g_1^p replica is asymptotically positive (negative). The fact that the asymptotic signs of Δq^+ and ΔG are, respectively, correlated and anticorrelated to the sign of g_1^p at small x is a robust, novel prediction of the small-x helicity evolution framework.[4,5]

[4]We note that no such relationship is exhibited by the nonsinglet hPDFs. When attempting the same strategy of color-coding the nonsinglet hPDFs (not shown) according to the asymptotic sign of the proton SIDIS structure function $g_1^{p\to h}$, no correlations could be identified.

[5]We note that in Ref. [32], a connection was found at small x between $\Delta G(x, Q^2)$ and the $\log Q^2$ derivative of $g_1(x, Q^2)$: $\Delta G(x, Q^2) \approx -\partial g_1(x, Q^2)/\partial \ln Q^2$. Our result, however, demonstrates anticorrelation of the signs of $\Delta G(x, Q^2)$ and $g_1^p(x, Q^2)$ [and not of the log Q^2 derivative of $g_1^p(x, Q^2)$]. In addition, we note that the calculation in Ref. [32] was in a DGLAP-based NLO perturbative QCD framework, while our calculation involves the all-order DLA-resummed coefficient functions [see the discussion around Eq. (7)].

Thus, in order to better predict the asymptotic signs of g_1^p, Δq^+ and ΔG, we need to better constrain the polarized dipole amplitude $\widetilde{G}$. One option is data from the future EIC, discussed in Sec. III D. We also outline several additional ways in Sec. III E.

C. Extracted helicity PDFs and calculation of net parton spin and axial-vector charges at small x

Our results for the hPDFs are shown in Fig. 13. Since our small-x analysis is only valid for $x < x_0 = 0.1$, we restrict the plots to that region. As with the g_1^p structure function shown in Fig. 5, the hPDFs themselves also exhibit broad uncertainty bands at small x.[6] The uncertainty bands for all four hPDFs span zero below $x \lesssim 10^{-3}$, indicating that the hPDFs in that region may be positive, negative, or consistent with zero. By far the largest uncertainty is seen in ΔG, which, unlike Δq^+, is not directly sensitive to inclusive DIS constraints on g_1^p [Eq. (4)]. As shown in Figs. 11 and 12, the large uncertainty in ΔG is due to the lack of sufficient constraints on the dipole amplitudes $\widetilde{G}$ and G_2 that dominate both Δq^+ and ΔG at small x. This conclusion is further supported by the left panel of Fig. 13, where Δu^+, Δd^+, and Δs^+ exhibit approximately the same error band below $x \approx 10^{-4}$. At larger x, where the hPDF behavior is driven more by the Q_q dipole amplitudes, we can observe flavor separation between the three quarks. The uncertainty of the Δs^+ distribution then becomes much larger than that for Δu^+ and Δd^+, most likely due to the limited SIDIS kaon data. The similar error bands at small x for Δu^+, Δd^+, and Δs^+ are in contrast to markedly distinct error bands for Δu^-, Δd^-, and Δs^-, shown in the right panel of Fig. 13, which exhibit significant flavor separation even down to small x. Recall that the flavor nonsinglet hPDFs are driven by a different polarized dipole amplitude,

[6]Note that in Fig. 13, we plot x mutliplied by hPDF on the vertical axis: this explains why the error bands in Fig. 13 appear to be smaller than those in Fig. 16, with the latter showing g_1^p not multiplied by x.

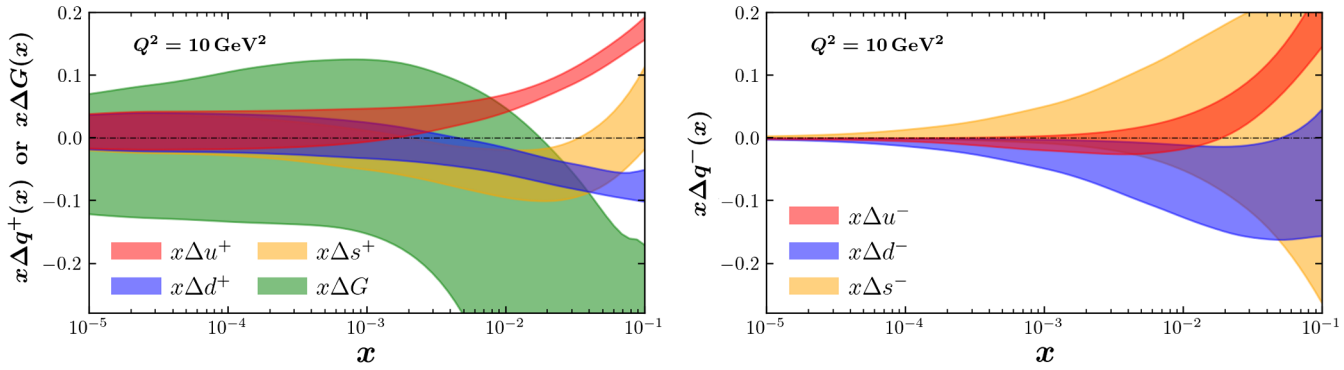

FIG. 13. Left: C-even hPDFs $x\Delta u^+$ (red), $x\Delta d^+$ (blue), $x\Delta s^+$ (orange), and $x\Delta G$ (green) extracted from existing low-x experimental data. Right: same as left panel, but for the flavor nonsinglet C-odd hPDFs $x\Delta u^-$ (red), $x\Delta d^-$ (blue), and $x\Delta s^-$ (orange).

G^{NS} [see Eq. (12)], which is sensitive to flavor separation through the SIDIS data. As a result of the different evolution, the $x\Delta q^-$ distributions converge quickly to zero at small x, unlike the $x\Delta q^+$ distributions, due to the smaller intercept at small x (see also Appendix B). The similarity of the error bands for Δu^+, Δd^+, and Δs^+ appears to be driven by the error band of the polarized dipole amplitude G_2, which affects all quark flavors in the same way, per Eq. (19). Consequently, additional input which can better constrain $\widetilde{G}$ and/or G_2 may well reduce this uncertainty by forcing the hPDFs to choose a definite sign at small x. We discuss possible strategies to achieve this in Sec. III E.

One feature of note in our hPDFs from Fig. 13 is that Δs^+ and ΔG are much larger in magnitude than the same hPDFs obtained in the JAM framework using the DGLAP-based approach [30,33,34]. In particular, our extracted Δs^+ distribution is below zero at about the 1σ level at $x \approx 10^{-2}$. This is to be compared with Fig. 6 of Ref. [33], which exhibits a Δs^+ consistent with zero across the entire considered range $5 \times 10^{-3} \leq x \leq 0.9$. Note that the global analyses conducted in Refs. [30,33,34] are quite different from the one we present here—e.g., they use DGLAP evolution within collinear factorization, include data across the full range of x, and in some cases impose SU(2) and SU(3) flavor symmetries. Nevertheless, it is a valuable cross-check to see whether zero strangeness polarization is consistent with our results as well. To that end, we have separately refit the data, setting the strangeness polarization identically to zero: $\Delta s^+(x, Q^2) = \Delta s^-(x, Q^2) = 0$. The overall quality $\chi^2/N_{\mathrm{pts}} = 1.04$ of the zero-strangeness fit is slightly worse than the quality $\chi^2/N_{\mathrm{pts}} = 1.03$ of the default fit, with the asymmetries A_1^h from tagged kaon SIDIS being the most affected by the change. For that subset of the data, the quality of fit degraded from $\chi^2/N_{\mathrm{pts}} = 0.81$ in the default fit to $\chi^2/N_{\mathrm{pts}} = 1.05$ in the zero-strangeness fit. This marginal degradation of the fit quality is consistent with the 1σ departure of Δs^+ from zero preferred by the default fit in Fig. 13, with the tagged kaon data only accounting for 26/226 data points in total. Therefore, we conclude that small Δs^+ is indeed consistent with our formalism, and that there is a real (but weak) preference from the data for nonzero Δs^+ at $x \sim 0.01$ within our small-x framework.

Next, we address the contribution to the proton spin and axial-vector charges from small x. The flavor singlet quark helicity distribution is given by

$$\Delta\Sigma(x, Q^2) \equiv \Delta u^+(x, Q^2) + \Delta d^+(x, Q^2) + \Delta s^+(x, Q^2) \tag{42}$$

for the light flavors considered in this work. Using the hPDFs in Fig. 13, we show $x\Delta\Sigma(x, Q^2)$ in Fig. 14. Again, the uncertainty band at small x based on current experimental data is rather wide, spanning zero so that the sign of $\Delta\Sigma$ is uncertain.

From $\Delta\Sigma(x, Q^2)$ and $\Delta G(x, Q^2)$, we can determine how much net parton spin [see Eq. (2)] resides at small x by computing truncated moments of the distributions. We can similarly determine the small-x contributions to the triplet g_A and octet a_8 axial-vector charges from truncated moments of the appropriate linear combinations of quark

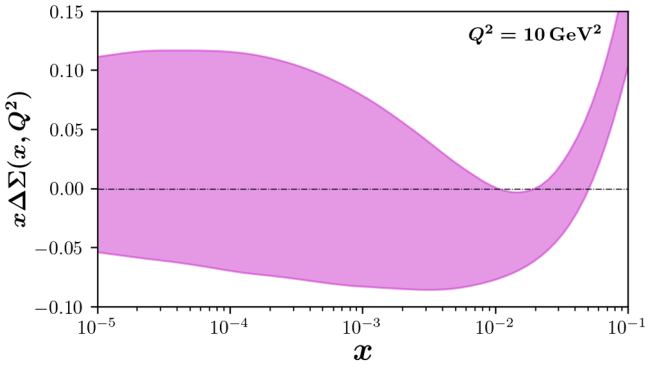

FIG. 14. Quark flavor singlet helicity distribution $x\Delta\Sigma(x, Q^2)$ calculated from hPDFs extracted from existing low-x experimental data.

hPDFs. Focusing on the x region $10^{-5} \leq x \leq 10^{-1}$ of our analysis, we consider the following truncated moments:

$$\left(\frac{1}{2}\Delta\Sigma + \Delta G\right)_{[x_{\max(\min)}]} \equiv \int_{x_1}^{x_2} \mathrm{d}x \left(\frac{1}{2}\Delta\Sigma + \Delta G\right)(x, Q^2), \tag{43a}$$

$$g_{A[x_{\max(\min)}]} \equiv \int_{x_1}^{x_2} \mathrm{d}x\, g_A(x, Q^2) \equiv \int_{x_1}^{x_2} \mathrm{d}x [\Delta u^+(x, Q^2) - \Delta d^+(x, Q^2)], \tag{43b}$$

$$a_{8[x_{\max(\min)}]} \equiv \int_{x_1}^{x_2} \mathrm{d}x\, a_8(x, Q^2) \equiv \int_{x_1}^{x_2} \mathrm{d}x [\Delta u^+(x, Q^2) + \Delta d^+(x, Q^2) - 2\Delta s^+(x, Q^2)]. \tag{43c}$$

Here we consider two representations of the truncated moments: either as a function of the upper limit $x_{\max}$ with fixed lower limit 10^{-5}, or as a function of the lower limit $x_{\min}$ with fixed upper limit 0.1. That is, in the notation of Eq. (43), we have $(x_1, x_2) = (10^{-5}, x_{\max})$ for $[x_{\max}]$ and $(x_1, x_2) = (x_{\min}, 0.1)$ for $[x_{\min}]$. We have also dropped the Q^2 dependence of the truncated moments on the left-hand side of Eq. (43) for brevity.

Both $[x_{\max}]$ and $[x_{\min}]$ representations of the truncated moments are plotted in Fig. 15. From the truncated moment of the total parton helicity $(\frac{1}{2}\Delta\Sigma + \Delta G)_{[x_{\max(\min)}]}$, we conclude that, despite the sizable uncertainties, the amount of the proton spin coming from the net spin of small-x partons could be quite large. The outer bounds of these truncated moments also allow for the possibility that the net quark and gluon spin contained within the small-x region may be even more significant than what has been computed at large x. We observe that, despite the wide error bands in

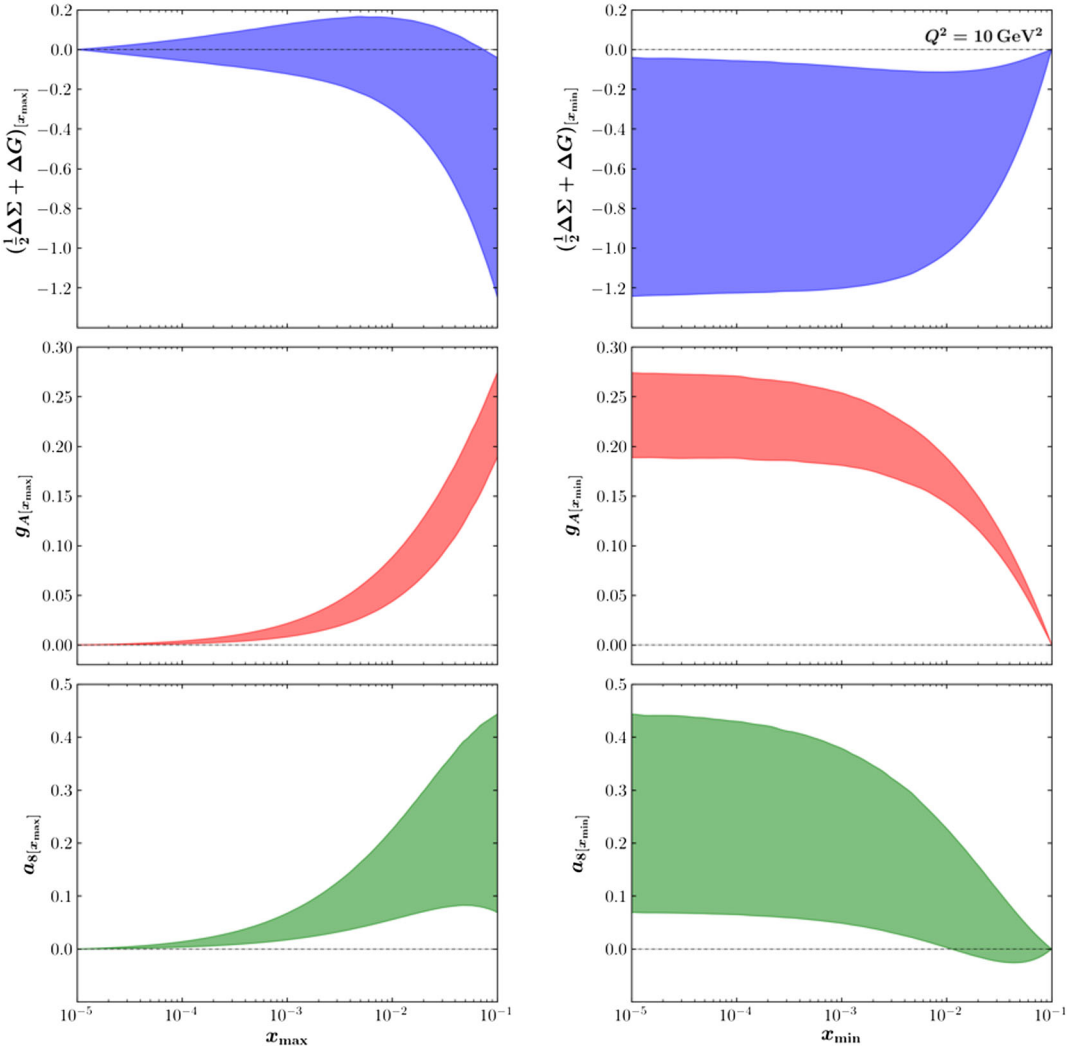

FIG. 15. Truncated moments of $(\frac{1}{2}\Delta\Sigma + \Delta G)(x, Q^2)$, $g_A(x, Q^2)$, and $a_8(x, Q^2)$, defined in Eq. (43), versus $x_{\max}$ (left) and $x_{\min}$ (right) at $Q^2 = 10\ \mathrm{GeV}^2$.

$\Delta G(x,Q^2)$ and $\Delta\Sigma(x,Q^2)$ separately, the error in the truncated moment $(\frac{1}{2}\Delta\Sigma+\Delta G)$ is narrower than if the two were uncorrelated. Because of the replica-by-replica anticorrelation between $\Delta q^+(x,Q^2)$ and $\Delta G(x,Q^2)$ seen in Fig. 12, there is a systematic cancellation between them, resulting in a truncated moment $(\frac{1}{2}\Delta\Sigma+\Delta G)$ which skews net negative and is more tightly constrained than either $\Delta\Sigma(x,Q^2)$ or $\Delta G(x,Q^2)$ alone. In addition, the nonzero slope of $(\frac{1}{2}\Delta\Sigma+\Delta G)_{[x_{\max}]}$ as one approaches $x_{\max}=10^{-5}$ indicates that this truncated moment has not fully saturated at that point in x. In contrast, the small-x contribution to g_A and a_8 appears to saturate around $x=10^{-4}$, giving a finite, non-negligible contribution from small-x partons.

Taken at face value, our formalism strikingly predicts a *negative* contribution to the proton spin from the net spin of small-x partons even when accounting for the 1σ error band. In this scenario favored by our default fit, a significant positive contribution from orbital angular momentum would be needed to satisfy the Jaffe-Manohar sum rule (1). Interestingly, similar observations have been made in using AdS/CFT to analyze g_1^p [160–163]. We also predict that approximately 15%–21% of the known value of g_A and 12%–77% of the known value of a_8 are generated from partons with $10^{-5}\le x\le 10^{-1}$, where the values of the moments over the full range $x\in[0,1]$ are known from neutron and hyperon β decays [24]: $g_A=1.269(3)$ and $a_8=0.586(31)$.

However, we caution the reader that our small-x analysis is strongly dependent on the large-x initial conditions to our evolution, and that the error bands shown throughout this work are *strictly statistical* in nature. These are an accurate representation of the uncertainty coming from the experimental data and from the Monte Carlo sampling procedure, but in particular they do not reflect the systematic bias that comes from omitting large-x data that cannot be captured in this formalism. Combining our small-x evolution equations with external input from large x can therefore possibly result in large, systematic changes to the extracted hPDFs beyond the 1σ statistical error bands. This suggests that an appropriate matching procedure onto hPDFs extracted from a large-x, DGLAP-based analysis like JAM [30,33,34] will be crucial to determining the proton spin budget. Moreover, since JAM found both viable positive $\Delta G(x,Q^2)$ and negative $\Delta G(x,Q^2)$ solutions [33,34], the predictions for the small-x truncated moments may even depend on *which* large-x solution is chosen for the matching. Indeed, as we show in Fig. 18 below, matching to the positive gluon hPDF solution could lead to a substantially different outcome for $\Delta G(x,Q^2)$, deviating beyond the 1σ error band over a significant range of x. Clearly a rigorous implementation of such a matching will be an important aspect of future analyses; a first attempt is detailed in Sec. III E below. Having emphasized this vital caveat, we summarize our results for the small-x truncated moments of $(\frac{1}{2}\Delta\Sigma+\Delta G)(x,Q^2)$, $g_A(x,Q^2)$, and $a_8(x,Q^2)$ over the small-x window $x\in[10^{-5},0.1]$ for $Q^2=10\ \mathrm{GeV}^2$:

$$\int_{10^{-5}}^{0.1}\mathrm{d}x\left(\frac{1}{2}\Delta\Sigma+\Delta G\right)(x)=-0.64\pm0.60, \tag{44a}$$

$$\int_{10^{-5}}^{0.1}\mathrm{d}x\,g_A(x)=0.23\pm0.04, \tag{44b}$$

$$\int_{10^{-5}}^{0.1}\mathrm{d}x\,a_8(x)=0.26\pm0.19. \tag{44c}$$

D. Impact of EIC data on g_1^p

In order to study the impact of lower x measurements on our ability to predict the behavior of g_1^p and the hPDFs at even smaller x, we utilized EIC pseudodata for the kinematic region of $10^{-4}<x<10^{-1}$ and $1.69\,\mathrm{GeV}^2<Q^2<50\,\mathrm{GeV}^2$. The EIC will be capable of going lower in x by reaching higher Q^2, but we do not expect our formalism to be applicable for arbitrarily large Q^2 (DGLAP resummation is needed to fully describe the Q^2 dependence). For DIS on the proton, the pseudodata were at center-of-mass energies $\sqrt{s}=\{29,45,63,141\}$ GeV with an integrated luminosity of 100 fb^{-1}, while for the deuteron and ^{3}He beams the pseudodata spanned $\sqrt{s}=\{29,66,89\}$ GeV with 10 fb^{-1} integrated luminosity. These are consistent with the EIC detector design of the Yellow Report, including 2% point-to-point uncorrelated systematic uncertainties [9]. For SIDIS on a proton, the pseudodata were at $\sqrt{s}=141$ GeV, also with a 2% systematic uncertainty [164]. In our earlier work [103], we had relied on parity-violating DIS pseudodata in order to disentangle the three light quark C-even hPDFs Δq^+. With the inclusion of SIDIS data, that is no longer necessary. The EIC could provide such data [9], and it would serve as an additional constraint in the future, but we do not consider its impact in the present analysis.

Our current extrapolation of g_1^p covers a wide range of possibilities at small x, so we generate the pseudodata based on three scenarios for g_1^p that are consistent with present data: (1) the mean of the asymptotically positive replicas ("high g_1"), (2) the mean of the asymptotically negative replicas ("low g_1"), and (3) the mean of a fit where g_1^p was constrained to have $|g_1^p|<100$ at $x=10^{-4}$ ("mid g_1"). These three options have qualitatively distinct behaviors, and comparing them should inform us if the impact of the EIC is dependent on the precise small-x asymptotics of g_1^p. The results are shown in Fig. 16. We find a dramatic decrease in uncertainties for all three scenarios, even in the extrapolated region of $x<10^{-4}$. In Fig. 17, we plot the relative uncertainty of g_1^p compared to that of a JAM DGLAP-based extraction in Ref. [165] using EIC pseudodata. The results confirm the observation above that, when

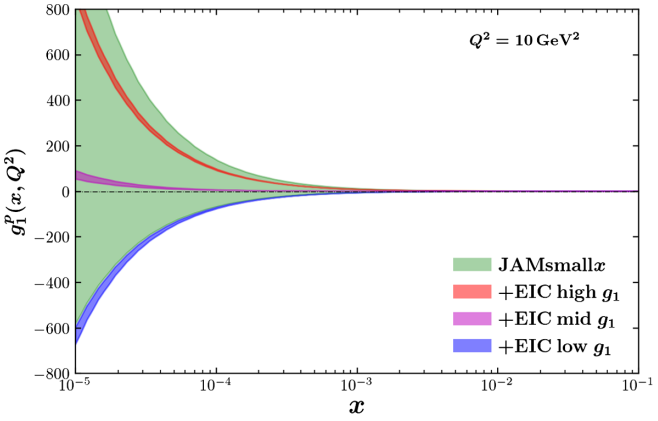

FIG. 16. Extraction of g_1^p from the current low-x experimental data (green, same as Fig. 5) and with EIC pseudodata generated from the mean of the asymptotically positive g_1^p replicas (red), the mean of the asymptotically negative g_1^p replicas (blue), and the mean of replicas restricted such that $|g_1^p| < 100$ at $x = 10^{-4}$ (magenta).

using the genuine predictability of the small-x helicity evolution, control over uncertainties is maintained as we extrapolate to smaller x. In contrast, since the DGLAP-based fit must use an *ad hoc* parametrization of the x dependence, it cannot maintain control over the uncertainties into the extrapolation region.

E. Imposing additional constraints

While future data from the EIC is a promising way to resolve the issue of sizeable uncertainties in our extracted hPDFs at small x, it is worth considering other options that might be more immediately accessible. Ideally, these constraints would enter in the form of existing data or as theoretical constraints on the initial conditions.

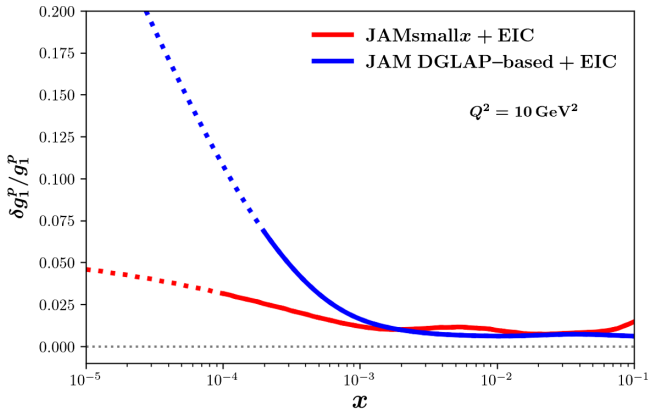

FIG. 17. Relative uncertainty for both this work (red) and a JAM DGLAP-based extraction [165] (blue) for EIC impact studies using the high-g_1^p scenario. Dotted lines denote extrapolating beyond the lowest x for which pseudodata were generated. For this work, pseudodata were generated down to $x = 10^{-4}$. For the JAM DGLAP-based fit, pseudodata were generated down to $x = 2 \times 10^{-4}$ [165].

The hPDF with the largest uncertainty that we have extracted is $\Delta G(x, Q^2)$, as demonstrated in Fig. 13, so we explored a few options to constrain it. The first such constraint is positivity, which is the statement that the number densities for positive- and negative-helicity partons are positive. In particular, for gluons this leads to

$$|\Delta G(x, Q^2)| < G(x, Q^2), \tag{45}$$

where $G(x, Q^2)$ is the unpolarized gluon PDF. (We will set aside issues as to whether Eq. (45) is strictly satisfied under ($\overline{\mathrm{MS}}$) renormalization [166–168].) We impose this constraint by checking the value of $\Delta G(x, Q^2)$ in the region $x < x_0 = 0.1$ and punishing the χ^2 of the fit if the positivity constraint is violated. Unfortunately, by the time our evolution begins, our baseline fit for $\Delta G(x, Q^2)$ and the JAM DGLAP-based $G(x, Q^2)$ [33,34] are of comparable size. The latter grows much faster at small x than our extraction for $\Delta G(x, Q^2)$, causing the positivity constraint to have a negligible effect. This is perhaps not surprising, given that at small x the unpolarized gluon distribution $G(x, Q^2)$ is eikonal, while $\Delta G(x, Q^2)$ is subeikonal, and hence, suppressed by a power of x.

Another constraint on $\Delta G(x, Q^2)$ that we explored was a preliminary matching onto the (large-x) JAM DGLAP-based extraction of $\Delta G(x, Q^2)$ in Refs. [33,34]—in particular, the SU(3)+positivity scenario. The result is shown in Fig. 18; the red box is bounded by $10^{-1.3} < x < 10^{-1}$ and $0.05 < \Delta G(x, Q^2) < 0.2$. The motivation is that any complete description of $\Delta G(x, Q^2)$ should agree with DGLAP extractions in this region. The matching is performed in a simple way, by choosing an intermediate region in x and forcing our fit of $\Delta G(x, Q^2)$ to qualitatively agree with the JAM DGLAP-based extraction. This is done in a similar way to the positivity constraint described above, whereby we punish the χ^2 whenever $\Delta G(x, Q^2)$

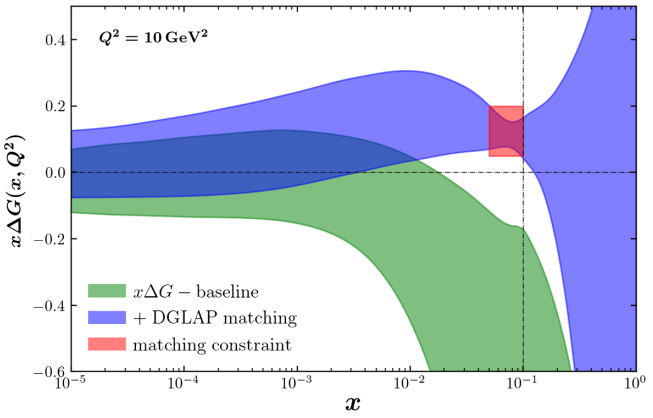

FIG. 18. The result of matching onto the $\Delta G(x)$ extraction from DGLAP [33,34] at intermediate x. The green band is our baseline fit. The blue band is the result of matching. The light red square is the region where we enforce matching.

strays outside of the matching region (red rectangle in Fig. 18). This constraint causes our extracted $\Delta G(x, Q^2)$ to take on mostly positive values at small x, seemingly changing sign from our original extraction. However, note that while the baseline extraction *uncertainty band* grew negative for large x, there were still a significant number of replicas (with good χ^2) that grew positive at large x and overlapped with the red region. Forcing $\Delta G(x, Q^2)$ to pass through that area then preferentially selects those replicas. Consequently, the whole uncertainty band for $\Delta G(x, Q^2)$ remains shifted upward even in the small-x region. Given that $g_1^p(x, Q^2) \propto -\Delta G(x, Q^2)$ [see Eq. (41)], the matching constraint leads to a quantitative change to the distribution of g_1^p replicas: they are now 40% positive and 60% negative. As we emphasized previously, input on hPDFs from large x can have a significant effect on predictions made at small x, motivating future work into a more rigorous matching to DGLAP-based hPDF fits.

Furthermore, the issue with constraining $\widetilde{G}$ could be alleviated by a more rigorous way of handling the starting point of evolution x_0. In this work, we chose $x_0 = 0.1$ and then used experimental data to fit initial conditions for the polarized dipole amplitudes in order to obtain the correct starting values for all of the extracted hPDFs. Only after these starting values have been determined do we then evolve the distributions in a region dominated by our double-logarithmic resummation. In reality, evolution in x begins at $x = 1$, but it is subleading, with the dominant contribution at large x given by DGLAP-driven large-x dynamics. The method of matched asymptotic expansions [169,170] suggests that we start the evolution at $x_0 = 1$, include the DGLAP contributions, but subtract the double-counting of logarithms that are present in both resummations. By starting evolution earlier, $\widetilde{G}$ might become more sensitive to the data. As discussed at the end of Sec. II E, the challenge in constraining $\widetilde{G}$ stems from the fact that it has a small magnitude in the region where there are measurements (see Fig. 1). The magnitude of the $\widetilde{G}$ contribution to Δu^+ is so small at larger x partly because $\widetilde{G}$ enters only through evolution, and evolution is delayed until $x_0 = 0.1$. If $x_0 = 1$, $\widetilde{G}$ will start growing sooner, and it might then have a large enough contribution to be sensitive to the experimental data.

Moreover, perhaps the most direct way to constrain ΔG is to include in the analysis an observable directly sensitive to it. (Recall that in the polarized DIS and SIDIS processes considered here, the contribution from the gluon hPDF is suppressed by a factor of α_s.) Two possibilities, which have been used in DGLAP-based extractions [23,26,27,33,34], are jet and hadron production in polarized proton-proton collisions. The numerator of the double-longitudinal spin asymmetry A_{LL} in $\vec{p} + \vec{p}$ collisions takes the following form:

$$\sigma^{\downarrow\Uparrow} - \sigma^{\uparrow\Uparrow} = \sum_{a,b} \Delta f_{a/A} \otimes f_{b/B} \otimes \sigma_{ab}, \tag{46}$$

where Δf is the parton hPDF for either the quarks or gluon, $a(b)$ is the parton coming from proton $A(B)$, and σ_{ab} is the partonic cross section of parton a interacting with parton b. For hadron production, Eq. (46) needs also to be convoluted with the D_1 FF. More work is needed to derive an analogue of Eq. (46) in the KPS-CTT small-x evolution framework, and initial developments can be found in Ref. [98].

Lastly, in the future, it will also be interesting to attempt to constrain the large-x behavior of the hPDFs by direct matching onto nonperturbative calculations from lattice QCD. Such matching in the vicinity of $x \sim 0.1$ is actually feasible for the double-logarithmic helicity evolution, unlike for the case of single-logarithmic unpolarized small-x evolution, which would require reliable lattice data down to much smaller x. In addition, recently a new approach to determining the initial conditions for small-x evolution by starting at the level of the proton wave function has been developed in Ref. [171]. While that work was done in the context of unpolarized small-x evolution, it is possible that it could be extended to the polarized case, helping us constrain the initial conditions for helicity evolution at hand.

IV. CONCLUSIONS

In this paper, we have presented the first phenomenological implementation of the KPS-CTT theoretical framework [58,64,71] for the evolution of hPDFs. This work represents a significant improvement over our previous study [103] by utilizing the revised evolution equations instead of the original KPS equations. On top of that, we have adopted the large-N_c & N_f limit, which enables a more realistic description of the physics, now including quarks in addition to gluons. Another key advancement of this research is an expansion of our analysis beyond just polarized DIS data by also incorporating polarized semi-inclusive DIS measurements. This allowed us to extract both the C-even and C-odd quark hPDFs Δq^+ and Δq^-, along with the gluon hPDF ΔG. To extract Δq^- we had to, for the first time, implement the numeric solution for the KPS evolution of the nonsinglet hPDFs. Moreover, we have included running coupling corrections in the evolution of Δq^+, Δq^-, and ΔG, which is another feature of the analysis that makes our approach more rigorous.

Through the application of the JAM Bayesian Monte Carlo framework, we have successfully described all available polarized DIS and SIDIS data below the threshold $x_0 = 0.1$, achieving a very good fit with $\chi^2/N_{\text{pts}} = 1.03$. However, when attempting to extend our predictions to lower values of x, the uncertainty associated with our results was found to be substantial. This large uncertainty arises from the inherent insensitivity of the data to the polarized dipole amplitudes G_2 and $\widetilde{G}$. To address this challenge, we discussed several potential future

improvements, among which investigating jet or hadron production in longitudinally polarized proton-proton collisions emerges as a promising medium-term solution. However, more theoretical developments are desirable in the short term, where one must identify the observables which can be expressed in terms of the polarized dipole amplitudes G_2 and $\widetilde{G}$.

Another issue which needs to be clarified in the medium term is the impact of the axial anomaly on the g_1 structure function and hPDFs at small x. The role of the axial anomaly in the polarized structure functions, originally pointed out in Refs. [10,172,173], has been recently revisited in Refs. [174–177]. The effect appears to be distinct from the DLA of BER and KPS-CTT evolution. Developing the corresponding phenomenology is left for future work.

Based on current experimental data, we find that there could be significant *negative* net spin, as well as non-negligible contributions to the triplet and octet axial-vector charges, coming from small-x partons. However, there are large uncertainties in our estimates, including unaccounted-for systematics in matching onto large-x DGLAP-based fits, which will be important to implement in future work. Nevertheless, in such a scenario (negative net parton spin), significant OAM would be needed to satisfy the (Jaffe-Manohar) spin sum rule. The inclusion of EIC data in the long term would greatly enhance our understanding of hPDFs, as our impact study showed, and enable more precise statements about the distribution of (spin and orbital) angular momentum within the proton.

ACKNOWLEDGMENTS

We thank Yiyu Zhou and Chris Cocuzza for providing us replicas and calculations for the JAM DGLAP-based analyses. This work has been supported by the U.S. Department of Energy, Office of Science, Office of Nuclear Physics under Awards No. DE-SC0004286 (D. A. and Y. K.), No. DE-SC0020081 (A. T.), No. DE-AC05-06OR23177 (D. A., W. M., and N. S.) under which Jefferson Science Associates, LLC, manages and operates Jefferson Lab, and the National Science Foundation under Grants No. PHY-2011763 and No. PHY-2308567 (D. P.). The work of N. S. was supported by the DOE, Office of Science, Office of Nuclear Physics in the Early Career Program, and the work of M. S. was supported by the DOE, Office of Science, Office of Nuclear Physics under the Funding for Accelerated, Inclusive Research Program. M. S. would also like to thank the BNL EIC Theory Institute for hospitality and support during the course of this work. This work is also supported by the U.S. Department of Energy, Office of Science, Office of Nuclear Physics, within the framework of the Saturated Glue (SURGE) Topical Theory Collaboration. The work of Y. T. has been supported by the Academy of Finland, the Centre of Excellence in Quark Matter and Project No. 346567, and under the European Union's Horizon 2020 research and innovation program by the STRONG-2020 project (Grant Agreement No. 824093) and by the European Research Council, Grant Agreement No. ERC-2015-CoG-681707. The content of this article does not reflect the official opinion of the European Union, and responsibility for the information and views expressed therein lies entirely with the authors.

APPENDIX A: DISCRETIZATION OF THE FLAVOR SINGLET AND NONSINGLET EVOLUTION EQUATIONS

In this appendix, we present the process of discretizing Eqs. (9) and (13) in order to perform the computation to obtain their numerical solutions. In addition, we implement the constraints corresponding to the fact that the starting point of our evolution is at $x = x_0 < 1$. See the discussion above Eq. (17) for more detail.

We start with the flavor singlet case. Imposing the $\eta - s_{10} > y_0$, $\eta' - s_{21} > y_0$, $\eta'' - s_{32} > y_0$ constraints with $y_0 = \sqrt{\frac{N_c}{2\pi}} \ln \frac{1}{x_0}$, we rewrite Eq. (9) in terms of the variables (15) as

$$\begin{aligned} Q_q(s_{10},\eta) = Q_q^{(0)}(s_{10},\eta) &+ \int_{s_{10}+y_0}^{\eta} d\eta' \int_{s_{10}}^{\eta'-y_0} ds_{21}\alpha_s(s_{21})[Q_q(s_{21},\eta') + 2\widetilde{G}(s_{21},\eta') + 2\widetilde{\Gamma}(s_{10},s_{21},\eta') \\ &- \overline{\Gamma}_q(s_{10},s_{21},\eta') + 2G_2(s_{21},\eta') + 2\Gamma_2(s_{10},s_{21},\eta')] \\ &+ \frac{1}{2}\int_{y_0}^{\eta} d\eta' \int_{\max[0,s_{10}+\eta'-\eta]}^{\eta'-y_0} ds_{21}\alpha_s(s_{21})[Q_q(s_{21},\eta') + 2G_2(s_{21},\eta')], \end{aligned} \tag{A1a}$$

$$\begin{aligned} \overline{\Gamma}_q(s_{10},s_{21},\eta') = Q_q^{(0)}(s_{10},\eta') &+ \int_{s_{10}+y_0}^{\eta'} d\eta'' \int_{\max[s_{10},s_{21}-\eta'+\eta'']}^{\eta''-y_0} ds_{32}\alpha_s(s_{32})[Q_q(s_{32},\eta'') + 2\widetilde{G}(s_{32},\eta'') \\ &+ 2\widetilde{\Gamma}(s_{10},s_{32},\eta'') - \overline{\Gamma}_q(s_{10},s_{32},\eta'') + 2G_2(s_{32},\eta'') + 2\Gamma_2(s_{10},s_{32},\eta'')] \\ &+ \frac{1}{2}\int_{y_0}^{\eta'} d\eta'' \int_{\max[0,s_{21}+\eta''-\eta']}^{\eta''-y_0} ds_{32}\alpha_s(s_{32})[Q_q(s_{32},\eta'') + 2G_2(s_{32},\eta'')], \end{aligned} \tag{A1b}$$

$$\widetilde{G}(s_{10},\eta) = \widetilde{G}^{(0)}(s_{10},\eta) + \int_{s_{10}+y_0}^{\eta} \mathrm{d}\eta' \int_{s_{10}}^{\eta'-y_0} \mathrm{d}s_{21}\alpha_s(s_{21}) \Big[3\widetilde{G}(s_{21},\eta') + \widetilde{\Gamma}(s_{10},s_{21},\eta') + 2G_2(s_{21},\eta') + \left(2-\frac{N_f}{2N_c}\right)\Gamma_2(s_{10},s_{21},\eta') - \frac{1}{4N_c}\sum_q \overline{\Gamma}_q(s_{10},s_{21},\eta') \Big] - \frac{1}{4N_c}\int_{y_0}^{\eta} \mathrm{d}\eta' \int_{\max[0,s_{10}+\eta'-\eta]}^{\min[s_{10},\eta'-y_0]} \mathrm{d}s_{21}\alpha_s(s_{21}) \Big[\sum_q Q_q(s_{21},\eta') + 2N_f G_2(s_{21},\eta') \Big], \tag{A1c}$$

$$\widetilde{\Gamma}(s_{10},s_{21},\eta') = \widetilde{G}^{(0)}(s_{10},\eta') + \int_{s_{10}+y_0}^{\eta'} \mathrm{d}\eta'' \int_{\max[s_{10},s_{21}-\eta'+\eta'']}^{\eta''-y_0} \mathrm{d}s_{32}\alpha_s(s_{32}) \Big[3\widetilde{G}(s_{32},\eta'') + \widetilde{\Gamma}(s_{10},s_{32},\eta'') + 2G_2(s_{32},\eta'') + \left(2-\frac{N_f}{2N_c}\right)\Gamma_2(s_{10},s_{32},\eta'') - \frac{1}{4N_c}\sum_q \overline{\Gamma}_q(s_{10},s_{32},\eta'') \Big] - \frac{1}{4N_c}\int_{y_0}^{\eta'+s_{10}-s_{21}} \mathrm{d}\eta'' \int_{\max[0,s_{21}+\eta''-\eta']}^{\min[s_{10},\eta''-y_0]} \mathrm{d}s_{32}\alpha_s(s_{32}) \Big[\sum_q Q_q(s_{32},\eta'') + 2N_f G_2(s_{32},\eta'') \Big], \tag{A1d}$$

$$G_2(s_{10},\eta) = G_2^{(0)}(s_{10},\eta) + 2\int_{y_0}^{\eta} \mathrm{d}\eta' \int_{\max[0,s_{10}+\eta'-\eta]}^{\min[s_{10},\eta'-y_0]} \mathrm{d}s_{21}\alpha_s(s_{21}) [\widetilde{G}(s_{21},\eta') + 2G_2(s_{21},\eta')], \tag{A1e}$$

$$\Gamma_2(s_{10},s_{21},\eta') = G_2^{(0)}(s_{10},\eta') + 2\int_{y_0}^{\eta'+s_{10}-s_{21}} \mathrm{d}\eta'' \int_{\max[0,s_{21}+\eta''-\eta']}^{\min[s_{10},\eta''-y_0]} \mathrm{d}s_{32}\alpha_s(s_{32}) [\widetilde{G}(s_{32},\eta'') + 2G_2(s_{32},\eta'')]. \tag{A1f}$$

Following Refs. [67,71,102], the evolution equations (A1) can be iterated more optimally by considering the recursive form of their Riemann sums. To do so, we begin by writing Eqs. (A1a), (A1c), and (A1e) as the first-order Taylor expansions in η—e.g.,

$$Q_q(s_{10},\eta+\Delta) = Q_q(s_{10},\eta) + \Delta\frac{\partial}{\partial\eta}Q_q(s_{10},\eta) + \mathcal{O}(\Delta^2), \tag{A2}$$

and Eqs. (A1b), (A1d), and (A1f) as the first-order Taylor expansions in η' and s_{21}—e.g.,

$$\overline{\Gamma}_q(s_{10},s_{21}+\Delta,\eta'+\Delta) = \overline{\Gamma}_q(s_{10},s_{21},\eta') + \Delta\frac{\partial}{\partial\eta'}\overline{\Gamma}_q(s_{10},s_{21},\eta') + \Delta\frac{\partial}{\partial s_{21}}\overline{\Gamma}_q(s_{10},s_{21},\eta') + \mathcal{O}(\Delta^2). \tag{A3}$$

The expansions for other (neighbor) dipole amplitudes are similar. Note that the transverse sizes in neighbor dipoles are always ordered such that $x_{32} < x_{21} < x_{10}$, which implies that $s_{32} > s_{21} > s_{10}$. Neglecting order-Δ^2 terms for small step sizes $\Delta \ll 1$, Eq. (A1) can be written as

$$Q_q(s_{10},\eta+\Delta) = Q_q(s_{10},\eta) + Q_q^{(0)}(s_{10},\eta+\Delta) - Q_q^{(0)}(s_{10},\eta) + \Delta\int_{s_{10}}^{\eta-y_0} \mathrm{d}s_{21}\alpha_s(s_{21}) \Big[\frac{3}{2}Q_q(s_{21},\eta) + 2\widetilde{G}(s_{21},\eta) + 2\widetilde{\Gamma}(s_{10},s_{21},\eta) - \overline{\Gamma}_q(s_{10},s_{21},\eta) + 3G_2(s_{21},\eta) + 2\Gamma_2(s_{10},s_{21},\eta) \Big] + \frac{1}{2}\Delta\int_{\eta-s_{10}}^{\eta} \mathrm{d}\eta'\alpha_s(s_{10}+\eta'-\eta)[Q_q(s_{10}+\eta'-\eta,\eta') + 2G_2(s_{10}+\eta'-\eta,\eta')], \tag{A4a}$$

$$\overline{\Gamma}_q(s_{10},s_{21}+\Delta,\eta'+\Delta) = Q_q(s_{10},\eta) + Q_q^{(0)}(s_{10},\eta+\Delta) - Q_q^{(0)}(s_{10},\eta) + \Delta\int_{s_{21}}^{\eta'-y_0} \mathrm{d}s_{32}\alpha_s(s_{32}) \Big[\frac{3}{2}Q_q(s_{32},\eta') + 2\widetilde{G}(s_{32},\eta') + 2\widetilde{\Gamma}(s_{10},s_{32},\eta') - \overline{\Gamma}_q(s_{10},s_{32},\eta') + 3G_2(s_{32},\eta') + 2\Gamma_2(s_{10},s_{32},\eta') \Big], \tag{A4b}$$

$$\widetilde{G}(s_{10},\eta+\Delta)=\widetilde{G}(s_{10},\eta)+\widetilde{G}^{(0)}(s_{10},\eta+\Delta)-\tilde{G}^{(0)}(s_{10},\eta)$$
$$+\Delta\int_{s_{10}}^{\eta-y_0}\mathrm{d}s_{21}\alpha_s(s_{21})\left[3\widetilde{G}[i',j-1]+\widetilde{\Gamma}(s_{10},s_{21},\eta)\right.$$
$$\left.+2G_2(s_{21},\eta)+\left(2-\frac{N_f}{2N_c}\right)\Gamma_2(s_{10},s_{21},\eta)-\frac{1}{4N_c}\sum_q\overline{\Gamma}_q(s_{10},s_{21},\eta)\right]$$
$$-\Delta\frac{1}{4N_c}\int_{\eta-s_{10}}^{\eta}\mathrm{d}\eta'\alpha_s(s_{10}+\eta'-\eta)\left[\sum_q Q_q(s_{10}+\eta'-\eta,\eta')+2N_fG_2(s_{10}+\eta'-\eta,\eta')\right],\tag{A4c}$$

$$\widetilde{\Gamma}(s_{10},s_{21}+\Delta,\eta'+\Delta)=\widetilde{\Gamma}(s_{10},s_{21},\eta')+\widetilde{G}^{(0)}(s_{10},\eta'+\Delta)-\widetilde{G}^{(0)}(s_{10},\eta')$$
$$+\Delta\int_{s_{21}}^{\eta'-y_0}\mathrm{d}s_{32}\alpha_s(s_{32})\left[3\widetilde{G}(s_{32},\eta')+\widetilde{\Gamma}(s_{10},s_{32},\eta')\right.$$
$$\left.+2G_2(s_{32},\eta')+\left(2-\frac{N_f}{2N_c}\right)\Gamma_2(s_{10},s_{32},\eta')-\frac{1}{4N_c}\sum_q\overline{\Gamma}_q(s_{10},s_{32},\eta')\right],\tag{A4d}$$

$$G_2(s_{10},\eta+\Delta)=G_2(s_{10},\eta)+G_2^{(0)}(s_{10},\eta+\Delta)-G_2^{(0)}(s_{10},\eta)$$
$$+2\Delta\int_{\eta-s_{10}}^{\eta}\mathrm{d}\eta'\alpha_s(s_{10}+\eta'-\eta)[\widetilde{G}(s_{10}+\eta'-\eta,\eta')+2G_2(s_{10}+\eta'-\eta,\eta')],\tag{A4e}$$

$$\Gamma_2(s_{10},s_{21}+\Delta,\eta'+\Delta)=\Gamma_2(s_{10},s_{21},\eta')+G_2^{(0)}(s_{10},\eta'+\Delta)-G_2^{(0)}(s_{10},\eta').\tag{A4f}$$

Next, we discretize the remaining integrals via a left-hand Riemann sum in order to be able to iteratively compute the amplitudes at higher rapidities η, which are required for the calculation of hPDFs and the g_1 structure function at small x. This step is most conveniently performed once we make the change of variables $\{\eta,s_{10},s_{21}\}\to\{j,i,k\}\cdot\Delta$. At the end, Eq. (A4) reduces to the discretized Eq. (17) in the main text.

The numerical implementation of the flavor nonsinglet evolution equation (13) parallels that of the flavor singlet evolution considered above. We use the variable change from Eq. (15) and also require that the flavor nonsinglet evolution start at $x=x_0$, such that $\eta-s_{10}\approx\sqrt{\frac{N_c}{2\pi}}\ln\frac{1}{x}>\sqrt{\frac{N_c}{2\pi}}\ln\frac{1}{x_0}\equiv y_0$. Implementing these modifications in Eq. (13) gives us the following evolution for G^{NS}:

$$G^{\mathrm{NS}}(s_{10},\eta)=G^{\mathrm{NS}(0)}(s_{10},\eta)+\frac{1}{2}\int_{y_0}^{\eta}\mathrm{d}\eta'$$
$$\times\int_{\max[0,s_{10}-\eta+\eta']}^{\eta'-y_0}\mathrm{d}s_{21}\alpha_s(s_{21})G^{\mathrm{NS}}(s_{21},\eta').\tag{A5}$$

The process of discretizing the nonsinglet evolution is mostly similar to that of the singlet evolution. First, we produce a recursion relation using the first-order Taylor expansion, simplify it, and discretize it using the left-handed Riemann sum. Differentiating Eq. (A5) yields

$$\frac{\partial}{\partial\eta}G^{\mathrm{NS}}(s_{10},\eta)=\frac{\partial}{\partial\eta}G^{\mathrm{NS}(0)}(s_{10},\eta)$$
$$+\frac{1}{2}\int_{s_{10}}^{\eta-y_0}\mathrm{d}s_{21}\alpha_s(s_{21})G^{\mathrm{NS}}(s_{21},\eta)$$
$$+\frac{1}{2}\int_{\eta-s_{10}}^{\eta}\mathrm{d}\eta'\alpha_s(s_{10}-\eta+\eta')$$
$$\times G^{\mathrm{NS}}(s_{10}-\eta+\eta',\eta'),\tag{A6}$$

where we have also employed the $s_{10}>0$, $\eta-s_{10}>y_0$ conditions. Using the Taylor expansion in η, cf. Eq. (A2), we obtain a recursive form of our flavor nonsinglet evolution:

$$G^{\mathrm{NS}}(s_{10},\eta)=G^{\mathrm{NS}}(s_{10},\eta-\Delta\eta)+G^{\mathrm{NS}(0)}(s_{10},\eta)$$
$$-G^{\mathrm{NS}(0)}(s_{10},\eta-\Delta\eta)$$
$$+\frac{1}{2}\Delta\eta\int_{s_{10}}^{\eta-y_0}\mathrm{d}s_{21}\alpha_s(s_{21})G^{\mathrm{NS}}(s_{21},\eta)$$
$$+\frac{1}{2}\Delta\eta\int_{\eta-s_{10}}^{\eta}\mathrm{d}\eta'\alpha_s(s_{10}-\eta+\eta')$$
$$\times G^{\mathrm{NS}}(s_{10}-\eta+\eta',\eta').\tag{A7}$$

In order to have a numerical solution consistent with the flavor singlet numerical evolution, we again define $\Delta\eta=\Delta s\equiv\Delta$. We also index our numerics in the same way as in the flavor singlet case, $\{\eta,\eta',s_{10},s_{21}\}\to\{j,j',i,i'\}\cdot\Delta$. Ultimately, Eq. (A7) yields the discretized Eq. (23) in the main text.

APPENDIX B: ANALYTIC CROSS-CHECK OF THE NUMERICAL SOLUTION FOR THE FLAVOR NONSINGLET EVOLUTION

Finding an analytic solution for the large-N_c flavor nonsinglet evolution equation that enforces all of our physical assumptions *and* includes running coupling is, unfortunately, outside the scope of this paper. However, an analytic solution does exist for the large-N_c evolution equations with *fixed* coupling [60], which ignores the $1/\Lambda$ IR cutoff on the transverse size of the dipoles. We can perform a limited cross-check by modifying our numerical solution to use a fixed coupling $\alpha_s = 0.3$, and expand our domain of s_{10} by removing the IR dipole size cutoff, $x_{21} < 1/\Lambda$, employed in Eq. (13). Since the dipole size constraint is enforced by the relation $s_{10} > 0$, we refer to the analytic cross-check regime as the all-s_{10} ($\pm s$) regime.

The revised evolution equation becomes [cf. Eq. (A5)]

$$G^{\mathrm{NS}}_{\pm s}(s_{10},\eta) = G^{\mathrm{NS}(0)}_{\pm s}(s_{10},\eta) + \frac{\alpha_s}{2}\int_0^{\eta} \mathrm{d}\eta' \int_{s_{10}-\eta+\eta'}^{\eta'-y_0} \mathrm{d}s_{21} G^{\mathrm{NS}}_{\pm s}(s_{21},\eta'), \tag{B1}$$

where relaxing the $s_{ij} > 0$ constraint has extended the lower limits of the η' and s_{21} integrals. As expected, changing the phase space of the evolution equation had an effect on our numerical solution, with the discretized flavor nonsinglet equation now being

$$G^{\mathrm{NS}}_{\pm s}[i,j] = G^{\mathrm{NS}}_{\pm s}[i,j-1] + G^{\mathrm{NS}(0)}_{\pm s}[i,j] - G^{\mathrm{NS}(0)}_{\pm s}[i,j-1] + \frac{\alpha_s}{2}\Delta^2\left[\sum_{i'=i}^{j-2-y_0} G^{\mathrm{NS}}_{\pm s}[i',j-1] + \sum_{j'=0}^{j-2} G^{\mathrm{NS}}_{\pm s}[i-j+1+j',j']\right], \tag{B2}$$

where the notable modifications compared to Eq. (23) are the factoring out of the fixed coupling α_s in front of the sum and the different starting point $j' = 0$ of the summation.

We can solve the all-s_{10} evolution equation analytically using Laplace-Mellin transforms (cf. Ref. [60]). To enforce the small-x assumption on our conjugate variables, we define the forward and inverse transforms

$$G^{\mathrm{NS}}_{\pm s}(s_{10},\eta) = \int \frac{\mathrm{d}\omega}{2\pi i} e^{\omega\eta} \int \frac{\mathrm{d}\lambda}{2\pi i} e^{(\eta - s_{10} - y_0)\lambda} G^{\mathrm{NS}}_{\pm s}(\omega,\lambda), \tag{B3a}$$

$$G^{\mathrm{NS}}_{\pm s}(\omega,\lambda), = \int_0^{\infty} \mathrm{d}(\eta - s_{10} - y_0) e^{-\lambda(\eta - s_{10} - y_0)} \times \int_0^{\infty} \mathrm{d}\eta e^{-\omega\eta} G^{\mathrm{NS}}_{\pm s}(s_{10},\eta). \tag{B3b}$$

In Mellin space, the solution presents itself just as it did in Ref. [60],

$$G^{\mathrm{NS}}_{\pm s}(\omega,\lambda) = \frac{\omega\lambda}{\lambda - \frac{\alpha_s}{2\omega}} \frac{1}{\omega} G^{\mathrm{NS}(0)}_{\pm s}(\omega,\lambda). \tag{B4}$$

This is convenient, since we only have three distinct initial conditions: $G^{\mathrm{NS}(0)}_{\pm s} = \eta, s_{10}, 1$. First, we will evaluate the nonsinglet evolution beginning with the constant contribution, $G^{\mathrm{NS}(0)}_{\pm s}(\eta, s_{10}) = 1$.

$$G^{\mathrm{NS}(0)}_{\pm s}(\omega,\lambda) = \int_0^{\infty} d(\eta - s_{10} - y_0) e^{-\lambda(\eta - s_{10} - y_0)} \int_0^{\infty} \mathrm{d}\eta\, e^{-\omega\eta} = \frac{1}{\omega\lambda}. \tag{B5}$$

Plugging this into the evolution equation leads to another contour integral with a pole at $\lambda = \alpha/(2\omega)$, which is evaluated via the residue theorem to give

$$G^{\mathrm{NS}}_{\pm s}(\eta, s_{10}) = \int \frac{\mathrm{d}\omega}{2\pi i} e^{\omega\eta} \int \frac{\mathrm{d}\lambda}{2\pi i} e^{(\eta - s_{10} - y_0)\lambda} \frac{1}{\lambda - \frac{\alpha_s}{2\omega}} \frac{1}{\omega} = \int \frac{\mathrm{d}\omega}{2\pi i} e^{\omega\eta + \frac{\alpha_s}{2\omega}(\eta - s_{10} - y_0)} \frac{1}{\omega}. \tag{B6}$$

Now we can Taylor-expand the singular ($\sim 1/\omega$) part of the exponential, use the residue theorem, and simplify the result, obtaining

$$G^{\mathrm{NS}}_{\pm s}(\eta, s_{10}) = \int \frac{\mathrm{d}\omega}{2\pi i} e^{\omega\eta} \sum_{n=0}^{\infty} \frac{1}{n!} \left(\frac{\alpha_s(\eta - s_{10} - y_0)}{2\omega}\right)^n \frac{1}{\omega} = \sum_{n=0}^{\infty} \frac{1}{(n!)^2} \left(\frac{\alpha_s}{2}\eta(\eta - s_{10} - y_0)\right)^n. \tag{B7}$$

This infinite sum is equivalent to the modified Bessel function of the first kind, $I_m(z)$ at $m = 0$,

$$G^{NS,1}_{\pm s}(\eta, s_{10}) = I_0(\sqrt{\alpha_s}\sqrt{2\eta(\eta - s_{10} - y_0)}). \tag{B8}$$

This process is repeated for the η initial condition, $G^{\mathrm{NS}(0)}_{\pm s}(\eta, s_{10}) = \eta$, giving

$$G^{\mathrm{NS}(0)}_{\pm s}(\omega,\lambda) = \int_0^{\infty} \mathrm{d}(\eta - s_{10} - y_0) e^{-\lambda(\eta - s_{10} - y_0)} \int_0^{\infty} \mathrm{d}\eta\, e^{-\omega\eta}\eta = \frac{1}{\omega^2\lambda}. \tag{B9}$$

This contour integral has the same pole at $\lambda = \alpha_s/(2\omega)$, resulting in a similar integral,

$$G^{\mathrm{NS}}_{\pm s}(\eta, s_{10}) = \int \frac{\mathrm{d}\omega}{2\pi i} e^{\omega\eta + \frac{\alpha}{2\omega}(\eta - s_{10} - y_0)} \frac{1}{\omega^2}. \tag{B10}$$

We use the same Taylor expansion and the above expression for the ω contour integral to obtain

$$G^{\rm NS}_{\pm s}(\eta, s_{10}) = \int \frac{{\rm d}\omega}{2\pi i} e^{\omega\eta} \sum_{n=0}^{\infty} \frac{1}{n!} \left(\frac{\alpha_s(\eta - s_{10} - y_0)}{2}\right)^n \frac{1}{\omega^{n+2}}$$
$$= \eta \sum_{n=0}^{\infty} \frac{1}{(n!)(n+1)!} \times \left(\frac{\alpha_s}{2}\eta(\eta - s_{10} - y_0)\right)^n. \quad \text{(B11)}$$

This, too, is proportional to a modified Bessel function of the first kind, now for $m = 1$. The solution is then rewritten as

$$G^{{\rm NS},\eta}_{\pm s}(\eta, s_{10}) = \frac{1}{\sqrt{\alpha_s}} \sqrt{\frac{2\eta}{\eta - s_{10} - y_0}} I_1(\sqrt{\alpha_s}\sqrt{2\eta(\eta - s_{10} - y_0)}). \quad \text{(B12)}$$

Lastly, we must solve for the initial condition term $G^{\rm NS}_{\pm s}(\eta, s_{10}) = s_{10}$. Noting that $s_{10} = \eta - (\eta - s_{10} - y_0) - y_0$,

$$G^{\rm NS(0)}_{\pm s}(\omega, \lambda) = \int_0^{\infty} {\rm d}(\eta - s_{10} - y_0) e^{-\lambda(\eta - s_{10} - y_0)} \times \int_0^{\infty} {\rm d}\eta\, e^{-\omega\eta} (\eta - (\eta - s_{10} - y_0) - y_0)$$
$$= \frac{\lambda - \omega - y_0\omega\lambda}{(\omega\lambda)^2}. \quad \text{(B13)}$$

In this case, we have two poles: $\lambda = 0$, $\alpha_s/(2\omega)$. Conveniently, there are no poles in ω at $\lambda = 0$, so that particular integral vanishes. Moving forward with the other λ pole, we write

$$G^{\rm NS}_{\pm s}(\eta, s_{10}) = \int \frac{{\rm d}\omega}{2\pi i} e^{\omega\eta} \int \frac{{\rm d}\lambda}{2\pi i} e^{(\eta - s_{10} - y_0)\lambda} \frac{\omega\lambda}{\lambda - \frac{\alpha_s}{2\omega}} \times \frac{1}{\omega} \frac{\lambda - \omega - y_0\omega\lambda}{(\omega\lambda)^2}$$
$$= \int \frac{{\rm d}\omega}{2\pi i} e^{\omega\eta + \frac{\alpha_s}{2\omega}(\eta - s_{10} - y_0)} \left(\frac{1}{\omega^2} - \frac{2}{\alpha_s} - \frac{y_0}{\omega}\right). \quad \text{(B14)}$$

This equation is a linear combination of the two other contributions we derived, plus a new term. This new term can be evaluated in the same way as the previous two. We obtain the following result for the s_{10} contribution:

$$G^{{\rm NS},s_{10}}_{\pm s}(\eta, s_{10}) = \frac{1}{\sqrt{\alpha_s}} \sqrt{\frac{2\eta}{\eta - s_{10} - y_0}} I_1(\sqrt{\alpha_s}\sqrt{2\eta(\eta - s_{10} - y_0)}) - \frac{1}{\sqrt{\alpha_s}} \sqrt{\frac{2(\eta - s_{10} - y_0)}{\eta}} I_1(\sqrt{\alpha_s}\sqrt{2\eta(\eta - s_{10} - y_0)}) - y_0 I_0(\sqrt{\alpha_s}\sqrt{2\eta(\eta - s_{10} - y_0)}). \quad \text{(B15)}$$

In the end, we arrive at an analytic solution for the flavor nonsinglet evolution equation in the all-s_{10} regime,

$$G^{\rm NS}_{\pm s}(\eta, s_{10}) = a^{\rm NS} G^{NS,\eta}_{\pm s} + b^{\rm NS} G^{NS,s_{10}}_{\pm s} + c^{\rm NS} G^{NS,1}_{\pm s}$$
$$= a^{\rm NS} \frac{1}{\sqrt{\alpha_s}} \sqrt{\frac{2\eta}{\eta - s_{10} - y_0}} I_1\left(\sqrt{\alpha_s}\sqrt{2\eta(\eta - s_{10} - y_0)}\right) + \frac{b^{\rm NS}}{\sqrt{\alpha_s}} \sqrt{\frac{2\eta}{\eta - s_{10} - y_0}} I_1\left(\sqrt{\alpha_s}\sqrt{2\eta(\eta - s_{10} - y_0)}\right)$$
$$- \frac{b^{\rm NS}}{\sqrt{\alpha_s}} \sqrt{\frac{2(\eta - s_{10} - y_0)}{\eta}} I_1\left(\sqrt{\alpha_s}\sqrt{2\eta(\eta - s_{10} - y_0)}\right) - b^{\rm NS} y_0 I_0\left(\sqrt{\alpha_s}\sqrt{2\eta(\eta - s_{10} - y_0)}\right)$$
$$+ c^{\rm NS} I_0\left(\sqrt{\alpha_s}\sqrt{2\eta(\eta - s_{10} - y_0)}\right). \quad \text{(B16)}$$

The first place to start our comparisons would be the dipole amplitudes themselves. There are three properties of the flavor nonsinglet dipole amplitudes that we can use to cross-check the numerical solution: the general shape of the amplitudes, a sign change in the s_{10} contributions due to the positive starting point and negative growth, and the asymptotic behavior at small x. The last property is also useful for checking the implementation of our hPDF calculation, since the dipole amplitudes and hPDFs should have the same asymptotics.

We show in Fig. 19 high-resolution (small step size) numerical solutions of the polarized dipole amplitudes, as functions of η for a fixed s_{10}, compared to their analytic counterparts. The general shape and growth of the flavor nonsinglet amplitudes (see the left panels in Fig. 19) shows a good agreement between the numerical and

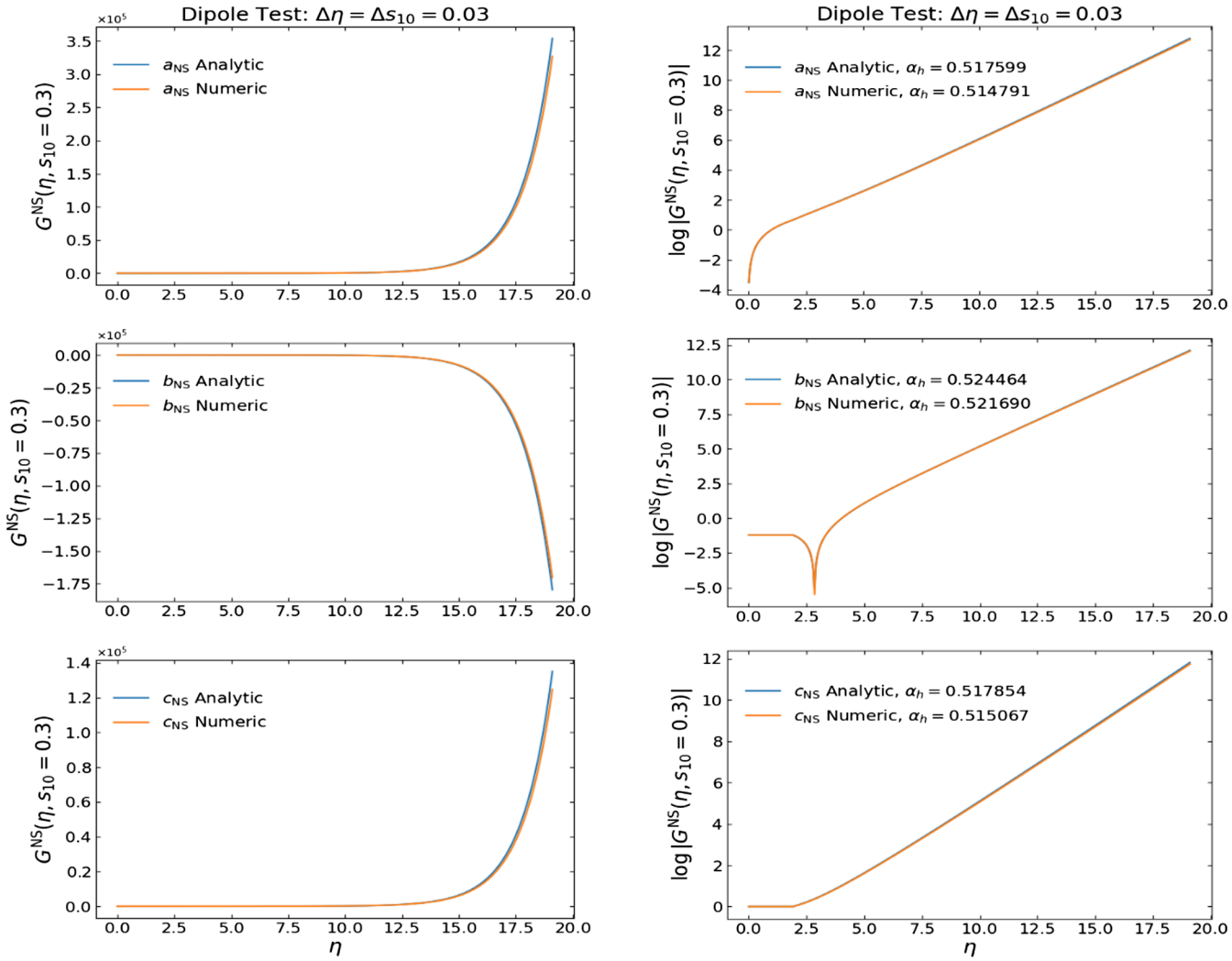

FIG. 19. $G^{\rm NS}(s_{10}, \eta)$ (left) and $\log|G^{\rm NS}(s_{10}, \eta)|$ (right) plotted as functions of η for a fixed value of $s_{10} = 0.3$. The large-η behavior corresponds to the small-x behavior, and this allows us to see how and when our numerical solution deviates from the analytic. The absolute value of the logarithm allows us to investigate the sign change (the cusp), and the slope of the logarithmic plot will give us a dipole amplitude-level intercept.

analytic solutions with a reasonably small step size of $\Delta\eta = \Delta s_{10} = \Delta = 0.03$. One can see that the analytic solution grows in magnitude slightly faster than the numeric solution. The logarithm of the absolute value of the dipole amplitudes, plotted in the right panels of Fig. 19, reveals further quantitative agreement, where we see that the numerical intercept α_h converges to within 1.4% of the analytic solution. The logarithmic scale also allows us to compare the two solutions' large-x (low-η) behaviors using the location of the sign change (the cusp) in the b_{NS} contribution (the middle-right panel of Fig. 19). The lower the fixed s_{10} value, the lower the sign change. We see in Fig. 19 that when $s_{10} = \text{const} = 0.3$, the sign changes coincide just above $\eta = 2.5$, implying that our numerical solution is equally valid as $x \to x_0$. Furthermore, we can delay the sign change by increasing s_{10} for these plots, and that will allow us to to determine the necessary resolution for retaining agreement as x becomes small. This test is given by the left-hand panel of Fig. 20, which informs us that a resolution of $\Delta\eta = \Delta s_{10} = \Delta < 0.06$ will retain analytic agreement at the dipole amplitude level. We routinely use $\Delta \lesssim 0.025$ for our numerics and global analysis.

The polarized dipole amplitude-level agreement gives us confidence to compare how each solution impacts our observables Δq^-. We employ the plots on the right-hand panel of Fig. 20 to extract the intercept of the $\ln|\Delta u^-|$ basis functions and confirm that the hPDFs asymptotics given by the analytic and numerical dipole amplitudes match within 1% and are consistent with the intercept that was computed at the dipole amplitude level. This completes the cross-check of our numerical solution for the flavor nonsinglet evolution equations.

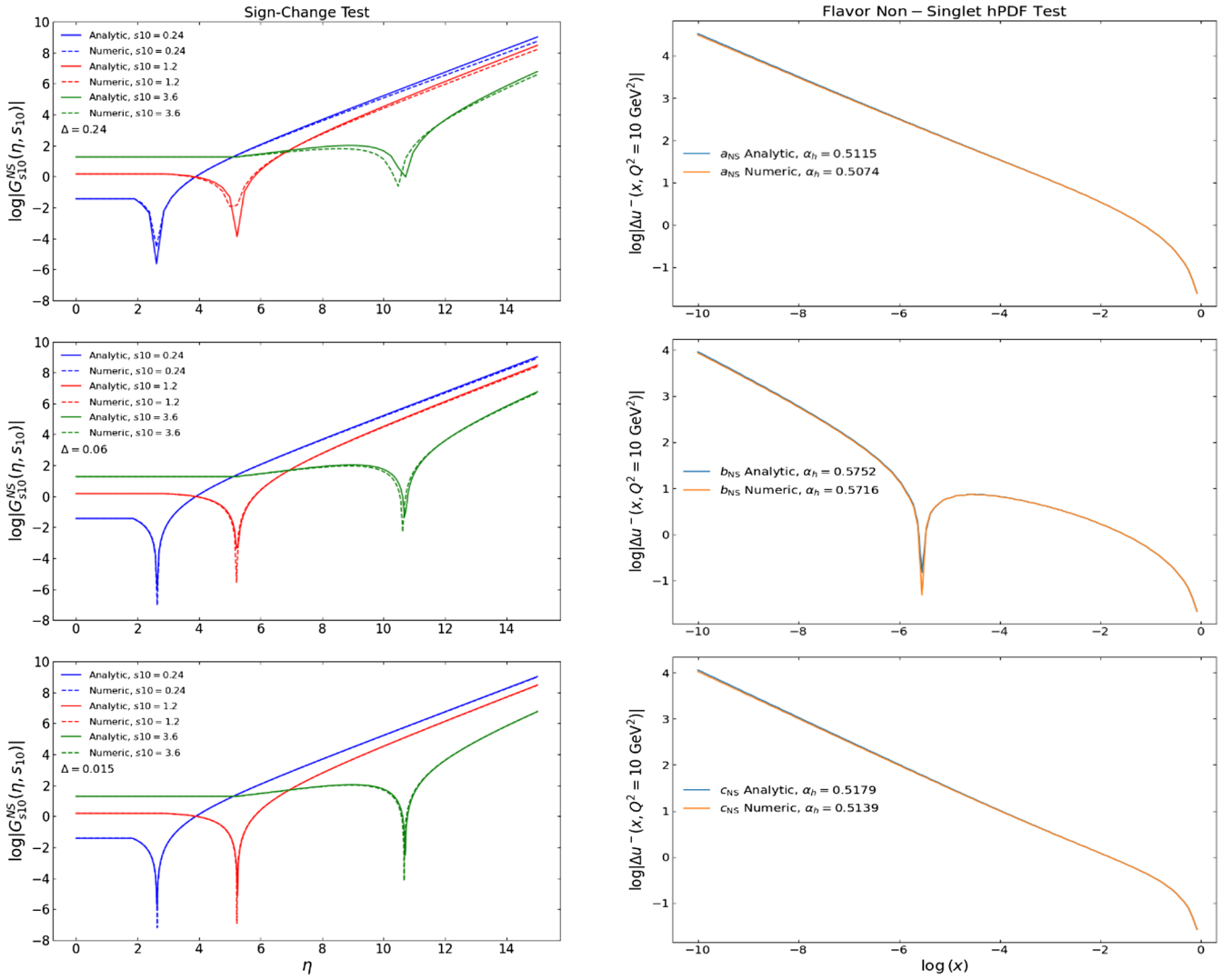

FIG. 20. Left: a plot of (the logarithm of) the s_{10} contribution to G_u^{NS} (parametrized by b_u^{NS}) as a function of η. Each color represents a different fixed value of s_{10}. The location of the sign change in the amplitude, indicated by the cusp, appears to vary with s_{10}. Smaller step sizes lead to convergence of the sign change between the analytic and numeric solutions, and $\Delta\eta = \Delta s_{10} = \Delta < 0.06$ retains small-x agreement. Right: a plot of (the logarithm of) each Δu^- basis function (parametrized by a_u^{NS}, b_u^{NS}, and c_u^{NS}) as a function of $\log(x)$. Each plot depicts the asymptotic agreement between the numeric and analytic solutions, as well as a measure of the intercept α_h.

APPENDIX C: CONVERGENCE TESTING OF NUMERICAL SOLUTIONS

The discretization defined in Appendix A is very useful for solving complicated integral equations which are very difficult if not impossible to solve analytically. The numerical solution is rather straightforward to derive, but it has the same faults as any discrete function—namely, the fact that the accuracy of a numerical solution is dependent on the resolution—i.e., the step size. In our case, we have two different variables to work with (η, s_{10}), which results in a two-dimensional grid ($G[i, j]$) for our numerical solution to compute. To simplify the discretization, we defined the step sizes for η and s_{10} to be the same, $\Delta\eta = \Delta s_{10} \equiv \Delta$. The requirement we impose on our numerical solution to confirm its validity is that as the step size decreases, the computed values should converge to a single output.

We have tested each of our flavor singlet basis functions (Fig. 1) as well as the flavor nonsinglet basis functions (not shown). However, the results can be summarized by their subsequent implementation in calculating the hPDFs $\Delta q^+(x)$ and $\Delta q^-(x)$. The left-hand panel of Fig. 21 shows $x\Delta u^+(x)$ for a "test state" of initial conditions. We define a test state simply as any replica that has been confirmed to fit data with $\chi^2/N_{\mathrm{pts}} \approx 1$. This hPDF was plotted multiple times for varying step sizes, and it is clear that as the step size decreases, the solutions converge to a single output.

The same convergence test was conducted on $x\Delta q^-(x)$ and is displayed in the right panel of Fig. 21. In this

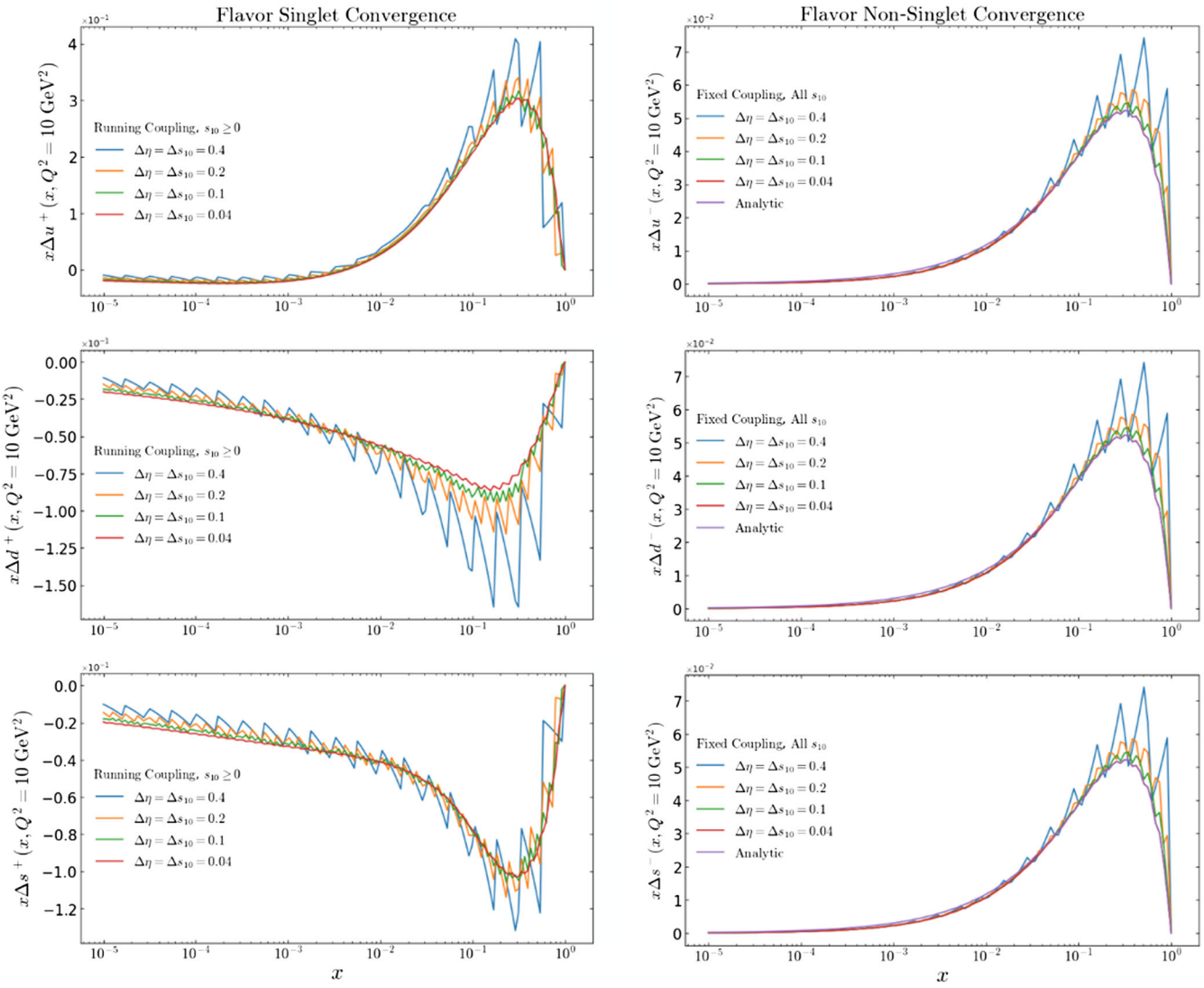

FIG. 21. Left: a numerical computation of $x\Delta q^+(x)$ for a test state of initial conditions. The graph shows the same numerical solution for various choices of step size, $\Delta = \Delta\eta = \Delta s_{10}$. As the step size Δ decreases, our numerical solution converges to a single result. Right: a numerical computation of $x\Delta q^-(x)$ that shows the convergence to a single output as Δ decreases. For both $x\Delta q^+(x)$ and $x\Delta q^-(x)$, the single output is described by the analytic solution (B16).

case, there is also an analytic solution, as discussed in Appendix B. We find not only a convergence of the numerical solution to a single output as Δ becomes smaller, but also that the converged output is exactly that of the analytic solution. We note here that Fig. 21 is a demonstration of the convergence. The results discussed in Sec. III were computed using much higher resolutions, $\Delta \approx 0.02$.

[1] C. A. Aidala, S. D. Bass, D. Hasch, and G. K. Mallot, The spin structure of the nucleon, Rev. Mod. Phys. **85**, 655 (2013).
[2] A. Accardi *et al.*, Electron ion collider: The next QCD frontier: Understanding the glue that binds us all, Eur. Phys. J. A **52**, 268 (2016).
[3] E. Leader and C. Lorcé, The angular momentum controversy: What's it all about and does it matter?, Phys. Rep. **541**, 163 (2014).
[4] E. C. Aschenauer *et al.*, The RHIC spin program: Achievements and future opportunities, arXiv:1304.0079.

[5] E.-C. Aschenauer *et al.*, The RHIC SPIN program: Achievements and future opportunities, arXiv:1501.01220.

[6] D. Boer *et al.*, Gluons and the quark sea at high energies: Distributions, polarization, tomography, arXiv:1108.1713.

[7] *Proceedings, Probing Nucleons and Nuclei in High Energy Collisions: Dedicated to the Physics of the Electron Ion Collider: Seattle (WA), United States, 2018*, edited by A. Prokudin, Y. Hatta, Y. Kovchegov, and C. Marquet (World Scientific Press, Singapore, 2020).

[8] X. Ji, F. Yuan, and Y. Zhao, What we know and what we don't know about the proton spin after 30 years, Nat. Rev. Phys. **3**, 27 (2021).

[9] R. Abdul Khalek *et al.*, Science requirements and detector concepts for the electron-ion collider: EIC Yellow Report, Nucl. Phys. **A1026**, 122447 (2022).

[10] R. L. Jaffe and A. Manohar, The G(1) problem: Fact and fantasy on the spin of the proton, Nucl. Phys. **B337**, 509 (1990).

[11] X. Ji, Gauge-invariant decomposition of nucleon spin, Phys. Rev. Lett. **78**, 610 (1997).

[12] S. Bashinsky and R. L. Jaffe, Quark and gluon orbital angular momentum and spin in hard processes, Nucl. Phys. **B536**, 303 (1998).

[13] P. Hagler and A. Schafer, Evolution equations for higher moments of angular momentum distributions, Phys. Lett. B **430**, 179 (1998).

[14] A. Harindranath and R. Kundu, On orbital angular momentum in deep inelastic scattering, Phys. Rev. D **59**, 116013 (1999).

[15] Y. Hatta and S. Yoshida, Twist analysis of the nucleon spin in QCD, J. High Energy Phys. 10 (2012) 080.

[16] X. Ji, X. Xiong, and F. Yuan, Probing parton orbital angular momentum in longitudinally polarized nucleon, Phys. Rev. D **88**, 014041 (2013).

[17] V. N. Gribov and L. N. Lipatov, Deep inelastic e p scattering in perturbation theory, Yad. Fiz. **15**, 781 (1972) [Sov. J. Nucl. Phys. **15**, 438 (1972)].

[18] G. Altarelli and G. Parisi, Asymptotic freedom in parton language, Nucl. Phys. **B126**, 298 (1977).

[19] Y. L. Dokshitzer, Calculation of the structure functions for deep inelastic scattering and e^+e^- annihilation by perturbation theory in quantum chromodynamics, Zh. Eksp. Teor. Fiz. **73**, 1216 (1977) [Sov. Phys. JETP **46**, 641 (1977)].

[20] M. Gluck, E. Reya, M. Stratmann, and W. Vogelsang, Models for the polarized parton distributions of the nucleon, Phys. Rev. D **63**, 094005 (2001).

[21] E. Leader, A. V. Sidorov, and D. B. Stamenov, Longitudinal polarized parton densities updated, Phys. Rev. D **73**, 034023 (2006).

[22] D. de Florian, R. Sassot, M. Stratmann, and W. Vogelsang, Extraction of spin-dependent parton densities and their uncertainties, Phys. Rev. D **80**, 034030 (2009).

[23] E. Leader, A. V. Sidorov, and D. B. Stamenov, Determination of polarized PDFs from a QCD analysis of inclusive and semi-inclusive deep inelastic scattering data, Phys. Rev. D **82**, 114018 (2010).

[24] P. Jimenez-Delgado, A. Accardi, and W. Melnitchouk, Impact of hadronic and nuclear corrections on global analysis of spin-dependent parton distributions, Phys. Rev. D **89**, 034025 (2014).

[25] R. D. Ball, S. Forte, A. Guffanti, E. R. Nocera, G. Ridolfi, and J. Rojo (NNPDF Collaboration), Unbiased determination of polarized parton distributions and their uncertainties, Nucl. Phys. **B874**, 36 (2013).

[26] E. R. Nocera, R. D. Ball, S. Forte, G. Ridolfi, and J. Rojo (NNPDF Collaboration), A first unbiased global determination of polarized PDFs and their uncertainties, Nucl. Phys. **B887**, 276 (2014).

[27] D. de Florian, R. Sassot, M. Stratmann, and W. Vogelsang, Evidence for polarization of gluons in the proton, Phys. Rev. Lett. **113**, 012001 (2014).

[28] E. Leader, A. V. Sidorov, and D. B. Stamenov, New analysis concerning the strange quark polarization puzzle, Phys. Rev. D **91**, 054017 (2015).

[29] N. Sato, W. Melnitchouk, S. Kuhn, J. Ethier, and A. Accardi (JAM Collaboration), Iterative Monte Carlo analysis of spin-dependent parton distributions, Phys. Rev. D **93**, 074005 (2016).

[30] J. J. Ethier, N. Sato, and W. Melnitchouk, First simultaneous extraction of spin-dependent parton distributions and fragmentation functions from a global QCD analysis, Phys. Rev. Lett. **119**, 132001 (2017).

[31] D. De Florian, G. A. Lucero, R. Sassot, M. Stratmann, and W. Vogelsang, Monte Carlo sampling variant of the DSSV14 set of helicity parton densities, Phys. Rev. D **100**, 114027 (2019).

[32] I. Borsa, G. Lucero, R. Sassot, E. C. Aschenauer, and A. S. Nunes, Revisiting helicity parton distributions at a future electron-ion collider, Phys. Rev. D **102**, 094018 (2020).

[33] Y. Zhou, N. Sato, and W. Melnitchouk (JAM Collaboration), How well do we know the gluon polarization in the proton?, Phys. Rev. D **105**, 074022 (2022).

[34] C. Cocuzza, W. Melnitchouk, A. Metz, and N. Sato (JAM Collaboration), Polarized antimatter in the proton from a global QCD analysis, Phys. Rev. D **106**, L031502 (2022).

[35] J. Bartels, B. I. Ermolaev, and M. G. Ryskin, Nonsinglet contributions to the structure function g_1 at small x, Z. Phys. C **70**, 273 (1996).

[36] J. Bartels, B. Ermolaev, and M. Ryskin, Flavor singlet contribution to the structure function G(1) at small x, Z. Phys. C **72**, 627 (1996).

[37] V. G. Gorshkov, V. N. Gribov, L. N. Lipatov, and G. V. Frolov, Doubly logarithmic asymptotic behavior in quantum electrodynamics, Yad. Fiz. **6**, 129 (1967) [Sov. J. Nucl. Phys. **6**, 95 (1968)].

[38] R. Kirschner and L. Lipatov, Double logarithmic asymptotics and Regge singularities of quark amplitudes with flavor exchange, Nucl. Phys. **B213**, 122 (1983).

[39] R. Kirschner, Reggeon interactions in perturbative QCD, Z. Phys. C **65**, 505 (1995).

[40] R. Kirschner, Regge asymptotics of scattering with flavor exchange in QCD, Z. Phys. C **67**, 459 (1995).

[41] S. Griffiths and D. A. Ross, Studying the perturbative Reggeon, Eur. Phys. J. C **12**, 277 (2000).

[42] L. V. Gribov, E. M. Levin, and M. G. Ryskin, Semihard processes in QCD, Phys. Rep. **100**, 1 (1983).

[43] E. Iancu and R. Venugopalan, The color glass condensate and high-energy scattering in QCD, in *Quark-Gluon Plasma 4*, edited by R. C. Hwa and X.-N. Wang (World Scientific, Singapore, 2003).

[44] H. Weigert, Evolution at small x_{bj}: The color glass condensate, Prog. Part. Nucl. Phys. **55**, 461 (2005).

[45] J. Jalilian-Marian and Y. V. Kovchegov, Saturation physics and deuteron-gold collisions at RHIC, Prog. Part. Nucl. Phys. **56**, 104 (2006).

[46] F. Gelis, E. Iancu, J. Jalilian-Marian, and R. Venugopalan, The color glass condensate, Annu. Rev. Nucl. Part. Sci. **60**, 463 (2010).

[47] J. L. Albacete and C. Marquet, Gluon saturation and initial conditions for relativistic heavy ion collisions, Prog. Part. Nucl. Phys. **76**, 1 (2014).

[48] Y. V. Kovchegov and E. Levin, *Quantum Chromodynamics at High Energy* (Cambridge University Press, Cambridge, England, 2012), Vol. 33.

[49] A. Morreale and F. Salazar, Mining for gluon saturation at colliders, Universe **7**, 312 (2021).

[50] K. Itakura, Y. V. Kovchegov, L. McLerran, and D. Teaney, Baryon stopping and valence quark distribution at small x, Nucl. Phys. **A730**, 160 (2004).

[51] J. Blumlein and A. Vogt, On the behavior of nonsinglet structure functions at small x, Phys. Lett. B **370**, 149 (1996).

[52] J. Blümlein and A. Vogt, The singlet contribution to the structure function $g_1(x, Q^2)$ at small x, Phys. Lett. B **386**, 350 (1996).

[53] B. I. Ermolaev, M. Greco, and S. I. Troian, QCD running coupling effects for the nonsinglet structure function at small x, Nucl. Phys. **B571**, 137 (2000).

[54] B. I. Ermolaev, M. Greco, and S. I. Troyan, Intercepts of the nonsinglet structure functions, Nucl. Phys. **B594**, 71 (2001).

[55] B. I. Ermolaev, M. Greco, and S. I. Troyan, Running coupling effects for the singlet structure function g_1 at small x, Phys. Lett. B **579**, 321 (2004).

[56] B. I. Ermolaev, M. Greco, and S. I. Troyan, Overview of the spin structure function g_1 at arbitrary x and Q^2, Riv. Nuovo Cimento **33**, 57 (2010).

[57] R. Boussarie, Y. Hatta, and F. Yuan, Proton spin structure at small-x, Phys. Lett. B **797**, 134817 (2019).

[58] Y. V. Kovchegov, D. Pitonyak, and M. D. Sievert, Helicity evolution at small-x, J. High Energy Phys. 01 (2016) 072; 10 (2016) 148(E).

[59] Y. Hatta, Y. Nakagawa, F. Yuan, Y. Zhao, and B. Xiao, Gluon orbital angular momentum at small-x, Phys. Rev. D **95**, 114032 (2017).

[60] Y. V. Kovchegov, D. Pitonyak, and M. D. Sievert, Helicity evolution at small x: Flavor singlet and non-singlet observables, Phys. Rev. D **95**, 014033 (2017).

[61] Y. V. Kovchegov, D. Pitonyak, and M. D. Sievert, Small-x asymptotics of the quark helicity distribution, Phys. Rev. Lett. **118**, 052001 (2017).

[62] Y. V. Kovchegov, D. Pitonyak, and M. D. Sievert, Small-x asymptotics of the quark helicity distribution: Analytic results, Phys. Lett. B **772**, 136 (2017).

[63] Y. V. Kovchegov, D. Pitonyak, and M. D. Sievert, Small-x asymptotics of the gluon helicity distribution, J. High Energy Phys. 10 (2017) 198.

[64] Y. V. Kovchegov and M. D. Sievert, Small-x helicity evolution: An operator treatment, Phys. Rev. D **99**, 054032 (2019).

[65] Y. V. Kovchegov, Orbital angular momentum at small x, J. High Energy Phys. 03 (2019) 174.

[66] F. Cougoulic and Y. V. Kovchegov, Helicity-dependent generalization of the JIMWLK evolution, Phys. Rev. D **100**, 114020 (2019).

[67] Y. V. Kovchegov and Y. Tawabutr, Helicity at small x: Oscillations generated by bringing back the quarks, J. High Energy Phys. 08 (2020) 014.

[68] F. Cougoulic and Y. V. Kovchegov, Helicity-dependent extension of the McLerran-Venugopalan model, Nucl. Phys. **A1004**, 122051 (2020).

[69] G. A. Chirilli, High-energy operator product expansion at sub-eikonal level, J. High Energy Phys. 06 (2021) 096.

[70] Y. V. Kovchegov, A. Tarasov, and Y. Tawabutr, Helicity evolution at small x: The single-logarithmic contribution, J. High Energy Phys. 03 (2022) 184.

[71] F. Cougoulic, Y. V. Kovchegov, A. Tarasov, and Y. Tawabutr, Quark and gluon helicity evolution at small x: Revised and updated, J. High Energy Phys. 07 (2022) 095.

[72] A. H. Mueller, Soft gluons in the infinite momentum wave function and the BFKL Pomeron, Nucl. Phys. **B415**, 373 (1994).

[73] A. H. Mueller and B. Patel, Single and double BFKL Pomeron exchange and a dipole picture of high-energy hard processes, Nucl. Phys. **B425**, 471 (1994).

[74] A. H. Mueller, Unitarity and the BFKL Pomeron, Nucl. Phys. **B437**, 107 (1995).

[75] I. Balitsky, Operator expansion for high-energy scattering, Nucl. Phys. **B463**, 99 (1996).

[76] I. Balitsky, Factorization and high-energy effective action, Phys. Rev. D **60**, 014020 (1999).

[77] Y. V. Kovchegov, Small x F(2) structure function of a nucleus including multiple Pomeron exchanges, Phys. Rev. D **60**, 034008 (1999).

[78] Y. V. Kovchegov, Unitarization of the BFKL Pomeron on a nucleus, Phys. Rev. D **61**, 074018 (2000).

[79] J. Jalilian-Marian, A. Kovner, and H. Weigert, The Wilson renormalization group for low x physics: Gluon evolution at finite parton density, Phys. Rev. D **59**, 014015 (1998).

[80] J. Jalilian-Marian, A. Kovner, A. Leonidov, and H. Weigert, The Wilson renormalization group for low x physics: Towards the high density regime, Phys. Rev. D **59**, 014014 (1998).

[81] H. Weigert, Unitarity at small Bjorken x, Nucl. Phys. **A703**, 823 (2002).

[82] E. Iancu, A. Leonidov, and L. D. McLerran, The renormalization group equation for the color glass condensate, Phys. Lett. B **510**, 133 (2001).

[83] E. Iancu, A. Leonidov, and L. D. McLerran, Nonlinear gluon evolution in the color glass condensate: 1, Nucl. Phys. **A692**, 583 (2001).

[84] E. Ferreiro, E. Iancu, A. Leonidov, and L. McLerran, Nonlinear gluon evolution in the color glass condensate: 2, Nucl. Phys. **A703**, 489 (2002).

[85] T. Altinoluk, N. Armesto, G. Beuf, M. Martinez, and C. A. Salgado, Next-to-eikonal corrections in the CGC: Gluon production and spin asymmetries in pA collisions, J. High Energy Phys. 07 (2014) 068.

[86] I. Balitsky and A. Tarasov, Rapidity evolution of gluon TMD from low to moderate x, J. High Energy Phys. 10 (2015) 017.

[87] I. Balitsky and A. Tarasov, Gluon TMD in particle production from low to moderate x, J. High Energy Phys. 06 (2016) 164.

[88] G. A. Chirilli, Sub-eikonal corrections to scattering amplitudes at high energy, J. High Energy Phys. 01 (2018) 118.

[89] J. Jalilian-Marian, Quark jets scattering from a gluon field: From saturation to high p_t, Phys. Rev. D **99**, 014043 (2019).

[90] J. Jalilian-Marian, Rapidity loss, spin, and angular asymmetries in the scattering of a quark from the color field of a proton or nucleus, Phys. Rev. D **102**, 014008 (2020).

[91] T. Altinoluk, G. Beuf, A. Czajka, and A. Tymowska, Quarks at next-to-eikonal accuracy in the CGC: Forward quark-nucleus scattering, Phys. Rev. D **104**, 014019 (2021).

[92] Y. V. Kovchegov and M. G. Santiago, Quark Sivers function at small x: Spin-dependent odderon and the sub-eikonal evolution, J. High Energy Phys. 11 (2021) 200.

[93] T. Altinoluk and G. Beuf, Quark and scalar propagators at next-to-eikonal accuracy in the CGC through a dynamical background gluon field, Phys. Rev. D **105**, 074026 (2022).

[94] Y. V. Kovchegov and M. G. Santiago, T-odd leading-twist quark TMDs at small x, J. High Energy Phys. 11 (2022) 098.

[95] T. Altinoluk, G. Beuf, A. Czajka, and A. Tymowska, DIS dijet production at next-to-eikonal accuracy in the CGC, Phys. Rev. D **107**, 074016 (2023).

[96] T. Altinoluk, N. Armesto, and G. Beuf, Probing quark transverse momentum distributions in the color glass condensate: Quark-gluon dijets in deep inelastic scattering at next-to-eikonal accuracy, arXiv:2303.12691.

[97] T. Altinoluk, G. Beuf, and J. Jalilian-Marian, Renormalization of the gluon distribution function in the background field formalism, arXiv:2305.11079.

[98] M. Li, Small x physics beyond eikonal approximation: An effective Hamiltonian approach, J. High Energy Phys. 07 (2023) 158.

[99] G. 't Hooft, A planar diagram theory for strong interactions, Nucl. Phys. **B72**, 461 (1974).

[100] G. Veneziano, Some aspects of a unified approach to gauge, dual and Gribov theories, Nucl. Phys. **B117**, 519 (1976).

[101] J. Borden and Y. V. Kovchegov, Analytic solution for the revised helicity evolution at small x and large N_c: New resummed gluon-gluon polarized anomalous dimension and intercept, Phys. Rev. D **108**, 014001 (2023).

[102] D. Adamiak, Y. V. Kovchegov, and Y. Tawabutr, Helicity evolution at small x: Revised asymptotic results at large N_c & N_f, Phys. Rev. D **108**, 054005 (2023).

[103] D. Adamiak, Y. V. Kovchegov, W. Melnitchouk, D. Pitonyak, N. Sato, and M. D. Sievert (JAM Collaboration), First analysis of world polarized DIS data with small-x helicity evolution, Phys. Rev. D **104**, L031501 (2021).

[104] B. Lampe and E. Reya, Spin physics and polarized structure functions, Phys. Rep. **332**, 1 (2000).

[105] E. B. Zijlstra and W. L. van Neerven, Order-α_s^2 corrections to the polarized structure function $g_1(x, Q^2)$, Nucl. Phys. **B417**, 61 (1994); **B426**, 245(E) (1994); **B773**, 105(E) (2007); **B501**, 599(E) (1997).

[106] R. Mertig and W. L. van Neerven, The calculation of the two loop spin splitting functions $P_{ij}^{(1)}(x)$, Z. Phys. C **70**, 637 (1996).

[107] S. Moch and J. A. M. Vermaseren, Deep inelastic structure functions at two loops, Nucl. Phys. **B573**, 853 (2000).

[108] W. L. van Neerven and A. Vogt, NNLO evolution of deep inelastic structure functions: The singlet case, Nucl. Phys. **B588**, 345 (2000).

[109] J. A. M. Vermaseren, A. Vogt, and S. Moch, The third-order QCD corrections to deep-inelastic scattering by photon exchange, Nucl. Phys. **B724**, 3 (2005).

[110] S. Moch, J. A. M. Vermaseren, and A. Vogt, The three-loop splitting functions in QCD: The helicity-dependent case, Nucl. Phys. **B889**, 351 (2014).

[111] J. Blümlein, P. Marquard, C. Schneider, and K. Schönwald, The three-loop polarized singlet anomalous dimensions from off-shell operator matrix elements, J. High Energy Phys. 01 (2022) 193.

[112] J. Blümlein and M. Saragnese, The N^{3}LO scheme-invariant QCD evolution of the non-singlet structure functions $F_2^{\mathrm{NS}}(x, Q^2)$ and $g_1^{\mathrm{NS}}(x, Q^2)$, Phys. Lett. B **820**, 136589 (2021).

[113] J. Davies, C. H. Kom, S. Moch, and A. Vogt, Resummation of small-x double logarithms in QCD: Inclusive deep-inelastic scattering, J. High Energy Phys. 08 (2022) 135.

[114] J. Blümlein, P. Marquard, C. Schneider, and K. Schönwald, The massless three-loop Wilson coefficients for the deep-inelastic structure functions F_2, F_L, xF_3 and g_1, J. High Energy Phys. 11 (2022) 156.

[115] G. Altarelli, R. K. Ellis, and G. Martinelli, Large perturbative corrections to the Drell-Yan process in QCD, Nucl. Phys. **B157**, 461 (1979).

[116] V. S. Fadin and L. N. Lipatov, BFKL Pomeron in the next-to-leading approximation, Phys. Lett. B **429**, 127 (1998).

[117] M. Ciafaloni and G. Camici, Energy scale(s) and next-to-leading BFKL equation, Phys. Lett. B **430**, 349 (1998).

[118] J. L. Albacete, N. Armesto, J. G. Milhano, and C. A. Salgado, Non-linear QCD meets data: A global analysis of lepton-proton scattering with running coupling BK evolution, Phys. Rev. D **80**, 034031 (2009).

[119] J. L. Albacete, N. Armesto, J. G. Milhano, P. Quiroga-Arias, and C. A. Salgado, AAMQS: A non-linear QCD analysis of new HERA data at small-x including heavy quarks, Eur. Phys. J. C **71**, 1705 (2011).

[120] I. Balitsky, Quark contribution to the small-x evolution of color dipole, Phys. Rev. D **75**, 014001 (2007).

[121] E. Gardi, J. Kuokkanen, K. Rummukainen, and H. Weigert, Running coupling and power corrections in nonlinear evolution at the high-energy limit, Nucl. Phys. **A784**, 282 (2007).

[122] Y. V. Kovchegov and H. Weigert, Triumvirate of running couplings in small-x evolution, Nucl. Phys. **A784**, 188 (2007).

[123] Y. V. Kovchegov and H. Weigert, Quark loop contribution to BFKL evolution: Running coupling and leading-N_f NLO intercept, Nucl. Phys. **A789**, 260 (2007).

[124] J. L. Albacete and Y. V. Kovchegov, Solving high energy evolution equation including running coupling corrections, Phys. Rev. D **75**, 125021 (2007).

[125] E. A. Kuraev, L. N. Lipatov, and V. S. Fadin, The Pomeranchuk singularity in non-Abelian gauge theories, Zh. Eksp. Teor. Fiz. **72**, 377 (1977) [Sov. Phys. JETP **45**, 199 (1977)].

[126] I. I. Balitsky and L. N. Lipatov, The Pomeranchuk singularity in quantum chromodynamics, Yad. Fiz. **28**, 1597 (1978) [Sov. J. Nucl. Phys. **28**, 822 (1978)].

[127] D. de Florian, C. A. Garcia Canal, and R. Sassot, Factorization in semiinclusive polarized deep inelastic scattering, Nucl. Phys. **B470**, 195 (1996).

[128] A. Bacchetta, M. Diehl, K. Goeke, A. Metz, P. J. Mulders, and M. Schlegel, Semi-inclusive deep inelastic scattering at small transverse momentum, J. High Energy Phys. 02 (2006) 093.

[129] A. Signori, A. Bacchetta, M. Radici, and G. Schnell, Investigations into the flavor dependence of partonic transverse momentum, J. High Energy Phys. 11 (2013) 194.

[130] A. Dumitru, A. Hayashigaki, and J. Jalilian-Marian, The color glass condensate and hadron production in the forward region, Nucl. Phys. **A765**, 464 (2006).

[131] G. A. Chirilli, B.-W. Xiao, and F. Yuan, One-loop factorization for inclusive hadron production in pA collisions in the saturation formalism, Phys. Rev. Lett. **108**, 122301 (2012).

[132] G. A. Chirilli, B.-W. Xiao, and F. Yuan, Inclusive hadron productions in pA collisions, Phys. Rev. D **86**, 054005 (2012).

[133] L. L. Frankfurt, M. I. Strikman, L. Mankiewicz, A. Schafer, E. Rondio, A. Sandacz, and V. Papavassiliou, The valence and strange sea quark spin distributions in the nucleon from semi-inclusive deep inelastic lepton scattering, Phys. Lett. B **230**, 141 (1989).

[134] D. de Florian, L. N. Epele, H. Fanchiotti, C. A. Garcia Canal, S. Joffily, and R. Sassot, Next-to-leading order semi-inclusive spin asymmetries, Phys. Lett. B **389**, 358 (1996).

[135] E. S. Ageev *et al.* (COMPASS Collaboration), Spin asymmetry A_1^d and the spin-dependent structure function g_1^d of the deuteron at low values of x and Q^2, Phys. Lett. B **647**, 330 (2007).

[136] T. Hobbs and W. Melnitchouk, Finite-Q^2 corrections to parity-violating DIS, Phys. Rev. D **77**, 114023 (2008).

[137] Y. Zhao, A. Deshpande, J. Huang, K. Kumar, and S. Riordan, Neutral-current weak interactions at an EIC, Eur. Phys. J. A **53**, 55 (2017).

[138] D. Wang, Measurement of the parity-violating asymmetry in deep inelastic scattering at JLab 6 GeV, Ph.D. thesis, Virginia U., 2013.

[139] N. Sato, C. Andres, J. J. Ethier, and W. Melnitchouk (JAM Collaboration), Strange quark suppression from a simultaneous Monte Carlo analysis of parton distributions and fragmentation functions, Phys. Rev. D **101**, 074020 (2020).

[140] E. Moffat, W. Melnitchouk, T. C. Rogers, and N. Sato (JAM Collaboration), Simultaneous Monte Carlo analysis of parton densities and fragmentation functions, Phys. Rev. D **104**, 016015 (2021).

[141] P. L. Anthony *et al.* (E142 Collaboration), Deep inelastic scattering of polarized electrons by polarized He-3 and the study of the neutron spin structure, Phys. Rev. D **54**, 6620 (1996).

[142] K. Abe *et al.* (E154 Collaboration), Precision determination of the neutron spin structure function g_1^n, Phys. Rev. Lett. **79**, 26 (1997).

[143] K. Abe *et al.* (E143 Collaboration), Measurements of the proton and deuteron spin structure functions g_1 and g_2, Phys. Rev. D **58**, 112003 (1998).

[144] P. L. Anthony *et al.* (E155 Collaboration), Measurement of the deuteron spin structure function $g_1^d(x)$ for $1\ (\mathrm{GeV}/c)^2 < Q^2 < 40\ (\mathrm{GeV}/c)^2$, Phys. Lett. B **463**, 339 (1999).

[145] P. L. Anthony *et al.* (E155 Collaboration), Measurements of the Q^2 dependence of the proton and neutron spin structure functions g_1^p and g_1^n, Phys. Lett. B **493**, 19 (2000).

[146] J. Ashman *et al.* (European Muon Collaboration), An investigation of the spin structure of the proton in deep inelastic scattering of polarized muons on polarized protons, Nucl. Phys. **B328**, 1 (1989).

[147] B. Adeva *et al.* (Spin Muon Collaboration), Spin asymmetries A(1) and structure functions g_1 of the proton and the deuteron from polarized high-energy muon scattering, Phys. Rev. D **58**, 112001 (1998).

[148] B. Adeva *et al.* (Spin Muon Collaboration), Spin asymmetries A(1) and structure functions g_1 of the proton and the deuteron from polarized high-energy muon scattering, Phys. Rev. D **58**, 112001 (1998).

[149] B. Adeva *et al.* (Spin Muon Collaboration), Spin asymmetries A(1) of the proton and the deuteron in the low x and low Q^2 region from polarized high-energy muon scattering, Phys. Rev. D **60**, 072004 (1999); **62**, 079902 (E) (2000).

[150] M. G. Alekseev *et al.* (COMPASS Collaboration), The spin-dependent structure function of the proton g_1^p and a test of the Bjorken sum rule, Phys. Lett. B **690**, 466 (2010).

[151] C. Adolph *et al.* (COMPASS Collaboration), The spin structure function g_1^{p} of the proton and a test of the Bjorken sum rule, Phys. Lett. B **753**, 18 (2016).

[152] C. Adolph *et al.* (COMPASS Collaboration), Final COMPASS results on the deuteron spin-dependent structure function g_1^{d} and the Bjorken sum rule, Phys. Lett. B **769**, 34 (2017).

[153] K. Ackerstaff *et al.* (HERMES Collaboration), Measurement of the neutron spin structure function g_1^n with a polarized He-3 internal target, Phys. Lett. B **404**, 383 (1997).

[154] A. Airapetian *et al.* (HERMES Collaboration), Precise determination of the spin structure function g_1 of the proton, deuteron and neutron, Phys. Rev. D **75**, 012007 (2007).

[155] B. Adeva *et al.* (Spin Muon Collaboration), Polarized quark distributions in the nucleon from semi-inclusive spin asymmetries, Phys. Lett. B **420**, 180 (1998).

[156] M. G. Alekseev *et al.* (COMPASS Collaboration), Quark helicity distributions from longitudinal spin asymmetries in muon-proton and muon-deuteron scattering, Phys. Lett. B **693**, 227 (2010).

[157] M. Alekseev *et al.* (COMPASS Collaboration), Flavour separation of helicity distributions from deep inelastic muon-deuteron scattering, Phys. Lett. B **680**, 217 (2009).
[158] A. Airapetian *et al.* (HERMES Collaboration), Quark helicity distributions in the nucleon for up, down, and strange quarks from semi-inclusive deep-inelastic scattering, Phys. Rev. D **71**, 012003 (2005).
[159] K. Ackerstaff *et al.* (HERMES Collaboration), Flavor decomposition of the polarized quark distributions in the nucleon from inclusive and semi-inclusive deep inelastic scattering, Phys. Lett. B **464**, 123 (1999).
[160] N. Kovensky, G. Michalski, and M. Schvellinger, Deep inelastic scattering from polarized spin-1/2 hadrons at low x from string theory, J. High Energy Phys. 10 (2018) 084.
[161] D. Jorrin and M. Schvellinger, Scope and limitations of a string theory dual description of the proton structure, Phys. Rev. D **106**, 066024 (2022).
[162] I. Borsa, D. Jorrin, R. Sassot, and M. Schvellinger, Proton helicity structure function g_1^p from a holographic Pomeron, Phys. Rev. D **108**, 056024 (2023).
[163] Y. Hatta, T. Ueda, and B.-W. Xiao, Polarized DIS in $N = 4$ SYM: Where is spin at strong coupling?, J. High Energy Phys. 08 (2009) 007.
[164] C. Van Hulse *et al.*, Evaluation of longitudinal double-spin asymmetry measurements in semi-inclusive deep-inelastic scattering from the proton for the ECCE detector design, Nucl. Instrum. Methods Phys. Res., Sect. A **1056**, 168563 (2023).
[165] Y. Zhou, C. Cocuzza, F. Delcarro, W. Melnitchouk, A. Metz, and N. Sato (JAM Collaboration), Revisiting quark and gluon polarization in the proton at the EIC, Phys. Rev. D **104**, 034028 (2021).
[166] A. Candido, S. Forte, and F. Hekhorn, Can $\overline{\text{MS}}$ parton distributions be negative?, J. High Energy Phys. 11 (2020) 129.
[167] J. Collins, T. C. Rogers, and N. Sato, Positivity and renormalization of parton densities, Phys. Rev. D **105**, 076010 (2022).
[168] A. Candido, S. Forte, T. Giani, and F. Hekhorn, On the positivity of $\overline{\text{MS}}$ parton distributions, arXiv:2308.00025.
[169] H. Müller and R. Dingle, Asymptotic expansions of Mathieu functions and their characteristic numbers, J. Reine Angew. Math. (Crelles Journal), 11 (1962).
[170] R. E. O'Malley and R. E. O'Malley, The method of matched asymptotic expansions and its generalizations, in *Historical Developments in Singular Perturbations* (Springer Cham, 2014).
[171] A. Dumitru and R. Paatelainen, Sub-femtometer scale color charge fluctuations in a proton made of three quarks and a gluon, Phys. Rev. D **103**, 034026 (2021).
[172] G. Altarelli and G. G. Ross, The anomalous gluon contribution to polarized leptoproduction, Phys. Lett. B **212**, 391 (1988).
[173] G. M. Shore and G. Veneziano, The U(1) Goldberger-Treiman relation and the proton "spin": A renormalization group analysis, Nucl. Phys. **B381**, 23 (1992).
[174] A. Tarasov and R. Venugopalan, Role of the chiral anomaly in polarized deeply inelastic scattering: Finding the triangle graph inside the box diagram in Bjorken and Regge asymptotics, Phys. Rev. D **102**, 114022 (2020).
[175] A. Tarasov and R. Venugopalan, Role of the chiral anomaly in polarized deeply inelastic scattering: II. Topological screening and transitions from emergent axionlike dynamics, Phys. Rev. D **105**, 014020 (2022).
[176] S. Bhattacharya, Y. Hatta, and W. Vogelsang, Chiral and trace anomalies in deeply virtual Compton scattering, Phys. Rev. D **107**, 014026 (2023).
[177] S. Bhattacharya, Y. Hatta, and W. Vogelsang, Chiral and trace anomalies in deeply virtual Compton scattering: II. QCD factorization and beyond, Phys. Rev. D **108**, 014029 (2023).